PHYSICS REPORTS (Review Section of Physics Letters) 70, No. 5 (1981) 315–398. North-Holland Publishing Company

OPTICAL PROPERTIES OF HIGHLY EXCITED DIRECT GAP SEMICONDUCTORS*

C. KLINGSHIRN

Institut für Angewandte Physik der Universität Karlsruhe, Kaiserstr. 12, D-7500 Karlsruhe, Fed. Rep. Germany

and

H. HAUG

Institut für Theoretische Physik der Universität Frankfurt, Robert-Mayer-Str. 8, D-6000 Frankfurt-Main, Fed. Rep. Germany

Received July 1980

Contents:

Abstract:

The electronic excitations in direct gap semiconductors interact strongly with the photon field. We discuss both the experimental and the theoretical aspects of the optical properties of these materials under strong optical excitation. We distinguish between intermediate excitation levels at which the electronic excitations form a dense system of excitons and excitonic molecules and very high excitation levels at which a degenerate electron–hole plasma occurs. The optical spectra of dense excitonic systems, which are mainly observed in copper halides and II–VI compounds, are shown to be determined mainly by the interaction processes between excitonic molecules, polaritons and free carriers. The optical properties of the electron–hole plasma, which has been observed in II–VI and especially in III–V compounds, can be understood only by taking into account many-body effects, such as dynamical screening of the Coulomb interactions, plasmon-assisted transitions and excitonic enhancement.

* The experimental part of this paper is based on the Habilitation-thesis of one of the authors (C.K.).

0370–1573/81/0000–0000/$16.80

OPTICAL PROPERTIES OF HIGHLY EXCITED DIRECT GAP SEMICONDUCTORS

C. KLINGSHIRN

Institut für Angewandte Physik der Universität Karlsruhe, Kaiserstr. 12, D-7500 Karlsruhe, Fed. Rep. Germany

and

H. HAUG

Institut für Theoretische Physik der Universität Frankfurt, Robert-Mayer-Str. 8, D-6000 Frankfurt-Main, Fed. Rep. Germany

NORTH-HOLLAND PUBLISHING COMPANY - AMSTERDAM

1. Introduction

Since more than ten years, the investigation of highly excited semiconductors (HES) became an increasingly important part of solid state physics, as can be deduced e.g. from the topics of the last international semiconductor- and luminescence conferences.

Though our understanding of the physics of HES is not yet complete in several respects (and probably will never be), the fundamental ideas are now rather well established. Therefore, it is reasonable to review our present knowledge of this field from both the experimental and theoretical point of view.

In this section, we try to describe what we mean by HES and we present a short review of their history. In section 2, the electronic quasiparticles are introduced, which are most important in HES. Section 3 gives some general considerations about the experimental needs for the investigation of HES and the description of some particular setups. In sections 4 and 5 we report theoretical treatments and experimental results concerning the optical properties of direct gap HES with dense excitonic systems or electron–hole plasmas. A detailed comparison between experiment and theory is given.

1.1. *What are "highly excited semiconductors"?*

We try to deduce a "definition" of HES from an example. Fig. 1 shows spectra of the near edge luminescence of CdS [1.1] at low temperature and for different excitation intensities I_{exc}.* Spectrum a has been taken under steady state band-to-band excitation by a conventional, high pressure mercury lamp, I_{exc} being 2 mW cm^{-2}. The two narrow peaks observed at 2.537 eV (I_1) and 2.546 eV (I_2) are due

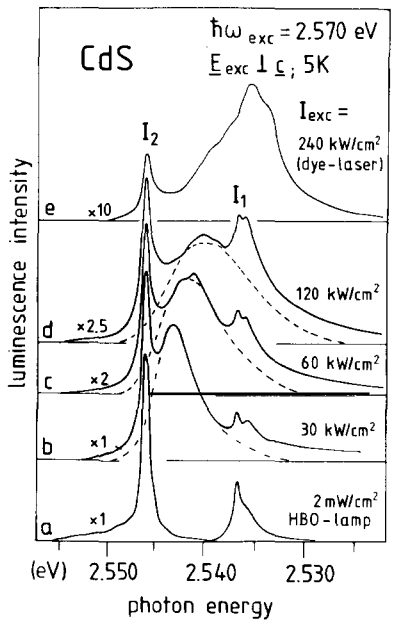

Fig. 1. Near-edge luminescence spectra of CdS at low temperature for different excitation intensities I_{exc}. The normalization factors are given on the left. The dashed lines indicate the so-called M-band (from Schrey and Klingshirn [1.1]).

* For the precise meaning of this quantity see subsection 3.1.

to the recombination of excitons (i.e. bound electron–hole pair states) which are bound to neutral acceptors and donors, respectively [1.2]. The emission around 2.553 eV is due to the weak contribution of the free exciton. It is possible to increase or to decrease I_{exc} by several orders of magnitude, without significant changes of the shape of the emission bands. For $I_{exc} \gtrsim 10^4\,W\,cm^{-2}$, however, a characteristic change is observed: On the low-energy side of I_2, a new emission-band appears. With increasing I_{exc}, the emission broadens and shifts to longer wavelengths. Its luminescence intensity I_{lum}* grows superlinearly with I_{exc} (fig. 1b–d). This emission-band is generally called M-band and will be discussed in more detail in subsection 4.5. At the highest excitation, which is shown in fig. 1e, the luminescence hardly resembles the low-excitation spectrum. Instead of rather sharp lines, a broad and weakly structured band dominates the luminescence.

Depending on the peculiarities of the experiment and of the sample, other new emission-bands may show up together with or instead of the M-band with increasing I_{exc}. The features, which are demonstrated in fig. 1 for CdS, are general in that sense, that in all semiconductors under investigation so far, new emission-bands appear when I_{exc} is increased to sufficiently high values. Since this luminescence occurs in the near-edge region, i.e., at energies which correspond to recombination processes of free excitons or of excitons weakly bound to impurities or of free electron–hole pairs, the presumption suggests itself, that these new emission bands are due to interaction processes of excitons or free carriers either among themselves or with other quasiparticles. This leads us to the following "definition": HES are semiconductors in which the density of electronic excitations has been increased by an external excitation source to such high values, that interaction processes between these quasiparticles, which are absent at low densities, become effective and give rise to new radiative or radiationless recombination processes. The thermal energy has to be reduced to a value, which is comparable to or smaller than typical interaction energies between the electronic excitations.

In an intermediate regime of excitation intensities I_{exc}, the excitons still appear as individual quasiparticles. The recombination processes in which bound electron-hole pairs participate, are called excitonic processes. They are treated in section 4. At still higher electronic densities, the bound pair-states are no longer stable, and a collective state of electron-hole pairs is created, a so-called electron-hole plasma. Its optical properties are discussed in section 5.

1.2. Scope of this paper

In the last decade, the investigation of HES yielded a vast number of results, both theoretical and experimental. Therefore, in a review of this subject, a restriction to a limited number of topics is necessary.

We limit ourselves here to theoretical and experimental aspects of high excitation effects in semiconductors with a direct, dipole-allowed gap, i.e. mainly copper halides, II–VI and direct III–V compounds. The reader interested in the results of indirect semiconductors is referred to a number of excellent review articles: for Ge and Si e.g. [1.3–1.7] and for the indirect III–V compounds e.g. [1.8–1.11] and the literature cited therein. Furthermore, we restrict outselves to the optical properties of HES, i.e., luminescence, absorption, optical gain and reflection. One of the most important radiationless recombination processes in dense systems of electronic excitations is the Auger-process. Detailed information about this mechanism is given e.g. in [1.12].

Concerning the literature, we try to cite contributions of all groups, that have brought some progress

* For the precise meaning of this quantity see subsection 3.1.

to the subject. Due to the overwhelming number of publications (and because of lack of space) it is impossible, to mention all contributions, and we apologize for this.

Other reviews of various aspects of HES are found e.g. in [1.13–1.25] and in the proceedings of the international luminescence and semiconductor conferences [1.26–1.28].

1.3. History of highly excited semiconductors

The history of HES started about twenty years ago. The first suggestions, that new phenomena could occur in high-density electronic systems appeared at the end of the fifties and the beginning of the sixties, at a time, when the excitons themselves where just understood in some detail [e.g. 1.29, 1.30].

In 1958 Lampert [1.31] and Moskalenko [1.32] suggested, that besides the excitons more complex electronic quasiparticles might exist, made up of three or four carriers. The latter one, consisting of two electrons and two holes is now well known as biexciton or excitonic molecule (see section 4). In 1962 Thomas and Hopfield [1.33] reflected, under which conditions the bound exciton recombination could show stimulated emission, and in fact it turned out, that stimulation effects – though generally not of bound excitons – play an important role in the investigation of HES. Some early works in this field are e.g. [1.13–1.15; 1.34–1.44]. The impetus to do research in the field of HES came at that time mainly from the investigations of p-n junction lasers, see e.g. [1.16, 1.43, 1.44].

The idea, that excitons may undergo at high densities a transition from an excitonic gas phase to a metallic electron–hole liquid (EHL), was introduced by Keldysh 1968 [1.45] and became a powerful tool for the understanding of many high-density phenomena, especially in Si and Ge. First experimental results appeared in the second half of the sixties, see e.g. [1.34–1.37]. Haynes [1.46] described e.g. in 1966 the appearance of an emission line in Si at low temperature and under increasing excitation, which was also observed by Benoit à la Guillaume [1.47].

Haynes attributed it to the decay of a biexciton. Now we know, that this new emission-band is due to the recombination in an EHL, whereas the radiative decay of biexcitons was observed first by the Strasbourg-group in 1968 [1.48]. Some early and very important experiments concerning the EHL in Ge came from scientists mainly in the USSR [e.g. 1.49–1.54].

At the end of the sixties and the beginning of the seventies, a rapid increase of the research on HES took place, to which many groups all over the world contributed. One realized soon, that all semiconductors show new emission-bands, if they are exposed to a sufficiently strong excitation. One tried to understand the origin of these new luminescence structures. The interpretations at that time were mainly based on the spectral positions of the bands, especially of their maxima, and the superlinear increase of the luminescence intensity I_{lum} with the excitation:

$$I_{\text{lum}} \sim I_{\text{exc}}^{\beta}. \tag{1.1}$$

Values of the exponent β between 1 and 2 were observed in the case of spontaneous emission and up to 7 or even more for stimulated recombination. Attempts were made, to explain these values of β in the frame of some models for the reaction kinetics. Typical examples of these models are found e.g. in [1.55 and 1.56].

Eventually one realized, however, that a superlinear increase of I_{lum} with I_{exc}, sometimes followed by a saturation [1.18; 1.57], is not characteristic for a certain recombination process, but it is a general property of almost all high-excitation phenomena. Concerning the spectral positions of the emission maxima, the imagination of the physicists was sufficiently well developed, to invent not only one but several possible mechanisms for the observed emission peaks. For the M-band in wurtzite II–VI

compounds, shown for CdS in fig. 1, there exist in the moment about six different models, which all are able to explain the appearance of an emission-band at just this position (see subsection 4.5).

These disillusions were even increased by the fact, that is was possible to get optically or electron beam pumped laser emission from the near UV to the near IR using various semiconductors, but that cheap, reliable p-n junction lasers could be fabricated only for the longer wavelength part of this spectrum. Semiconductors with a larger gap ($E_g \gtrsim 2.3$ eV) can generally be grown only as either n- or p-type material.

Having realized, that the investigation of the luminescence spectra as a function of I_{exc} and the lattice temperature T_L using band-to-band excitation with lasers* or electron beams did not yield sufficient information to identify the different recombination processes, the scientists started to use – apart from the "classical" luminescence spectroscopy – more sophisticated techniques. Presently, one- or two-photon absorption and excitation spectroscopy as well as two-photon Raman techniques are applied. In addition the reflection- and transmission spectra of the samples are investigated as function of I_{exc}, T_L and other parameters using separate probe and pump beams. Furthermore, the time resolution has been extended to the picosecond region [see e.g. 1.58].

These new techniques have become possible only by a corresponding development of the laser technology. Especially, the availability of tunable, high-power, narrow bandwidth dye-lasers and of mode-locked picosecond lasers brought a significant progress to the investigation of HES.

Parallel to the development of experimental techniques and the increasing wealth of experimental data, large efforts have been made to describe HES by appropriate theoretical models. The step from qualitative models to a quantitative understanding has already been performed in many fields of HES.

2. Electronic quasiparticles

In this section, we present those quasiparticles, which are of major importance in the investigation of HES. We start with a short outline of the single particle concept in semiconductors which is given by the band structures. In subsection 2.2 the concept of excitons and excitonic polaritons is introduced for the simplified case of a two-band model. In subsection 2.3 we shortly discuss some of the implications brought about by the real band structure. The last parts of this section contain some remarks about biexcitons and plasmons.

2.1. Free carriers and their band structure

The relation between the momentum $\boldsymbol{k}$ and the energy E of single free carriers is given by the band structure, which is the solution of the $N \pm 1$ particle problem in the following sense: An ideal semiconductor at $T = 0$ K has a valence band, which is completely filled with N electrons. All those states in which an additional electron can be put, form the conduction bands and all those states from which one electron can be removed, form the valence bands.

The properties of the band structures of direct materials discussed here, can qualitatively be understood, if we assume that the lattice periodic parts of the Bloch functions are still related to the parent atomic orbitals. This approach is justified in compounds with a rather strong ionic contribution to the binding such as the Cu-halides or the II–VI compounds. This requirement is fulfilled only to a

* At that time mainly the fundamental and harmonic waves of Q-switched ruby and neodymium-lasers have been used.

Table 1
Correlation between atomic s- and p-levels and the conduction- and valenceband-symmetries, respectively, for the pointgroup T_d

Atomic level	Quantum-number of the orbital angular momentum l	Irreducible representation	Degeneracy	Spin	Quantum-number of the total angular momentum j	Irreducible representation	Degeneracy
s	0	Γ_1	1	1/2	1/2	Γ_6	2
p	1	Γ_5	3	1/2	3/2 1/2	Γ_8 Γ_7	4 2

minor degree for the III–V compounds, which have a more homeopolar binding [2.1]. Nevertheless, this approach yields the correct symmetries of the lowest conduction and the upper valence bands in all three classes of compounds. In this picture, the conduction bands are mainly formed by the first unoccupied s-levels of generally the cations (e.g. the 4s levels of Cu and Cl in CuCl [2.2], the 4s- or 5s-levels of Zn or Cd in ZnO and CdS, CdSe, respectively, [e.g. 2.3, 2.4], or the 4s-levels of Ga in GaAs*). The valence bands are correspondingly made up from the highest occupied levels, generally p-levels of the anions (e.g. 3p-levels of Cl [2.2], 2p, 3p or 4p-levels of O, S or Se, respectively [2.3, 2.4], and the 4p-levels of As). Often, there is an admixture of lower lying d-levels to the valence bands, especially in the Cu-halides [2.2].

From this type of electron configuration, one concludes immediately, that the band-to-band transition is optically dipole-allowed. Since the band extrema are situated at $\boldsymbol{k} = 0$ in all compounds considered here, one can deduce the symmetries of the bands at the Γ-point from the compatibility relations between the irreducible representations of the full rotation group and those of the corresponding point groups. The results are given in the following tables for T_d and C_{6v} symmetry, neglecting for the moment all mixing of the states due to symmetry-breaking effects. Typical examples for the point group T_d are GaAs, GaSb, InP, ZnSe, ZnTe, CuCl, CuBr, CuJ; and for C_{6v}: CdS, CdSe, ZnO, ZnS.

In the cubic symmetry (see table 1) one has at the Γ-point a twofold degenerate conduction band and two degenerate valence bands, split by the spin-orbit coupling. In most cases the fourfold Γ_8 level is higher in energy. In CuCl, however, the Γ_7 level forms the upper valence bands, because of a negative

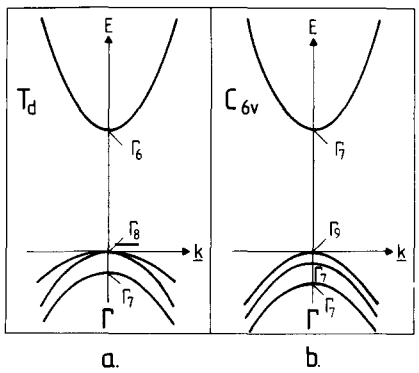

Fig. 2. A schematic drawing of the band structure at the Γ-point, (a) T_d-symmetry, (b) C_{6v}-symmetry.

* See however [2.5].

Table 2
Correlation between atomic s- and p-levels and the conduction- and valence-band symmetries, respectively, for the pointgroup C_{6v}

Atomic level	z-component of orbital angular momentum l_z	Irreducible representation	Degeneracy	z-component of the spin s_z	z-component of the total angular momentum j_z	Irreducible representation	Degeneracy
s	0	Γ_1	1	±1/2	±1/2	Γ_7	2
p	±1	Γ_5	2	±1/2	±3/2	Γ_9	2
				∓1/2	±1/2	Γ_7	2
	0	Γ_1	1	±1/2	±1/2	Γ_7	2

spin–orbit coupling caused by the admixture of the 3d-levels of Cu [2.6]. Away from the Γ-point, the fourfold Γ_8 level splits into a light and a heavy hole band, as schematically shown in fig. 2a. A detailed description of the valence bands, including k-linear and warping terms, is given e.g. in [2.7, 2.13, 2.14].

The corresponding table for the uniaxial wurtzite type compounds is given above. Since only the components of the angular momentum parallel to the crystallographic c-axis are (at least partly) good quantum numbers, we give only these (see table 2).

The sixfold anion level is split by the uniaxial crystal-field and by the spin–orbit coupling into three degenerate valence bands, sometimes labeled A, B and C from higher to lower energies with symmetries Γ_9, Γ_7 and Γ_7, respectively. Note the two different Γ_7 levels. Only in ZnO the upper two valence bands are reversed, again because of a negative spin–orbit coupling. The band curvature may be different for $\boldsymbol{k} \| \boldsymbol{c}$ and $\boldsymbol{k} \perp \boldsymbol{c}$. In fact it turns out, that the conduction band is generally rather isotropic, whereas the valence bands frequently show strong anisotropies (e.g. in CdS and CdSe [2.3], but not in ZnO [2.8]).

2.2. Excitons and excitonic polaritons

The excitons can be considered as the excited states of the N-particle system: An electron from the valence band is excited into the conduction band. The attractive Coulomb potential between the missing electron in the valence band, which can be regarded as a positively charged hole and the electron in the conduction band gives rise to a hydrogenlike spectrum (fig. 3) with an infinite number of bound states

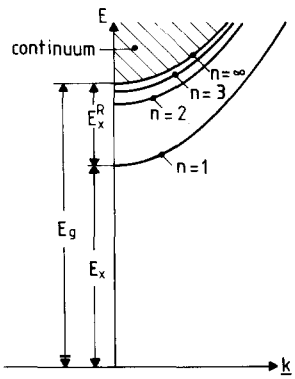

Fig. 3. A schematic sketch of the dispersion curves of Wannier excitons in direct gap materials. The bound states form the discrete bands with main quantum numbers $n = 1, 2, \ldots$, while the ionized states form a continuum (shaded region). E_g is the gap energy and E_x^R the excitonic Rydberg energy. The curvature of the dispersion curves gives the effective mass of the exciton.

and an ionization continuum. In this paper we call the bound states of electron–hole (e–h) pairs exciton states (x), while we refer to ionized e–h pairs as free carriers. However, the expression "free carriers" does not imply that the effect of the strong Coulomb forces between the electronic excitations could be neglected. Thus, an x-state can be build by an appropriate superposition of e–h pair states, which in a simple two-band model for cubic crystal symmetry is given by:

$$a^+_{\boldsymbol{k},s} b^+_{\boldsymbol{k}',s'} |0\rangle \tag{2.1}$$

where $a^+_{\boldsymbol{k},s}$ is the creation operator for an electron in the conduction band with wavevector $\boldsymbol{k}$ and spin s, while $b^+_{\boldsymbol{k}',s'}$ is the creation operator of a hole in the valence band. This operator is obtained from the annihilation operator of an electron in the valence band by

$$b^+_{\boldsymbol{k},s} = \sigma_s a_{-\boldsymbol{k},-s}, \tag{2.2}$$

where $\sigma_s = (-1)^{(1/2-s)}$ is a sign-function, which has its origin in the time-reversal transformation of a spin state [2.9, 2.10]. Both the electron and hole operators obey Fermi commutation relations. The vacuum state is the crystal ground state. In cubic structures the pair states are classified according to the total spin

$$|p^{S,S_z}_{\boldsymbol{k},\boldsymbol{k}'}\rangle. \tag{2.3}$$

The triplet states are given by $S = 1$, $S_z = 0, \pm 1$

$$|p^{1,1}_{\boldsymbol{k},\boldsymbol{k}'}\rangle = a^+_{\boldsymbol{k},+1/2} b^+_{\boldsymbol{k}',+1/2} |0\rangle \tag{2.4}$$

$$|p^{1,0}_{\boldsymbol{k},\boldsymbol{k}'}\rangle = \frac{1}{\sqrt{2}} (a^+_{\boldsymbol{k},+1/2} b^+_{\boldsymbol{k}',-1/2} + a^+_{\boldsymbol{k},-1/2} b^+_{\boldsymbol{k}',+1/2}) |0\rangle \tag{2.5}$$

$$|p^{1,-1}_{\boldsymbol{k},\boldsymbol{k}'}\rangle = a^+_{\boldsymbol{k},-1/2} b^+_{\boldsymbol{k}',-1/2} |0\rangle, \tag{2.6}$$

while the singlet state with $S = 0$, $S_z = 0$ is given by

$$|p^{0,0}_{\boldsymbol{k},\boldsymbol{k}'}\rangle = \frac{1}{\sqrt{2}} (a^+_{\boldsymbol{k},+1/2} b^+_{\boldsymbol{k}',-1/2} - a^+_{\boldsymbol{k},-1/2} b^+_{\boldsymbol{k}',+1/2}) |0\rangle. \tag{2.7}$$

The general pair state is then obtained as

$$|p\rangle = \sum_{\boldsymbol{k},\boldsymbol{k}'} C^{S,S_z}_{\boldsymbol{k},\boldsymbol{k}'} |p^{S,S_z}_{\boldsymbol{k},\boldsymbol{k}'}\rangle. \tag{2.8}$$

From the e–h-Hamiltonian (see e.g. ref. [1.22]) we can derive an equation for the pair amplitude $C^{S,S_z}_{\boldsymbol{k},\boldsymbol{k}'}$:

$$(E_e(\boldsymbol{k}) + E_h(\boldsymbol{k}') - E) C^{S,S_z}_{\boldsymbol{k},\boldsymbol{k}'} - \sum_{\bar{\boldsymbol{k}},\bar{\boldsymbol{k}}'} (V^{cvvc}_{\boldsymbol{k}-\bar{\boldsymbol{k}}',-\boldsymbol{k}'-\bar{\boldsymbol{k}}} - 2\delta_{S,0} V^{cvcv}_{\boldsymbol{k}-\bar{\boldsymbol{k}}',-\bar{\boldsymbol{k}}-\boldsymbol{k}'}) C^{S,S_z}_{\bar{\boldsymbol{k}},\bar{\boldsymbol{k}}'} = 0. \tag{2.9}$$

Here, $E_e(\boldsymbol{k})$ and $E_h(\boldsymbol{k}')$ are the energies of the noninteracting electrons and holes, respectively. The

Coulomb matrix elements are

$$V^{ijlm}_{k_1k_2k_3k_4} = \langle \boldsymbol{k}_1 i, \boldsymbol{k}_2 j | \frac{e^2}{|\boldsymbol{r} - \boldsymbol{r}'|} | \boldsymbol{k}_3 l, \boldsymbol{k}_4 m \rangle, \tag{2.10}$$

where the band indices i, j, l, m can be either c or v. Eq. (2.9) shows that the exchange interaction shifts the singlet states with respect to the triplet states. The resulting energy shift is different for the longitudinal and transversal singlet excitons. In the limit of a large exciton, the exchange interaction is small compared with the direct e–h Coulomb interaction. If we express further $E_e(\boldsymbol{k})$ and $E_h(\boldsymbol{k}')$ by the effective mass approximation, we obtain the Wannier equation

$$\left(-\frac{\hbar^2\nabla_e^2}{2m_e} - \frac{\hbar^2\nabla_h^2}{2m_h} + E_g - \frac{e^2}{\varepsilon_0|\boldsymbol{r}_e - \boldsymbol{r}_h|} - E_x\right)\phi(\boldsymbol{r}_e, \boldsymbol{r}_h) = 0. \tag{2.11}$$

$\phi(\boldsymbol{r}_e, \boldsymbol{r}_h)$ is the Fourier transform of the pair wave function $C^{S,S_z}_{\boldsymbol{k}',\boldsymbol{k}''}$

$$\phi(\boldsymbol{r}_e, \boldsymbol{r}_h) = \sum_{\boldsymbol{k}',\boldsymbol{k}''} C^{S,S_z}_{\boldsymbol{k}',\boldsymbol{k}''} \exp\{i(\boldsymbol{k}'\boldsymbol{r}_e + \boldsymbol{k}''\boldsymbol{r}_h)\}, \tag{2.12}$$

where we have included the screening of the Coulomb potential by the static dielectric constant ε_0. m_e and m_h are the effective masses of the electrons and holes respectively. The spectrum of the bound states is given by

$$E_x = E_g - \frac{e^2}{2\varepsilon_0 a_0}\frac{1}{n^2} + \frac{\hbar^2 k^2}{2m_x}, \tag{2.13}$$

where

$a_0 = \hbar^2\varepsilon_0/\mu_x e^2$ is the exciton Bohr radius,

$\mu_x = m_e \cdot m_h/m_x$ is the reduced exciton mass,

$m_x = m_e + m_h$ is the total exciton mass,

and

$e^2/2\varepsilon_0 a_0 = E_x^R$ is the exciton Rydberg.

Normally, transversal singlet excitons are strongly coupled to the light field. Hopfield [2.11] showed that the Hamiltonian of the interacting exciton–photon system can be diagonalized by a linear transformation. By this transformation one finds new quasiparticles, which are mixed exciton–photon states, called (excitonic) polaritons.

The exciton operator

$$t^+_{k,n} = \sum_{\boldsymbol{k}',\boldsymbol{k}''} C^{0,0}_{\boldsymbol{k}',\boldsymbol{k}''} p^{0,0}_{\boldsymbol{k}',\boldsymbol{k}''} \delta(\boldsymbol{k} - \boldsymbol{k}' - \boldsymbol{k}'') \tag{2.14}$$

can be shown to obey Bose commutation relations in the limit of low exciton densities n_x. $\boldsymbol{k}$ is the exciton momentum, n is the main quantum number of the internal motion.

The Hamiltonian for the transversal excitons in the ground state $n = 1s$ and of the photons is

$$H = \sum_{\boldsymbol{k}} E_t(\boldsymbol{k}) t_{\boldsymbol{k}}^+ t_{\boldsymbol{k}} + \sum_{\boldsymbol{k}} \hbar\omega_{\boldsymbol{k}} c_{\boldsymbol{k}}^+ c_{\boldsymbol{k}} + \sum_{\boldsymbol{k}} \frac{\pi\tilde{\beta} E_t^2(\boldsymbol{k})}{\hbar\omega_{\boldsymbol{k}}} (c_{\boldsymbol{k}}^+ + c_{-\boldsymbol{k}})(c_{-\boldsymbol{k}}^+ + c_{\boldsymbol{k}})$$

$$+ \mathrm{i} \sum_{\boldsymbol{k}} \frac{(\pi\tilde{\beta})^{1/2} E_t(\boldsymbol{k})^{3/2}}{(\hbar\omega_k)^{1/2}} (t_{\boldsymbol{k}} + t_{-\boldsymbol{k}}^+)(c_{-\boldsymbol{k}} + c_{\boldsymbol{k}}^+), \tag{2.15}$$

where $\omega_{\boldsymbol{k}} = ck/\sqrt{\varepsilon_\infty}$ and $\tilde{\beta} = \hat{\beta}/\varepsilon_\infty$. ε_∞ is the high-frequency limit of the dielectric constant, $\hat{\beta}$ is the polarizability of the exciton, $c_{\boldsymbol{k}}$ and $c_{\boldsymbol{k}}^+$ are the photon creation and annihilation operators, respectively.

This Hamiltonian can be diagonalized by a linear transformation to polariton operators $\alpha_{\boldsymbol{k}}$

$$\alpha_{\boldsymbol{k}} = u c_{\boldsymbol{k}} + v t_{\boldsymbol{k}} + w c_{-\boldsymbol{k}}^+ + z t_{-\boldsymbol{k}}^+. \tag{2.16}$$

The resulting eigenfrequencies of the polaritons obey the following dispersion relation

$$(\hbar\omega_{\boldsymbol{k}}/E)^2 = 1 + 4\pi\tilde{\beta}/(1 - (E/E_t)^2). \tag{2.17}$$

The four solutions are given by

$$E_1(\boldsymbol{k}) = \frac{1}{\sqrt{2}} \{(\hbar\omega_{\boldsymbol{k}})^2 + E_t^2(1 + 4\pi\tilde{\beta}) - R\}^{1/2},$$

$$E_2(\boldsymbol{k}) = \frac{1}{\sqrt{2}} \{(\hbar\omega_{\boldsymbol{k}})^2 + E_t^2(1 + 4\pi\tilde{\beta}) + R\}^{1/2},$$

$$E_3(\boldsymbol{k}) = -E_1(\boldsymbol{k}) \quad \text{and} \quad E_4(\boldsymbol{k}) = -E_2(\boldsymbol{k})$$

with

$$R = [((\hbar\omega_{\boldsymbol{k}})^2 + E_t^2(1 + 4\pi\tilde{\beta}))^2 - 4(\hbar\omega_{\boldsymbol{k}} E_t)^2]^{1/2}. \tag{2.18}$$

E_1 and E_2 give the energies of the lower and upper polariton branch (fig. 4). The knee in the lower polariton branch is called the bottle-neck region. Here, the rates for scattering of polaritons by phonon emission to lower energies become rather small [see e.g. 2.29]. Via the Lydane–Sachs–Teller relation the split between the longitudinal and transverse excitons is given by

$$E_l(0)/E_t(0) = \sqrt{1 + 4\pi\beta}. \tag{2.19}$$

The polariton operators of the lower and upper branches are $\alpha_{\boldsymbol{k},1}$ and $\alpha_{\boldsymbol{k},2}$, respectively. The full transformation from the exciton-photon operators to the polariton operators can be expressed by

$$\hat{p}_{\boldsymbol{k},i} = \sum_j C_{ij} (x\hat{p})_{\boldsymbol{k},j}, \tag{2.20}$$

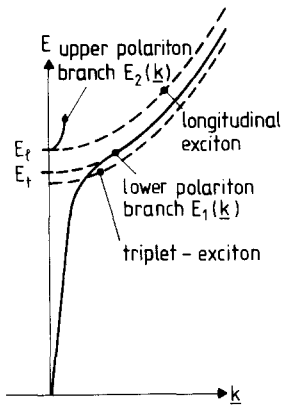

Fig. 4. A schematic drawing of the dispersion curves of the lower and upper polariton branches ($E_1(\boldsymbol{k})$ and $E_2(\boldsymbol{k})$), respectively, and of the longitudinal and the triplet excitons. Only the states for the main quantum number $n = 1$ are shown.

where the four components of the polariton operators are $\hat{p}_{\boldsymbol{k},1} = \alpha_{\boldsymbol{k},1}$, $\hat{p}_{\boldsymbol{k},2} = \alpha_{\boldsymbol{k},2}$, $\hat{p}_{\boldsymbol{k},3} = \alpha^{+}_{-\boldsymbol{k},3}$ and $\hat{p}_{\boldsymbol{k},4} = \alpha^{+}_{-\boldsymbol{k},4}$, while the four exciton-photon operators are

$$(x\hat{p})_{\boldsymbol{k},1} = c_{\boldsymbol{k}}, \quad (x\hat{p})_{\boldsymbol{k},2} = t_{\boldsymbol{k}}, \quad (x\hat{p})_{\boldsymbol{k},3} = c^{+}_{-\boldsymbol{k}}, \quad (x\hat{p})_{\boldsymbol{k},4} = t^{+}_{-\boldsymbol{k}}.$$

The reverse transformation is given by the matrix

$$C^{-1} = \begin{pmatrix} C^*_{11} & C^*_{21} & -C^*_{31} & -C^*_{41} \\ C^*_{12} & C^*_{22} & -C^*_{32} & -C^*_{42} \\ -C^*_{13} & C^*_{23} & C^*_{33} & C^*_{43} \\ -C^*_{14} & C^*_{24} & C^*_{34} & C^*_{44} \end{pmatrix}. \tag{2.21}$$

The elements of the Hopfield transformation are given by

$$C_{\substack{11 \\ (13)}} = \begin{matrix} + \\ (-) \end{matrix} \frac{(1-(E_1/E_t)^2)(\hbar\omega_{\boldsymbol{k}}/E_t \begin{matrix} + \\ (-) \end{matrix} E_1/E_t)}{2\sqrt{\hbar\omega|E_1|/E_t}A} \tag{2.22}$$

and by

$$C_{\substack{12 \\ (14)}} = -\frac{\mathrm{i}\sqrt{\pi\tilde{\beta}}(1 \begin{matrix} + \\ (-) \end{matrix} E_1/E_t)}{\sqrt{E_1/E_t}\cdot A}, \tag{2.23}$$

where

$$A = \sqrt{(1-(E_1/E_t)^2)^2 + 4\pi\tilde{\beta}}. \tag{2.24}$$

The other coefficients C_{jl} can be obtained from C_{1l} by

$$C_{ji} = (-1)^{s_j/2} C_{1i}(E_1 \to E_j), \tag{2.25}$$

where one has to replace E_1 by E_j in the expression for C_{1j} [see e.g. (2.12)]. The exponents s_j are $s_1 = 0$, $s_2 = 1$, $s_3 = 2$, $s_4 = 1$.

The polariton Hamiltonian is now given by

$$H = \sum_{k,i=1,2} E_i(\boldsymbol{k}) \alpha^+_{ki} \alpha_{ki}. \tag{2.26}$$

In the treatment of the optical properties of HES the use of the polariton picture simplifies the calculation of the spectra essentially.

2.3. Excitonic polaritons in real crystals

The twofold degenerate conduction band and the six valence bands give rise to a rich structure of the exciton or polariton levels in real crystals. The possible symmetries at (or close to) the Γ-point are found from the reduction of the direct product of the irreducible representations of the conduction band, of the valence bands and of the envelope function

$$\Gamma^{\text{cond}} \otimes \left(\sum \Gamma^{\text{hole}} \right) \otimes \Gamma^{\text{env}} = \sum_i a_i \Gamma_i^{\text{exciton}}; \qquad a_i = 0, 1, 2, \ldots \tag{2.27}$$

We restrict ourselves to the exciton states, with main quantum number $n = 1$, i.e., with a Γ_1 envelope function. Therefore, we obtain twelve exciton levels i.e. $\Sigma\, a_i g_i = 12$, where g_i gives the degeneracy of the irreducible representation Γ_i. See table 3.

In T_d symmetry the Γ_5 levels are optically dipole-allowed as well as the Γ_5 and Γ_1 levels for $\boldsymbol{E} \perp \boldsymbol{c}$ and $\boldsymbol{E} \parallel \boldsymbol{c}$, respectively, in C_{6v} symmetry. The dipole-allowed levels are generally coupled strongly to the electromagnetic field, giving rise to a polariton effect (see subsections 2.2 and 4.4). Some of the dipole-allowed levels involve a spin flip, however, (e.g. the A_{Γ_1} or the C_{Γ_5} triplet excitons in ZnO) which drastically reduces their oscillator strengths.

The degeneracy of the valence bands not only gives rise to a large number of exciton levels, but implies, together with the symmetry breaking effects at $\boldsymbol{k} \neq 0$ which have been neglected until now, additional complications: it is, e.g., generally no longer possible to separate the relative motion of the electron and the hole from the motion of the center of mass. Furthermore, different states are mixed

Table 3
Possible symmetries of the exciton groundstates ($n = 1$) in T_d and C_{6v} symmetries

Symmetry T_d		Symmetry C_{6v}	
$\Gamma_6^{\text{cond}} \otimes \Gamma_8^{\text{val}} \otimes \Gamma_1^{\text{env}} = \Gamma_3 + \Gamma_4 + \Gamma_5$		$\Gamma_7^{\text{cond}} \otimes \Gamma_9^{\text{val}} \otimes \Gamma_1^{\text{env}} = \Gamma_5 + \Gamma_6$	
$\Gamma_6^{\text{cond}} \otimes \Gamma_7^{\text{val}} \otimes \Gamma_1^{\text{env}} = \Gamma_2 + \Gamma_5$		$\Gamma_7^{\text{cond}} \otimes \Gamma_7^{\text{val}} \otimes \Gamma_1^{\text{env}} = \Gamma_1 + \Gamma_2 + \Gamma_5$	
		$\Gamma_7^{\text{cond}} \otimes \Gamma_7^{\text{val}} \otimes \Gamma_1^{\text{env}} = \Gamma_1 + \Gamma_2 + \Gamma_5$	
Exciton symmetry	degeneracy g_i	exciton symmetry	degeneracy g_i
Γ_3	2	A-excitons Γ_6	2
Γ_4	3	A-excitons Γ_5	2
Γ_5	3	B-excitons Γ_1	1
Γ_2	1	B-excitons Γ_2	1
Γ_5	3	B-excitons Γ_5	2
		C-excitons Γ_1	1
		C-excitons Γ_2	1
		C-excitons Γ_5	2

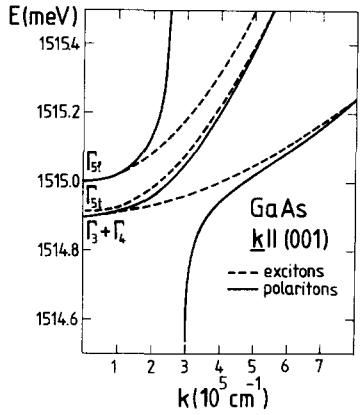

Fig. 5. Dispersion curves of the excitons and the excitonic polaritons calculated for GaAs at $T = 0$ K (from Rössler [2.13]).

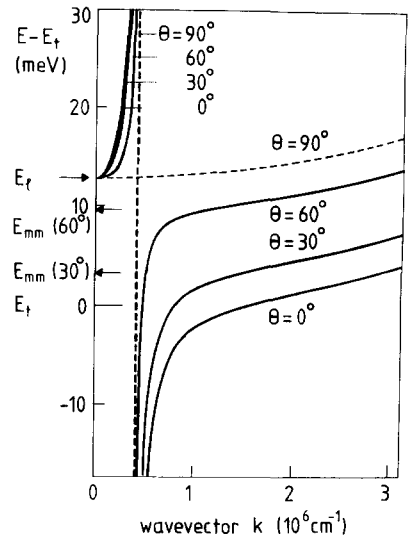

Fig. 6. Dispersion curves for ordinary and mixed-mode polaritons. The latter appear in uniaxial crystals if the polarization is in the principal section (the plane defined by the wavevector $\boldsymbol{k}$ and the crystallographic $\boldsymbol{c}$-axis) and if the angle $\theta = \sphericalangle(\boldsymbol{k}, \boldsymbol{c})$ is neither 0° nor 90° (from Hümmer [2.15]).

which leads to a weakening of the selection rules given above. Originally dipole-forbidden states may receive a generally momentum-dependent admixture of states with dipole-allowed symmetry and are thus giving rise to a more or less pronounced polariton effect.

A detailed discussion of these problems is beyond the scope of this article and we restrict ourselves to two examples. For detailed information the reader is referred to the recent review articles of Rössler and of Cho [2.13, 2.14] and the literature cited therein.

Fig. 5 shows the dispersion curves of excitons and polaritons in GaAs according to [2.13]. The occurence of a light and a heavy hole-band is reflected in a light and a heavy exciton branch. The participation of the originally dipole-forbidden Γ_3 and Γ_4 levels in the polariton effect can also be seen clearly. The $\boldsymbol{k}$-linear terms are negligible in GaAs [3.13] and therefore the Γ_3 and Γ_4 levels do not split away from the Γ-point, in contrast e.g. to CuBr (see section 4.4).

In addition to the peculiarities indicated above, there is another speciality in the wurtzite type compounds, caused by their uniaxial crystal structure: In the cubic T_d compounds, the excitonic polarization can always be decomposed in parts perpendicular and parallel to the wavevektor $\boldsymbol{k}$, i.e. in transverse and longitudinal contributions, respectively, at least as long as $\boldsymbol{k}$-induced mixing is neglected. In uniaxial crystals, the quantization axis is given by the $\boldsymbol{c}$-axis. If an exciton is polarized in the principle section (i.e. in the plane defined by $\boldsymbol{c}$ and $\boldsymbol{k}$) and if $\boldsymbol{c}$ and $\boldsymbol{k}$ are neither parallel nor perpendicular, then so-called mixed mode polaritons are formed [2.15] which exhibit a dispersion curve situated between the pure longitudinal and the pure transverse case, depending on the angle $\theta = \sphericalangle(\boldsymbol{c}, \boldsymbol{k})$. They correspond to the extraordinary beam in classical crystal optics. A schematic drawing taken from [2.15] is shown in fig. 6.

2.4. Biexcitons

Since excitons in semiconductors can be understood in analogy to the hydrogen atom, one can expect, that excitonic molecules or biexcitons (m) may exist in the same way as H_2 molecules. Because

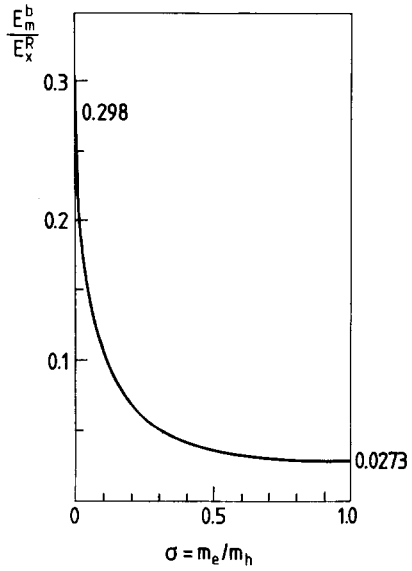

Fig. 7. The ratio of biexciton binding energy E_m^b and the exciton Rydberg E_x^R as a function of $\sigma = m_e/m_h$ (from Akimoto and Hanamura [2.16]).

in a semiconductor the masses of the positive and negative carriers are of the same order of magnitude and since they are imbedded in a polarizable medium, it is not obvious from first principles, that the biexciton can exist as a bound state in all semiconductors. Bound state means, that the energy of the biexciton E_m at $\boldsymbol{k} = 0$ lies a finite binding energy E_m^b below two times the energy of the lowest free exciton (generally a triplet exciton) E_x.

Variational calculations for E_m^b (measured in units of the exciton Rydberg E_x^R) have been performed as a function of the mass ratio $\sigma = m_e/m_h$ [2.16, 2.17]. They give a lower limit of E_m^b/E_x^R and indicate, that the biexciton is bound in all semiconductors (see fig. 7). A calculation using the Feynman path integral method gave qualitatively the same result, but yielded significant larger values of E_m^b especially around $\sigma = 1$ [2.18]. An investigation of the symmetry of the simple four particle effective mass Hamiltonian indicated, that $E_m^b(\sigma) = E_m^b(1/\sigma)$ and that $E_m^b(\sigma)/E_x^R$ is a monotonously decreasing, concave function in the interval $0 < \sigma < 1$ with slope zero for $\sigma = 1$ [2.19].

Some calculations made for selected substances yield binding energies which partly deviate considerably from the values deduced from the more general but simpler calculations. Nevertheless, they also indicate that the biexciton is a bound state. The carrier–phonon interaction seems to stabilize the biexciton further [2.20–2.22].

2.5. Plasmons

At very high excitation intensities bound pair states are no longer stable. In the higher temperature range excitons ionize due to the screening of the e–h Coulomb interation at the Mott density, while at low temperatures a phase transition into a degenerate metallic Fermi liquid occurs. Therefore, at very high excitation intensities one generates a plasma. The two basic phenomena occuring in a plasma are the screening of the Coulomb interaction between charged carriers and the appearance of the collective mode in the form of plasma oscillations. Both effects can be obtained from the intraband dielectric function, which in the random phase approximation (RPA) is given by the Lindhard-formula [see e.g. 2.23]

$$\varepsilon(\boldsymbol{k},\omega)=1+V_{\boldsymbol{k}}\sum_{i,\boldsymbol{k}'}\frac{(n_{-\boldsymbol{k}',i}-n_{\boldsymbol{k}',i})}{\hbar\omega-E_{\boldsymbol{k}'-\boldsymbol{k},i}-E_{\boldsymbol{k}',i}}, \tag{2.28}$$

$n_{\boldsymbol{k},i}$ are the Fermi distribution functions in the band i. This intraband dielectric function determines the screened Coulomb potential $V_s(\boldsymbol{k},\omega)=V(\boldsymbol{k})/\varepsilon(\boldsymbol{k},\omega)$ and also the frequency of the plasmons, which can be obtained from $\varepsilon(\boldsymbol{k},\omega)=0$. Fig. 8 shows the dispersion of the plasmon frequency together with the continuum of the pair excitations (shaded region) in a simple one-band model. When the plasmon mode enters into the continuum of pair excitations, the plasmons can decay into individual pair excitations. Therefore, the plasmons are strongly damped in this region. In a real semiconductor the range of pair excitations is more extended due to the existence of several valence bands. The intervalence band transitions cause a damping of the plasmons in real semiconductors [2.24].

The RPA dielectric function can be simplified by the plasmon-pole approximation, which yields the correct long-wavelength and static limit of eq. (2.28), respectively, and gives a useful extrapolation elsewhere. According to Lundquist [2.25], Zimmermann [2.26] and Rice [2.27], the plasmon-pole approximation for the dielectric function of an e–h plasma is given by:

$$\left.\begin{aligned}
&\varepsilon(\boldsymbol{k},\omega)=\varepsilon_0\left(\frac{\omega^2-\omega_{\boldsymbol{k}}^2}{\omega^2-\omega_{\boldsymbol{k}}^2+\omega_{\mathrm{pl}}^2}\right),\\
&\text{where}\\
&\omega_{\boldsymbol{k}}^2=\omega_{\mathrm{pl}}^2\left(1+\frac{\boldsymbol{k}^2}{k_{\mathrm{TF}}^2}\right)+\frac{\hbar^2}{2}\left(\frac{\boldsymbol{k}^2}{2\mu_x}\right)^2\\
&\omega_{\mathrm{pl}}^2=\left(\frac{4\pi ne^2}{\varepsilon_0\mu_x}\right)\\
&k_{\mathrm{TF}}^2=4\pi(e^2/\varepsilon_0)\sum_{i=\mathrm{e,h}}\left(\frac{\partial n_i}{\partial\mu_i}\right)_{\mathrm{T}},
\end{aligned}\right\} \tag{2.29}$$

with $n_e=n_h=n$.

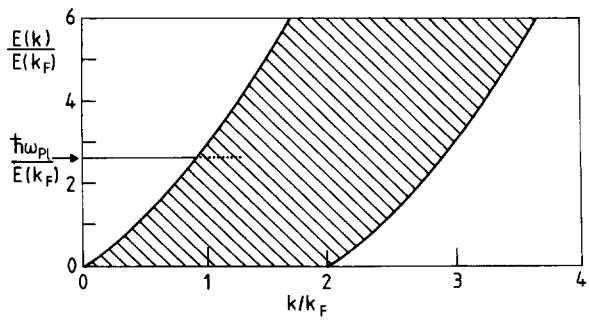

Fig. 8. Dispersion curve of the plasma mode and of pair excitations in a one-band model. Wavevectors $\boldsymbol{k}$ are given in units of the Fermi vector, energies are given in units of the Fermi energy. The shaded area indicates the region where individual pair excitations are possible. The plasmons are strongly damped in this region.

Here, μ_x is the reduced e–h mass, k_{TF} is the inverse Thomas–Fermi screening length and μ_i the chemical potential of the electrons or the holes. In this description the lattice polarizability is taken into account by the static dielectric constant ε_0.

However, in strongly ionic semiconductors the lattice polarizability has to be treated dynamically (see section 5.1). The use of the plasmon-pole approximation simplifies the calculations of many-particle effects in the plasma considerably. Sometimes, e.g., in line-shape calculations, it is also important to take the damping of the effective plasma oscillation into account. This modification is described and used in subsection 5.1.3.

3. Experimental methods

The first part of this section gives some general arguments on the conditions under which an excitation source is suitable for the investigation of HES. In the second part some special setups are discussed.

3.1. General considerations

In order to observe HES effects, it is necessary that the electronic excitations interact with each other at a sufficiently high rate. The short lifetime and diffusion path in direct gap materials necessitate a rather high density n of bound (excitons) or unbound electronic excitations. A value of $n = 10^{17}\,\mathrm{cm}^{-3}$ is a reasonable average, though the onset of HES effects depends strongly on the compounds under investigation, on the "quality" of the individual sample and on the special conditions of the experiment.

The lifetime of excitons τ in direct gap materials is about 1 ns at low densities [e.g. 3.1]. It is reduced at high densities by quadratic recombination processes and stimulated emission to values around 0.1 ns*.

The generation rate G, which is needed to obtain a stationary concentration of $n = 10^{17}\,\mathrm{cm}^{-3}$ e–h pairs with a lifetime of 10^{-10} s is at least $G \simeq 10^{27}\,\mathrm{cm}^{-3}\,\mathrm{s}^{-1}$.

G has now to be connected with the excitation intensity I_{exc}, where I_{exc} is the energy per units of area and time impinging on the sample.†

In the case of nonresonant two-photon band-to-band excitation of semiconductors for which the absorption edge $\hbar\omega_{ed}$ fulfills the inequality $2\hbar\omega_{exc} > \hbar\omega_{ed} > \hbar\omega_{exc}$, the relation between G and I_{exc} reads

$$I_{exc} = \left(\frac{G \cdot 2\hbar\omega_{exc}}{K_2}\right)^{1/2}, \tag{3.1}$$

where K_2 is the two-photon absorption coefficient. Since K_2 is of the order of $10^{-7}\,\mathrm{W}^{-1}\,\mathrm{cm}$ for many direct gap materials (see table 4) I_{exc} has to be about $2 \times 10^7\,\mathrm{W\,cm}^{-2}$ in order to observe HES effects. In real experiments I_{exc} is varied from $10^5\,\mathrm{W\,cm}^{-2}$ to $10^8\,\mathrm{W\,cm}^{-2}$, where the upper limit is given by the threshold for destroying the sample surface.

The excitation by two-photon absorption (TPA) is especially useful if a homogeneous bulk excitation

* Strictly, it is not allowed to speak about lifetime in the case of a nonexponential decay. The 0.1 ns given here corresponds to some average or effective lifetime.

† Some authors prefer to give the photon flux density I_{Ph} instead of I_{exc} in the case of optical excitation. They are connected by $I_{exc} = I_{Ph} \cdot \hbar\omega_{exc}$. Thus, $I_{exc} \simeq 10^6\,\mathrm{W\,cm}^{-2}$ with a N_2-laser ($\hbar\omega_{exc} = 3.78$ eV) corresponds to $I_{Ph} = 1.7 \times 10^{24}\,\mathrm{cm}^{-2}\,\mathrm{s}^{-1}$.

Table 4
Two photon absorption coefficients K_2 of some direct gap materials for ruby laser light ($\hbar\omega_{exc} = 1.785$ eV). The values given here are measured at 300 K. They are almost temperature independent. c gives the optical axis, $\boldsymbol{E}$ and $\boldsymbol{k}$ are the electric field and the wavevector of the photon field, respectively (from Kobbe and Klingshirn [3.2])

Substance	K_2 (W^{-1} cm)
CuCl	0.45×10^{-7}
CuBr	0.2×10^{-6}
CuJ	0.9×10^{-7}
ZnO	0.32×10^{-7} ($\boldsymbol{E} \parallel c \perp \boldsymbol{k}$)
	0.20×10^{-7} ($\boldsymbol{E} \perp c \perp \boldsymbol{k}$)
CdS	0.12×10^{-6} ($\boldsymbol{E} \parallel c \perp \boldsymbol{k}$)
	0.55×10^{-7} ($\boldsymbol{E} \perp c \perp \boldsymbol{k}$)

of rather thick samples is desired. With a standard Q-switched ruby laser volumes of several mm^3 can be pumped.

In the case of resonant TPA e.g. in some biexciton level, the values of K_2 may be some orders of magnitude higher than those for nonresonant excitation (see subsection 4.3.2).

In the case of one-photon excitation in the exciton or band-to-band region, an equation like

$$I_{exc} = G\hbar\omega_{exc}/K_1 \tag{3.2}$$

does not hold. The values of the one-photon absorption coefficient K_1 are of the order of $10^5\,cm^{-1}$ or even higher. However, the created e–h pairs do not remain confined in a surface layer of a thickness of $K_1^{-1} \leq 0.1\,\mu m$ but rapidly spread out into the volume of the crystal, driven by the gradient of the chemical potential. The effective penetration depth d_{eff} is generally assumed to be one or a few micrometers. A value of this order of magnitude has been found in CdS, where a thin platelet (about 4 μm thick) was excited by a N_2-laser from one side and the change of the excitonic reflection spectra with I_{exc} was investigated on both sides of the sample [3.3]. Therefore, equation (3.2) should rather be replaced by*

$$I_{exc} = G \cdot \hbar\omega_{exc} \cdot d_{eff}. \tag{3.3}$$

The values already used for TPA yield now $I_{exc} \simeq 5 \times 10^4\,W\,cm^{-2}$. In the experiments I_{exc} is typically varied from $10^3\,W\,cm^{-2}$ up to $5 \times 10^6\,W\,cm^{-2}$, the upper limit is again given by the damage threshold of the sample surface. With one-photon excitation it is generally possible to reach higher G values. Because of the high diffraction losses of the thin excited layers [3.4], it is partly possible to suppress the optical stimulation of recombination processes, especially if small diameters D of the excitation spot are used ($D < 100\,\mu m$).

* If fast surface recombination has to be taken into account eq. (3.3) has to be replaced by a more complicated expression. (See also discussion in subsection 5.2.1.)

Some years ago, also pulsed electron beams were in common use as excitation sources. The acceleration voltages ranged from 2×10^4 V to 2×10^5 V and the current densities on the sample reached values up to 40 A/cm^2. They were replaced, however, by optical excitation sources (i.e. lasers) for different reasons: The excitation with an electron beam is non-selective. The lattice is considerably heated, since an energy of about three times the band-gap energy is dissipated for the generation of one e–h pair [3.5]. Furthermore, the production of lattice defects cannot be excluded at the higher acceleration voltages. It is obvious, that the above mentioned excitation intensities can be applied to the samples in short pulses only. The pulse durations τ_{exc} of different excitation sources are ranging from 50 ns down to the ps region. The repetition rates have to be much smaller than τ_{exc}^{-1} to avoid heating effects. If a temporal resolution of the recombination processes is required, then τ_{exc} and the time constant of the detection system must be in the ps region. For $\tau_{exc} > 1$ ns steady state conditions are approximately realized.

It should be pointed out here, that the excitation conditions for indirect gap semiconductors are quite different from those described above. In these materials the lifetime is several orders of magnitude larger than in direct gap materials. Therefore, excitation sources with much lower values of I_{exc} and even conventional incandescent lamps may be used, either pulsed or in a continously working mode.

3.2. Some special experimental arrangements

Fig. 9 shows a setup, which allows to apply different experimental techniques for the investigation of HES. In fig. 9a, the crystal, mounted either in an evaporation- or a bath cryostat is imaged on a slit and the slit in turn is imaged on the entrance of a spectrometer. The luminescence light is then either detected by an optical multichannel analyzer or by a photomultiplier, the signal of which is fed into a boxcar integrator. With the aid of the mirrors M_1, M_2 and the microscope, it is possible to determine precisely the position of the excitation spot on the sample and to localize the place from which the luminescence is collected. This place can be the excitation spot itself or the crystal edge, where generally stimulated emission dominates.

First of all, such a setup allows to investigate the luminescence of a sample as a function of the excitation intensity I_{exc} and the bath or lattice temperature T_b or T_l, respectively. One can observe e.g. the superlinear increase of a luminescence band with I_{exc} or temperature-dependent properties such as broadening or decrease or increase of the emission intensity. Such observations can help to identify the

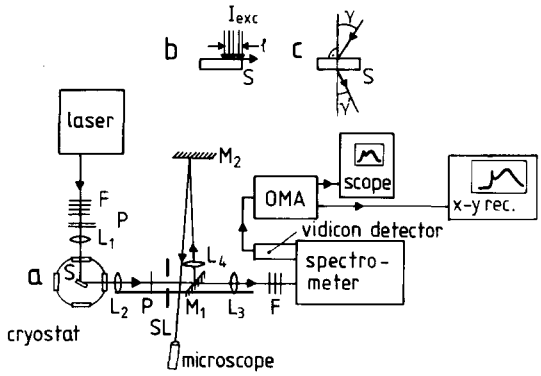

Fig. 9. An experimental setup suited e.g. for luminescence- and excitation spectroscopy (a), for gain spectroscopy (b) and for Raman spectroscopy (c). (L = lens, M = mirror, S = sample, P = polarizer, F = neutral density filter, SL = slit.)

quasiparticles which are involved in a certain scattering process. At low temperatures one preferentially observes scattering processes of weakly bound particles (e.g. biexcitons). At higher temperatures, where excitons and impurity centers are already partly ionized, scattering between free carriers and/or strongly bound particles takes place.

Examples for the experimental features sketched here and below are given in sections 4 and 5.

For excitation spectroscopy, the intensity of a luminescence structure I_{lum} is measured as a function of $\hbar\omega_{\text{exc}}$ at constant I_{exc}. I_{lum} is generally given in arbitrary units and is proportional to the area of a certain emission peak in the spectrum. Resonant excitation of certain quasiparticles, e.g. biexcitons, frequently gives rise to a distinct peak in the excitation spectrum. Since many of the HES emission shift or broaden as a function of $\hbar\omega_{\text{exc}}$, or since they may be superimposed on a $\hbar\omega_{\text{exc}}$-dependent background emission, it is in most cases absolutely necessary to evaluate the whole luminescence spectra. The frequently used method in which the spectrometer is fixed to certain $\hbar\omega_{\text{lum}}$ and the photomultiplier signal is recorded as a function of $\hbar\omega_{\text{exc}}$, may easily lead to incorrect results.

If the exciting beam is focussed to a strip of variable length L on the sample (see inset B in fig. 9), it is possible to deduce the spectral dependence of optical absorption or gain $g(\hbar\omega)$ in the excited volume from a variation of L [e.g. 3.6, 3.7], provided that both the excitation source and the sample are homogeneous. The relation between L, $I_{\text{lum}}(\hbar\omega, L)$ and $g(\hbar\omega)$ can be found by a simple integration:

$$\frac{I_{\text{lum}}(L, \hbar\omega)}{I_{\text{lum}}(L+\Delta L, \hbar\omega)} = \frac{\exp\{g(\hbar\omega)L\}-1}{\exp\{g(\hbar\omega)(L+\Delta L)\}-1} \quad . \tag{3.4}$$

An especially convenient method results from modulating the excitation strip length from L to $2L$ [3.7]. Then $g(\hbar\omega)$ is given by

$$g(\hbar\omega) = \frac{1}{L}\ln\left(\frac{I_{\text{lum}}(2L, \hbar\omega)}{I_{\text{lum}}(L, \hbar\omega)} - 1\right). \tag{3.5}$$

Since in real experiments the product $g(\hbar\omega)L$ is limited to values below approximately 5 [3.7, 3.8], care has to be taken, that the determination of the gain spectra is not falsified by saturation effects, especially if L is doubled. Since values of L below 50 μm are difficult to realize experimentally, the strip length method is limited to gain processes with $g < 10^3\ \text{cm}^{-1}$. These are especially the excitonic recombination processes discussed in section 4.

The setup in fig. 9 is also well suited for Raman spectroscopy. Since the spectral position of the Raman lines often depends strongly on the scattering configuration (see subsection 4.4), the possibility to vary the scattering angles γ and γ' has to be provided (see inset c in fig. 9).

A setup which allows to investigate the reflection and transmission spectra (absorption and gain) of a sample as a function of I_{exc} is shown in fig. 10. One uses the beam of a N_2-laser as excitation source and of a broad band dye-laser as a probe beam. Equal optical path-length and a prefocussing of the two beams on a pinhole assure spatial and temporal coincidence on the sample, which is even improved by the fact, that the dye-laser pulse is generally shorter than that of the exciting N_2-laser (e.g. $\tau_{\text{dye}} = 6$ ns, $\tau_{N_2} = 10$ ns). It is now possible to observe e.g. that the excitonic reflection or absorption structures disappear with increasing excitation (subsection 5.2) or that optical amplification (gain) sets in. If only a thin surface layer of the sample is excited, the setup of fig. 10 is useful for the observation of recombination processes yielding an optical gain above $10^3\ \text{cm}^{-1}$ as expected for the recombination in an EHP. If thicker samples are pumped homogeneously the considerations for the strip length method

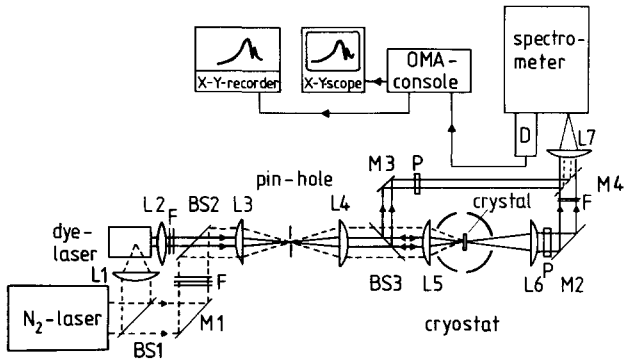

Fig. 10. An experimental setup suited e.g. for reflection- and transmission spectroscopy (BS = beam splitter, other symbols same meaning as in fig. 9). (From Bohnert et al. [3.8].)

apply. If the N_2-laser does not serve directly to excite the sample, but pumps both a broad band dye-laser and a narrow band tunable dye-laser, this setup can be used, e.g., for two-photon-absorption spectroscopy or for gain excitation spectroscopy.

For time-resolved measurements it is necessary that τ_{exc} and the time constants of the detection system are below 100 ps. A setup that fulfills this condition is shown in fig. 11. A single ps pulse of a Nd-laser ($\tau_{exc} = 30$ ps, $\hbar\omega_{exc} = 1.653$ eV) is twice frequency doubled by second harmonic generation (SHG). The 266 nm ($\hbar\omega_{exc} = 4.661$ eV) output of the second SHG crystal serves to excite the sample and is monitored by a fast vacuum photo diode. The part of the fundamental wave passing the first SHG crystal is fed into an optical delay line of variable length and then opens a fast Kerr-cell shutter consisting of the Kerr-cell and two crossed polarizers. The luminescence light transmitted through this cell is dispersed by a monochromator and detected by an optical multichannel analyzer system. An interface correlates the functions of the different moduls of this setup [3.10]. More information on picosecond spectroscopy is contained in a recent review article [1.58] and the literature cited therein. Other setups are described e.g. in [3.11–3.15].

From such time-resolved measurements predominantly informations about the decay of different emission structures are obtained. Analysing the temporal evolution of emission-, absorption- or gain

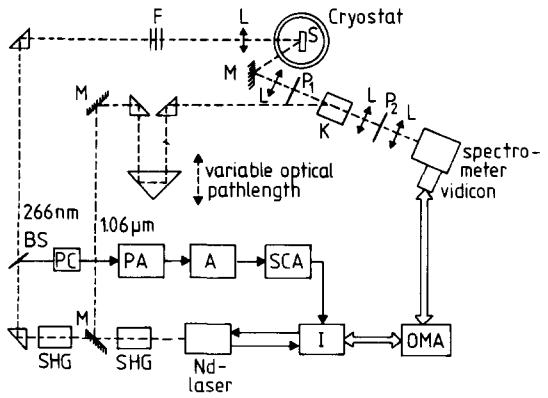

Fig. 11. An experimental setup suited for time-resolved spectroscopy (SHG = second harmonic generator, PC = photocell, PA = preamplifier, SCA = single channel analyzer, I = interface, K = Kerr-cell, other symbols same meaning as in fig. 9). (From Ostertag and Grun [3.9].)

lineshapes it is possible to get e.g. the temperature relaxation time constants of some quasiparticles. At the end of a picosecond excitation pulse the quasiparticle temperature is generally rather far above the lattice temperature, relaxing towards the latter. However, during the short lifetime of the electronic excitations often the lattice temperature is not reached.

4. Optical properties of dense excitonic systems

In this section, we are dealing with HES-effects, in which bound e–h pair states participate, i.e. we are describing the regime of moderately high excitation intensity. This regime is especially pronounced in semiconductors, which have a rather large exciton binding energy E_x^b and a correspondingly small Bohr-radius, which is however generally still larger than the lattice constant. Only in CuCl (Bohr-radius 7 Å, lattice constant 5.4 Å) one reaches the lower limit for the validity of the Wannier formalism for excitons. Large exciton binding energies are found in the II–VI compounds and especially in the copper-halides, while the excitons in the direct gap III–V compounds are bound rather weakly.

4.1. Calculation of the spontaneous and stimulated excitonic emission

In this subsection, we give a theoretical treatment of the recombination processes in dense excitonic systems. In these processes only parts of the energy of the recombining exciton leave the crystal as a photon, while the remaining energy is transfered to other excitations, such as free carriers, excitons or phonons.

These processes have first been introduced in 1968 by Benoit à la Guillaume et al. [4.1]. For theoretical treatments of these processes see [1.14, 4.1–4.9].

We discuss the following optical processes:

x–e	recombination
x–h	recombination
x–x	recombination
x–*M* LO	recombination
m_l	recombination
m_t	recombination.

These processes are schematically described in figs. 12a–d in the polariton picture:

In the x–e process, a polariton is scattered from the exciton-like part of its dispersion curve to the photon-like part, whereas a free carrier (in fig. 12a an electron) is scattered into a state with higher energy, so that in the total process energy and momentum are conserved. The photon-like polariton can leave the crystal as a luminescence photon. The approximately thermal distribution of electrons and polaritons in their bands gives rise to a certain width of the emission band*.

In the x–x recombination, the second quasi-particle is an excitonic polariton, too, which is transfered into a state with higher energy (fig. 12b).

We include in the discussion also the x–*M* LO process, i.e. the recombination of an exciton under simultaneous emission of *M* LO-phonons ($M = 1, 2 \ldots$), (fig. 12c), though this is not a HES-effect in the sense of our definition, since the corresponding emission-bands may be observed even at the lowest

* In contrast to these inelastic scattering processes, elastic scattering is investigated e.g. in [4.214].

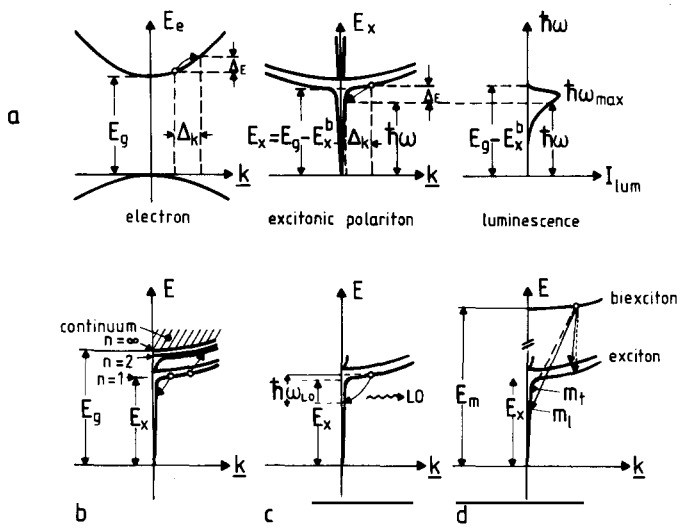

Fig. 12. A schematic representation of various excitonic recombination processes which yield optical gain. In the first row (a), the exciton–electron scattering is sketched in some detail. An electron is scattered into a state of higher kinetic energy ($\Delta E, \Delta k$) and an excitonic polariton is scattered from the exciton-like branch under energy and momentum conservation on the photon-like one, leaving the crystal as a luminescence photon. The thermal distribution of electrons and polaritons in their bands give rise to a broad luminescence band. In the second row, three other recombination processes are depicted schematically: the inelastic scattering between two exciton-like polaritons (b), the recombination of an exciton-like polariton by the emission of a LO-phonon (c) and the decay of a biexciton in a exciton-like- and a photon-like polariton, respectively (d). The transitions to the transvers- and longitudinal exciton state give rise to the m_t and m_l luminescence bands, respectively.

excitation intensities. On the other hand, also the x–*M* LO process gives rise to optical gain, especially if large crystal volumes are pumped homogeneously by two-photon excitation (TPE). Under this condition, the x–*M* LO recombination can dominate the luminescence spectra up to the highest I_{exc}.

In the m_l or m_t processes a molecule decays into a photon-like polariton and into a longitudinal exciton or into an exciton-like polariton on the lower branch, respectively (fig. 12d).

The gain spectra and the spectra of the spontaneous recombination for all these processes can be obtained most directly from a laser theory [4.9, 4.10] which makes use of the polariton concept. In the framework of this theory one formulates rate equations for the polaritons and all the other excitations which are involved in the considered recombination process. The quantum-mechanical derivation of these rate equations has been described in detail in refs. [4.9, 4.10]. The derivation contains the following steps:

(a) Construct an effective Hamiltonian for the system of interacting free carriers, excitons, excitonic molecules and photons from the basic two-band Hamiltonian.

(b) Eliminate from this Hamiltonian transverse excitons and photons by a Hopfield-transformation and thereby introduce the polaritons.

(c) Calculate the equations of motion for the creation and annihilation operators of free carriers, longitudinal excitons, polaritons and biexcitons.

(d) Include damping terms due to excitation, spontaneous emission and other losses, and introduce the corresponding quantum noise operators. By these means, one obtains the quantum mechanical Langevin equations.

(e) Derive rate equations from the Langevin equations by an adiabatic elimination of the transition operators.

(f) The resulting rate equations for the polaritons are decoupled into a rate equation for the photon-like polaritons and one for the exciton-like polaritons. Quasi-equilibrium assumptions are made for all excitations in the crystal. Furthermore, we take into account that only the photon component of the polaritons below the bottle-neck can leave the crystal.

The mean rate equation of the laser photons is of the form

$$\frac{\mathrm{d}N}{\mathrm{d}t} = -2\kappa N + \sum \frac{2\pi}{\hbar} \delta(\Delta E)|W|^2 Q. \tag{4.1}$$

N is the number of photons in the active laser mode and 2κ is the damping coefficient of this mode. W is the effective transition matrix element for the considered scattering process, $\delta(\Delta E)$ symbolizes the energy conservation in the scattering process and Q stands for the statistical factor, which describes the population of the initial and final states. The summation is carried out over the moments of the scattered particles by taking into account the momentum conservation.

For the exciton recombination processes $|W|^2$ is given by [4.10]

$$|W|^2 = \hbar^2 |U|^2 C_{11}^2 |C_{12} - C_{14}|^2, \tag{4.2}$$

where U is the scattering matrix element for the x–e, x–h, x–x and x–LO scattering, respectively. The Hopfield coefficients $|C_{12} - C_{14}|^2$ stem from the transformation from interacting excitons to polaritons, while the factor C_{11}^2 originates from a transformation of the polaritons (below the bottle-neck) back to photons. This last transformation is necessary because only the photon-like part of the polariton can leave the crystal.

For the biexciton recombination processes $|W|^2$ is derived from the interaction matrix element U, which describes the decay of a biexciton in a photon and an exciton. For the $\mathrm{m_l}$ process $|W|^2$ is given by [4.22]

$$|W_\mathrm{l}|^2 = \hbar^2 |C_{11}|^2 |C_{11} - C_{13}|^2 |U|^2 \tag{4.3}$$

and for the $\mathrm{m_t}$ process by

$$|W_\mathrm{t}|^2 = \hbar^2 |C_{11}|^2 |(C_{11} - C_{13})(C_{12} - C_{14})U + \{\boldsymbol{k} \rightleftarrows 0\}|^2. \tag{4.4}$$

Here the expression $\{\boldsymbol{k} \rightleftarrows 0\}$ has the form of the preceding term, but the two final polariton states with momentum $\boldsymbol{k}$ and 0, respectively, are interchanged.

We list the conserved energies ΔE and the population factors Q for all excitonic recombination processes:

x–i with i = e, h:

$$\left.\begin{aligned} \Delta E &= E_{\mathrm{x},\boldsymbol{k},1} + E_{i,\boldsymbol{k}'} - E_{i,\boldsymbol{k}+\boldsymbol{k}'} - \hbar\Omega \\ Q &= n^{\mathrm{x}}_{\boldsymbol{k},1} n^{i}_{\boldsymbol{k}'} (1 - n^{i}_{\boldsymbol{k}+\boldsymbol{k}'})(1 + N) - N n^{i}_{\boldsymbol{k}+\boldsymbol{k}'} (1 - n^{i}_{\boldsymbol{k}'})(1 + n^{\mathrm{x}}_{\boldsymbol{k},1}), \end{aligned}\right\} \tag{4.5}$$

where Ω is the laser frequency, $E_{\mathrm{x},\boldsymbol{k},1}$ is the energy of the exciton in the 1s state, $n^{\mathrm{x}}_{\boldsymbol{k},1}$ and $n^{i}_{\boldsymbol{k}+\boldsymbol{k}'}$ are the

thermal population functions of the excitons and the free carriers in the different states and N finally is the number of photons in the laser mode.

x–x: Here we only consider scatterings into the $n = 2$ exciton level. This is the so-called P_2-line;

$$\left.\begin{aligned} \Delta E &= \Delta E_{x,k,1} + E_{x,k',1} - E_{x,k+k',2} - \hbar\Omega \\ Q &= n^{x}_{k,1} n^{x}_{k',1}(1 + n^{x}_{k+k',2})(1+N) - N n^{x}_{k+k',2}(1 + n^{x}_{k,1})(1 + n^{x}_{k',1}). \end{aligned}\right\} \tag{4.6}$$

x–LO:

$$\left.\begin{aligned} \Delta E &= E_{x,k,1} - \hbar\omega^{LO}_{k} - \hbar\Omega \\ Q &= n^{x}_{k,1}(1+N)(1+n^{LO}_{k}) - n^{LO}_{k} N(1+n^{x}_{k,1}). \end{aligned}\right\} \tag{4.7}$$

m_j with $j = l$ or $j = t$:

$$\left.\begin{aligned} \Delta E &= E_{m,k} - E_{x_j,-k} - \hbar\Omega \\ Q &= n^{m}_{k}(1 + n^{x_j}_{-k})(1+N) - N n^{x_j}_{-k}(1 + n^{m}_{k}). \end{aligned}\right\} \tag{4.8}$$

The term $\Sigma(2\pi/\hbar)\delta(\Delta E)|W|^2 Q$ in the photon rate equation (4.1) is now split into two parts: one which is proportional to the number N of already available photons and a second one which is the rate of spontaneous emission into the laser mode. This last term is obtained by setting $N = 0$. These two expressions give us the gain per unit time and the rate of spontaneous emission, respectively. The gain is the probability per unit time for an induced emission minus the corresponding probability for absorption of a photon. This quantity is directly related to the experimentally determined gain per unit length. The two functions only differ by a factor equal to the velocity of the light in the crystal. For all considered recombination processes the method of obtaining a positive gain is the same: One has to suppress the absorption probability by lowering the temperature so that the thermal population of the final states of the emission process (which are the initial states for the absorption process) is sufficiently small.

In the case of the x–x and the x–i recombination, the temperatures of the electronic excitations have to be low enough, so that there are no excitons in the band $n = 2$, i.e. $n^{x}_{k+k',2} \simeq 0$ or no free carriers at higher energies, i.e. $n^{i}_{k+k'} \simeq 0$, respectively. Due to the smaller effective electron mass, the condition $n^{e}_{k+k'} \simeq 0$ but $n^{e}_{k'} \neq 0$ can be realized much easier than the corresponding conditions for the population of the hole states. Therefore, the x–e recombination normally dominates in an intermediate temperature region, where we have both excitons and free carriers. Only in p-type semiconductors the x–h process can have a higher gain due to the excess concentration of holes. In the case of the x–LO recombination, the lattice temperature has to be low enough so that there are no thermal optical phonons, i.e. $n^{LO}_{k} \simeq 0$.

The decay processes of the biexcitons, have positive gain, if the molecular binding energy E^{b}_{m} is large compared to the thermal energy. This condition can easily be fulfilled in the Cu-halides CuCl and CuBr, where the biexcitons are strongly bound (see subsection 4.3.4). For a theoretical description of the gain- and absorption spectra due to biexciton decay at higher temperatures see also e.g. [4.11–

4.20, 4.22]. The question, how the gain changes if the molecular distribution becomes quantum statistically degenerate, i.e. if a nonequilibrium Bose–Einstein condensation occurs, will not be treated in the present review; for a detailed discussion see ref. [1.22].

In order to calculate the gain spectra for the various recombination processes one has to evaluate the momentum integrations numerically. The result of numerical evaluations [4.2, 4.9, 4.10, 4.22] of the gain spectra of the x–e, x–x and x–LO recombination are shown in figs. 13–15 for the example of CdS. The x–e gain spectrum has a characteristic asymmetry due to the steep transition from gain to absorption on the high energy side (fig. 13). With increasing temperature its maximum shifts stronger to lower energies than the band edge.

The x–x process gives rise to a rather symmetric gain spectrum (fig. 14) with a flat transition from gain to absorption. Again the maximum of the gain shifts to lower energies with increasing temperature.

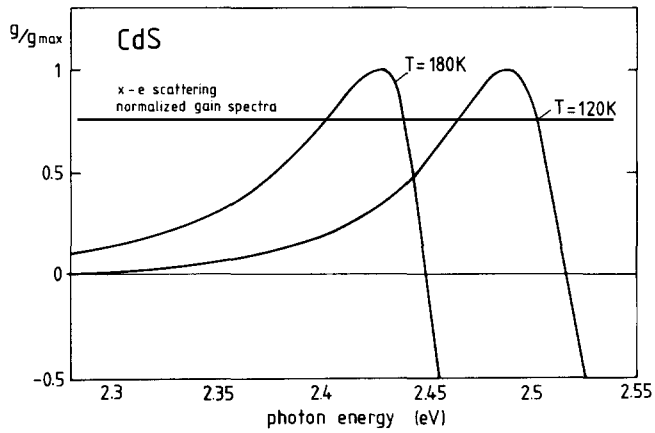

Fig. 13. Calculated gain spectra for the x–e scattering process in CdS (from Koch et al. [4.10–4.21]).

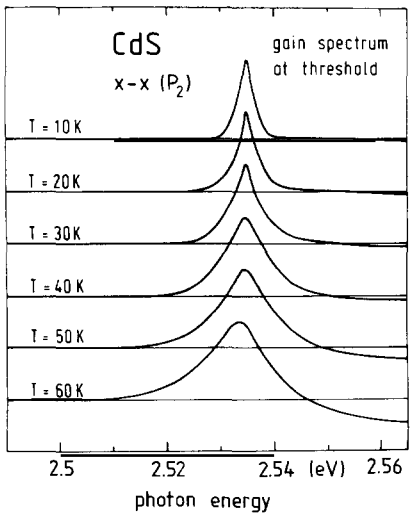

Fig. 14. Calculated gain spectra of the x–x scattering in CdS for different temperatures, including the transition to the $n = 2$ exciton states only (P_2-emission). (From Haug and Koch [4.9].)

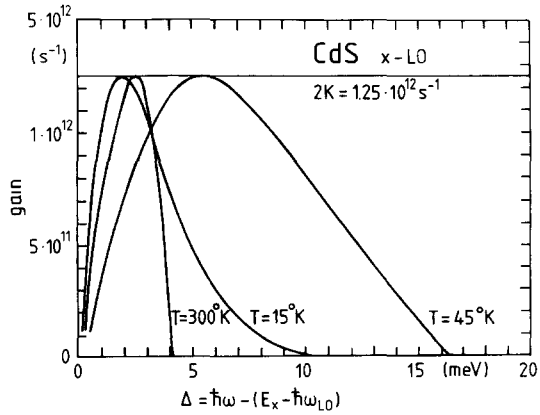

Fig. 15. Calculated gain spectra of the x-LO recombination in CdS for different temperatures (from Haug [4.2]).

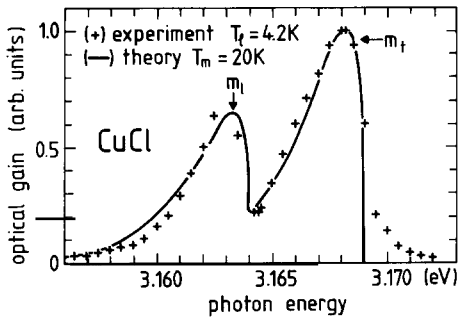

Fig. 16. Calculated gain spectrum for the m_t and m_l component of the biexciton recombination in CuCl. The influence of the polariton effect on the dispersion curve has been neglected (from Freienstein [4.22]). The crosses give an experimentally observed luminescence spectrum, recorded at a lattice temperature T_L of 4.2 K (from Ostertag [2.12, 4.15]).

The maximum of the gain spectrum of the x–LO process (fig. 15) shows a different temperature dependence. It shifts relative to the band edge first (from 15–45 K for CdS) to higher energies due to the spreading of the thermal exciton distribution. Above 45 K (for CdS) the absorption process due to the presence of thermal phonons shifts the gain maximum to lower energies with increasing temperature.

The gain spectra for the m_l and m_t recombination are plotted in fig. 16 for the example of CuCl for a temperature of the excitonic molecules T_m of 20 K [4.22]. At these temperatures the gain spectrum is nearly identical with the spectrum of spontaneous emission. The crosses give the experimentally recorded spectrum for which the lattice temperature was kept at 4.2 K. Similar results have been reported earlier, see e.g. [4.15] and [4.23].

If the maximum of the gain equals the losses 2κ in the crystal cavity, laser action sets in. The resulting exciton concentrations at the laser threshold are plotted in fig. 17 for the excitonic recombination processes in CdS. The exciton threshold concentration depends on the quality of the cavity. For low losses, the lasing of the x–LO process which is linear in the concentration of the electronic excitations, is favoured while for a cavity with high losses the quadratic recombination processes x–x and x–e have the lower threshold concentrations [4.9, 4.24, 4.25]. At temperatures above ≈60 K the x–e process has the lowest laser threshold. In fig. 18 the resulting laser thresholds are plotted for p-doped

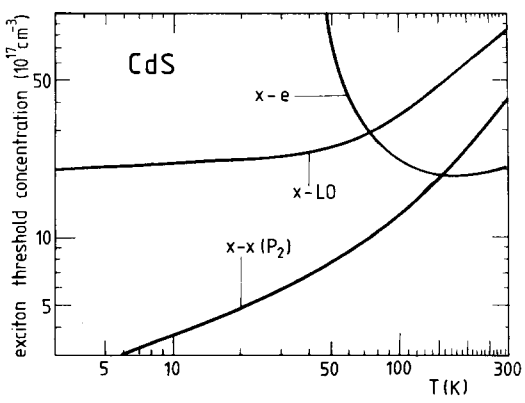

Fig. 17. Calculated temperature dependence of the exciton density at laser threshold $n_x^{th}(T)$ for different recombination processes in CdS (from Koch et al. [4.10]).

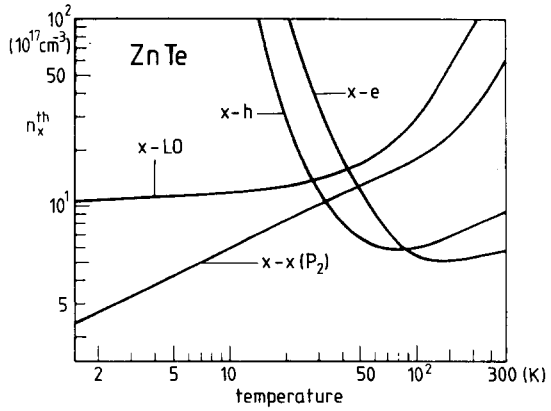

Fig. 18. Calculated temperature dependence of the exciton concentration required to reach the laser threshold $n_x^{th}(T)$ for different recombination processes in p-type ZnTe assuming an excess concentration of acceptors of 5×10^{16} cm^{-3} (from Koch et al. [4.10]).

ZnTe with an acceptor concentration of $5 \times 10^{16}\,cm^{-3}$. Fig. 18 predicts the existence of an intermediate temperature range in which the x–h recombination has the highest gain and the lowest laser threshold.

The theoretical results of this subsection will be compared with the corresponding experimental results in the following subsection.

4.2. Experimental results for the luminescence due to the inelastic scattering processes

We start the comparison between experiment and theory with a discussion of the x–*M* LO process. At low temperatures gain is easily obtained from this process. Since the corresponding gain values seem to be rather low [4.1], however, it becomes the dominant emission only, if large volumes are excited homogeneously (e.g. by TPE) and especially if in addition an external resonator is used [e.g. 4.24–4.26]. On the other hand, if small spots are excited in a thin layer only, which exhibits high diffraction losses [4.27], (e.g. by one photon-band to band excitation), then the stimulation of the x–LO process can at least partly be suppressed [4.10]. Fig. 19 shows the temperature dependence of the generation rate G_{exc}^{th} which is required to reach the laser threshold for CdS under two-photon excitation (TPE).

The experimental points nicely follow the theoretical curve, which predicts at low temperature a constant laser threshold and at higher temperatures an increase of G_{exc}^{th} due to the increasing reabsorption caused by the thermal population of the LO-phonons. At the highest temperatures, the exciton–electron-scattering has a lower threshold than the x–LO process. Similar results are also known for ZnO, with the main difference that the laser emission shifts around 115 K from the x–LO to the x–2 LO process [4.24–4.26]. Some further results about the x–LO laser emission in CdS have been published in [4.28], where especially the influence of the size and of the geometry of the excitation spot has been investigated.

The fact, that the x–LO emission is rather easily stimulated under TPE, suggests to build a tunable semiconductor laser working with this process, by incorporating the active medium in a wavelength selective resonator. In order to get a compact setup and to avoid reflection losses from many optical surfaces, a configuration as shown in the inset of fig. 20 has been used [4.26]. The sample, which is

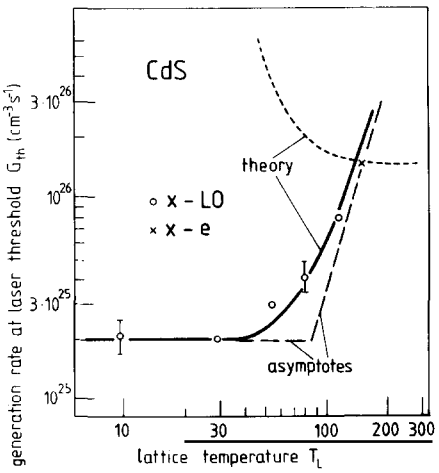

Fig. 19. Calculated and measured generation rates at laser threshold G_{th} as a function of the temperature for CdS under two-photon excitation (TPE). (From Wünstel and Klingshirn [4.26], theory from Haug [4.2] and Koch [4.21].)

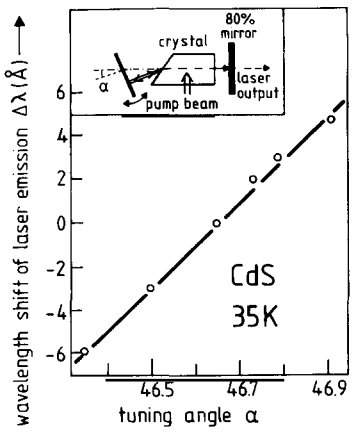

Fig. 20. Schematic plot of a tunable semiconductor laser. In a wavelength selective resonator (see inset) the spectral position of the laser emission of a semiconductor can be tuned. The experimental curve gives the detuning of the spectral position of the laser emission from its position in a non-wavelength selective resonator as a function of the detuning angle α (from Wünstel and Klingshirn [4.26]).

pumped transversely to the resonator by a standard Q-switched ruby laser, has the shape of a prism and acts simultaneously as the active and the wavelength dispersive element. The prism angle is chosen in a way that the angle β is close to the Brewster angle to avoid reflection. A 100% mirror or a total internal reflection (TIR) prism is mounted on an axis and can be tilted for wavelength selection. The lattice temperature of the crystal is chosen to get a low laser threshold and a maximum width of the gain (see fig. 15). Fig. 20 shows for CdS the detuning of the laser emission from its position in a nondispersive resonator as a function of the angle α at 35 K. An overall tuning range of 11 Å has been obtained. For ZnO similar results have been achieved [4.26]. Though the results indicate that the idea works, it should be pointed out here, that semiconductor lasers, tuned in the way illustrated above or by other methods (e.g. by temperature variation [e.g. 1.13, 4.25, 4.27, 4.29, 4.30], by the use of graded mixed crystals [e.g. 4.31–4.34] or by parametric oscillators [e.g. 4.35]), are inferior to presently commercially available dye-lasers in several respects, e.g., tuning range, efficiency, or spectral purity.

After this short excursion in connection with the LO-phonon replicas of the free excitons, let us return to the other recombination processes. The inelastic x–e scattering was extensively studied in CdS and other II–VI compounds [e.g. 1.13, 4.1, 4.4, 4.10, 4.25, 4.29, 4.30, 4.36, 4.37]. The most characteristic feature is, that the maximum of the corresponding emission band shifts with increasing lattice temperature T_L faster to lower photon energies than the band gap does (see fig. 21 and refs. [1.13, 4.3, 4.4, 4.8, 4.10, 4.25, 4.27, 4.29, 4.30, 4.36, 4.37]).

In fig. 22 measured and calculated spontaneous emission spectra are compared for ZnTe. The solid lines give the experimental results under strong N_2-laser band-to-band excitation for various tem-

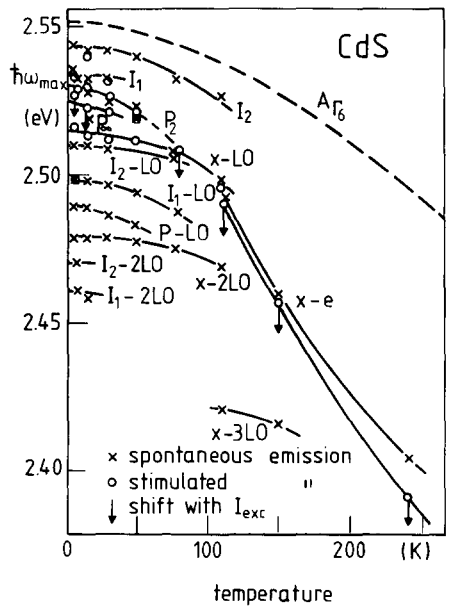

Fig. 21. The temperature dependence of the emission maxima of various luminescence bands. The spectral positions of spontaneous (×) and stimulated emission maxima (O) are given and also the shift of the latter with increasing excitation intensity I_{exc}. The processes are: the recombination of the bound excitons I_2 and I_1 with their LO-phonon replicas ($I_{1/2}$–LO and $I_{1/2}$–2 LO, respectively), the recombination of free A-excitons under emission of one or more LO-phonons (x–LO, x–2 LO and x–3 LO, respectively), the inelastic scattering between two excitons (P_2, P_∞) with their LO-phonon satellite (P–LO) and the inelastic exciton–electron scattering (x–e). While the former emission bands roughly follow the temperature variation of the free exciton (indicated by a dashed line) the x–e process shifts stronger to lower photon-energies with increasing temperature.

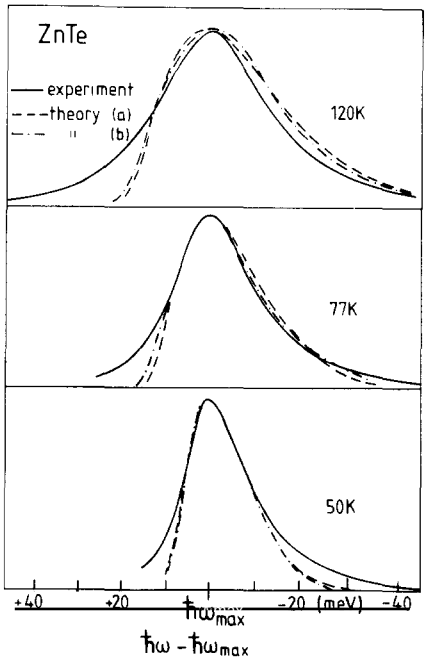

Fig. 22. Experimentally observed spontaneous luminescence spectra of ZnTe under high excitation for different temperatures, as compared to spectra calculated according to (a) Hönerlage, (b) Haug and Koch. $\hbar\omega_{max}$ corresponds to 2.365 eV, 2.355 eV and 2.340 eV ± 3 meV at 50 K, 77 K and 120 K, respectively.

peratures. The dashed and dotted lines are theoretical results for inelastic x–h scattering by Haug and Koch and by Hönerlage, respectively. One observes good agreement between both calculations and experiment, especially if one takes into account, that the high energy tail of the luminescence stems from the radiative recombination of the free excitons themselves, which is not incorporated explicitly in the calculations.

The reason why one observes x–h scattering in ZnTe at intermediate temperatures is that this material can be grown as a p-type semiconductor only, i.e. at not too high excitations one has more holes than electrons. In the typical n-type materials like CdS and ZnO, until now only x–e scattering has been reported [e.g. 1.13, 4.10, 4.25]. In a high-resistivity ZnSe sample, where the Fermi level is deep in the gap without excitation, a superposition of x–e and x–h scattering has been proposed from a lineshape analysis [4.36] (see fig. 23).

Though the emission maximum due to the scattering of the exciton with the light carrier (generally the electron) shifts with increasing lattice temperature faster to lower photon energies than in the case of an inelastic scattering with the heavy carrier, it should be pointed out here, that the superposition of both processes does not lead to the appearance of two separate maxima, but to an emission band, the maximum of which is situated between the pure cases. For this point, see also the discussion about the origin at the high excitation luminescence bands in red HgI_2 in ref. [4.38] and the literature therein. Gain spectra for the x–e scattering have been reported for CdS in ref. [4.39]. The agreement with theory is reasonably good.

The inelastic x–x scattering is expected to be seen preferentially at lower temperatures, where the excitons are not thermally dissociated. This process has been observed at intermediate excitation levels in all II–VI compounds investigated so far, e.g. [1.13, 1.17, 4.10, 4.18, 4.24, 4.28, 4.36, 4.37, 4.40–4.45] and in

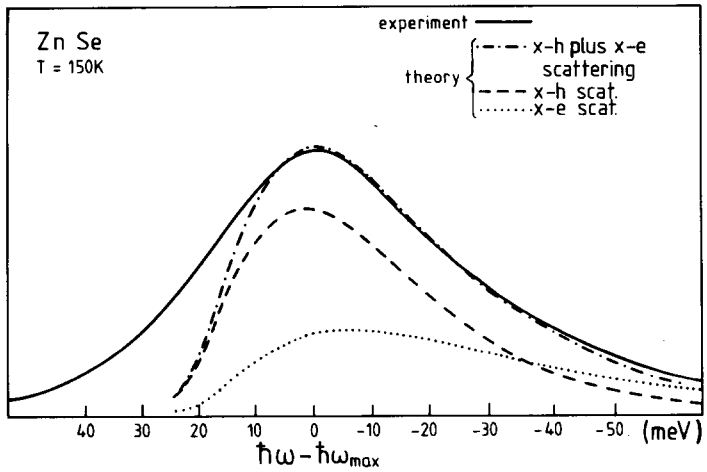

Fig. 23. Experimentally observed luminescence spectrum of ZnSe under high excitation, as compared to a calculated superposition of x–e and x–h scattering. $\hbar\omega_{max}$ corresponds to 2.75 eV (from Maier and Klingshirn [4.36]).

GaAs [4.46–4.48], though the distinction between x–e and x–x scattering is not easy in the latter material, because of the small exciton binding energy. In the Cu-halides, there is not much reliable information about this process [4.49]. In these materials biexciton formation is more likely than inelastic x–x scattering if two excitons collide.

The inelastic x–x scattering manifests itself in the luminescence spectra of HES by an emission band, which is displaced from the position of the free exciton to lower energies by approximately one exciton binding energy. These so called P-bands often exhibit a fine-structure. The spectral positions of the peaks P_n can generally be described in good approximation by

$$\hbar\omega_{max} = E_g - E_x^b(1 - 1/n^2); \qquad n = 2, 3, \ldots \infty. \tag{4.9}$$

This formula follows immediately from fig. 12 if energy conservation and a hydrogen-like exciton series are assumed and if the kinetic energy is neglected. Fig. 24 shows the P_n-lines for ZnO.

The fact, that the P_n-lines are often rather broad (up to 5–10 meV) even at low lattice temperature T_L, can be explained by the kinetic energy of the excitons, which may be described by an exciton temperature T_x which is higher than the lattice temperature T_L * or possibly by a dynamic variation of E_x^b during the excitation pulse in the high density exciton-gas [4.37]. For time-resolved measurements in the P-bands see [4.50–4.56]. In principle, the P emission band could extend to energies far below $E_g - 2E_x^b$ if one of the excitons is scattered high into the continuum. The scattering matrix element seems to decrease however rather rapidly with increasing energy transfer and thus the intensity of the P-bands decreases below P_∞ [4.57].

Though a recombination process which involves an inelastic x–x intraband-scattering – a P_1-line – should also be possible, there are not much experimental indications for such a process [4.8, 4.48].

The x–x recombination process is not only observed in the luminescence, but also in the gain spectra [e.g. 4.9, 4.28, 4.58, 4.59]. Since the gain values of this process are generally below $10^3\,cm^{-1}$, the

* For $T_L = 4$ K a value of T_x between 20 and 30 K is often realistic.

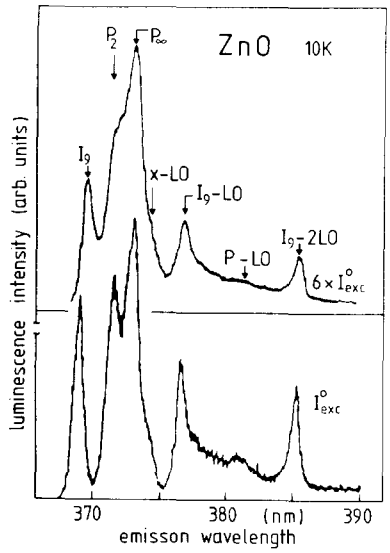

Fig. 24. Luminescence spectra of ZnO under high electron beam excitation, showing the x–x scattering bands P_2 and P_∞, the bound exciton recombination line I_9, as well as LO-phonon replica of I_g, of the free exciton and the P-bands (from Hvam [4.40]).

strip length method is adequate. Fig. 25 gives an example for CdS in which the P_2 and P_3 bands are nicely resolved.

All of the scattering processes depicted in fig. 12 are capable to show laser emission; the temperature dependence of the laser thresholds of the various processes has been studied in CdS under one-photon band-to-band excitation. Fig. 26 gives the excitation intensity at the laser threshold I^{th}_{exc} for different processes as a function of temperature in CdS. Below 80 K the x–x scattering bands P_2 and P_3 are observed; they exhibit a threshold which increases with temperature. Above 100 K, the x–e scattering is observed. Its threshold passes through a minimum around 150 K. The x–LO process shows up only at the highest I_{exc} under the present experimental condition. For comparison the calculated laser thresholds are given by the dashed lines under the assumption, that the concentration of excitons at

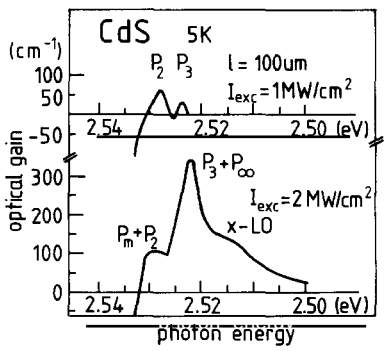

Fig. 25. Gain spectra of CdS under high N_2-laser excitation, obtained by the excitation strip-length method. The x–x scattering bands P_2, P_3 and P_∞, the acoustic phonon sideband of the bound exciton I_1 (P_m-band) and the x–LO process are seen (from Bohnert et al. [3.8]).

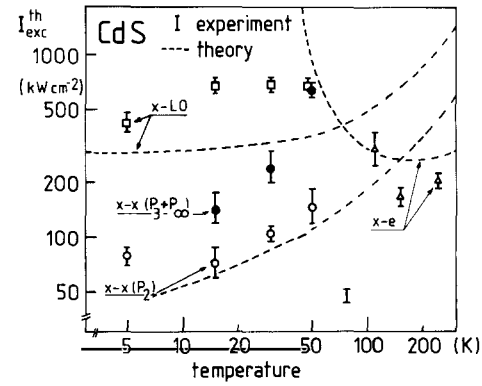

Fig. 26. Temperature dependence of the excitation intensity I^{th}_{exc} required to reach the laser threshold for different recombination processes in CdS. Error bars = experimental results, dashed lines = theory. The experimental point at 77 K is discussed in the text (from Koch et al. [4.10]).

threshold n_x^{th} is proportional to I_{exc}^{th}. The proportionality holds only as long as no strong stimulated emission takes place. In fact, the predictions of the theory compare favourable with the experiment: The threshold of the P_2-line increases with T because of the increase of the thermal population of the final state excitons and a corresponding reabsorption. The threshold for the x–e process first decreases with T, since the number of free carriers increases due to thermal ionization of donors or excitons, and increases again because of the reabsorption mechanism. The x–LO process shows up in stimulated emission only at the highest I_{exc} at lower temperatures. The fact, that the experimental values are higher than the theoretical curve, finds its explanation in a sublinear increase of n_x with I_{exc}, due to the partial saturation of the exciton density [4.10].

In view of the good overall agreement between experiment and theory, it seems noteworthy that the theory contains apart from the relation between I_{exc} and n_x only one partly unknown parameter, namely the effective loss constant of the resonator. The value used here is rather high ($K \simeq 10^3\,cm^{-1}$) since it incorporated radiationless processes not considered explicitly in the calculation.

The experimental point at 77 K deserves some attention, since it indicates a lower laser threshold than the points at adjacent temperatures. At this temperature, the three processes x–x (P_2), x–e and x–LO are spectrally almost degenerate, and it is assumed, that the cooperation of all three recombination processes causes the observed low threshold.

As a summary of this subsection it can be stated, that the existence of the intrinsic inelastic scattering process is well established, and that a quantitative understanding of these processes is reached in many respects.

Inelastic scattering processes involving impurity states are also discussed in the literature, e.g. the radiative recombination of an exciton bound to an impurity with simultaneous transfer of energy to either a free carrier, or a free exciton [4.25, 4.60–4.63] or to another carrier bound to the impurity [4.25, 4.64]. Some comments about these processes as well as about the stimulated recombination of bound excitons under emission of acoustic phonons [1.1, 4.42, 4.65, 4.66] are contained in subsection 4.5 of this paper.

4.3. Optical properties of biexcitons

The fact, that the biexciton is expected to occur as a bound state in semiconductors, has been already discussed in subsection 2.4. A first experimental finding concerning the radiative decay of biexcitons has been presented in fig. 16 for CuCl. In this subsection we describe further results concerning the optical properties of biexciton formation and decay. First we discuss the results for the Cu-halides, especially for CuCl which acts as a model-substance for biexcitons. Then we describe the experimental findings and their interpretations in the II–VI compounds.

4.3.1. Stationary and time resolved luminescence

As already mentioned in section 1, the biexcitons have been observed for the first time in 1968 in CuCl by the appearance of a luminescence band, which increases superlinearly with I_{exc} and which was interpreted as being due to the decay of a biexciton in a photon-like and an exciton-like polariton. Since then, this emission band has been investigated in much detail by various groups in France and Japan [e.g. 1.18–1.26, 3.14, 4.15, 4.67–4.121]. Theoretical investigations concerning different aspects of the biexciton problem are found e.g. in [1.18–1.28, 2.16–2.21, 4.11–4.20, 4.122–4.162]. The significant doublet structure of the biexciton emission band which is due to the decay of the biexcitons in photons and either transverse polaritons or longitudinal excitons has been already shown in fig. 16. The shape of

the spontaneous emission can qualitatively be understood solely from energy and momentum conservation. (For the quantitative lineshape calculation see subsection 4.1.) We assume for simplicity simple parabolic bands for the biexciton and the exciton. Then energy and momentum conservation in the decay process are given by

$$\left.\begin{aligned} &2(E_g(T)-E_x^b)-E_m^b+\frac{\hbar^2 k_i^2}{2m_m}=E_g(T)-E_x^b+\frac{\hbar^2 k_f^2}{2m_x}+\hbar\omega \\ &\text{with} \\ &m_m=2m_x \text{ and} \\ &k_i=k_f+k_f^{\text{photon}} \quad \text{and} \quad k_f^{\text{photon}}\simeq 0 \end{aligned}\right\} \tag{4.10}$$

it follows immediately, that $\hbar\omega$ is given by

$$\hbar\omega=E_g(T)-E_x^b-\frac{\hbar^2 k_i^2}{4m_x}-E_m^b. \tag{4.11}$$

If one assumes a Boltzmann distribution for the biexcitons, one expects from (4.11) an emission band, which resembles an inverted Boltzmann distribution and which extends from $E_x-E_m^b$ to lower photon energies. An analysis of the emission band allows in principle to determine E_m^b and the temperature of the biexciton gas.

A more realistic analysis has to take into account the superposition of the transitions to longitudinal excitons or transverse polaritons or in uniaxial crystals to mixed-mode polaritons [4.11–4.20]. Furthermore, the deviation of the polariton dispersion curve from a simple parabola and the influence of scattering processes have to be considered [e.g. 4.11, 4.12, 4.15]. The agreement between experiment and theory is very good [4.15, 4.80, 4.81].

In principle also the decay of a biexciton into a photon and an exciton in a state with a higher quantum number is possible, but it has a rather low transition probability [4.134] and is not observed in Cu-halides. The decay of biexcitons into one polariton on the lower and one on the upper polariton branch (the so-called two-photon decay) seems to have a rather high probability [4.162]. Because of k-conservation, only molecules around $k=0$ can participate in this process.

The investigation of the low-temperature luminescence of CuBr under high exitation also yielded indications for biexcitons [e.g. 4.71, 4.77]. However, the biexciton emission bands in CuBr have been investigated in less detail than in CuCl. The same is true for the zincblende II–VI compounds [4.36]. In the wurtzite II–VI compounds, there appears a so-called M-band under high excitation, which is also attributed to the biexciton decay [e.g. 4.11, 4.19, 4.20, 4.41, 4.51, 4.56, 4.66, 4.163–4.176]. Since many findings indicate the participation of impurity states [e.g. 1.1, 4.25, 4.42, 4.60–4.63, 4.65, 4.66, 4.177, 4.178], however, a unique assignment of the M-band in II–VI compounds is impossible (see also subsection 4.5). Therefore, the experimental proofs for the existence of biexcitons in II–VI compounds had to come from other spectroscopic methods, which are discussed together with the corresponding results for the Cu-halides in subsection 4.3.3.

Before continuing the discussion, some remarks about the time evolution of the M-band in CuCl should be made. The results cited so far were obtained under quasistationary conditions, i.e. the

duration of the excitation pulse τ_{exc} ($2\,\text{ns} \lesssim \tau_{exc} \lesssim 10\,\text{ns}$) was longer than the formation and decay times of the biexcitons. In order to determine these values, time resolved spectroscopy after pico-second pulse excitation has to be performed [3.9–3.12, 3.14, 4.82, 4.93, 4.102, 4.103, 4.109–4.111, 4.113]. Typical spectra demonstrating the evolution of the M-band luminescence in time are shown in fig. 27. The initially rather hot gas of biexcitons cools down to some 20 K within 200 ps [4.87].

The temporal behaviour of the integrated M-band luminescence is shown in fig. 28. It exhibits a significantly non-exponential decay, which can be described quantitatively by the following rate equations for the densities of excitons and biexcitons, n_x and n_m, respectively [3.9], as long as stimulation effects can be neglected:

$$\left.\begin{aligned} \mathrm{d}n_x/\mathrm{d}t &= QI_{exc}(t) - n_x/\tau_x - Bn_x^2 + n_m/\tau_m + Cn_m n_x \\ \mathrm{d}n_m/\mathrm{d}t &= \tfrac{1}{2}Bn_x - n_m/\tau_m - Cn_m n_x. \end{aligned}\right\} \tag{4.12}$$

$Q \cdot I_{exc}(t)$ is the generation rate for excitons, τ_x and τ_m are the lifetimes of excitons and molecules, respectively. B is the rate constant for the biexciton formation out of excitons and $Cn_m n_x$ finally describes the scattering rate between an exciton and a biexciton in which a photon and two excitons are created.

The parameters which have been obtained by fitting the solution of this coupled differential equations to the experiment are $\tau_m = 1\,\text{ns}$, $B = C = 1.8 \times 10^{-10}\,\text{cm}^3\,\text{s}^{-1}$, $\tau_x = 1\,\text{ns}$, $Q = 10^5\,\text{cm}^{-1}$. Similar values for τ_m have been obtained by other authors [e.g. 3.14, 3.82, 4.87]. However, calculations for the reaction-kinetics are always model-calculations which at most can show that an experimentally observed behaviour can be understood in the framework of this model, but normally there exist other models

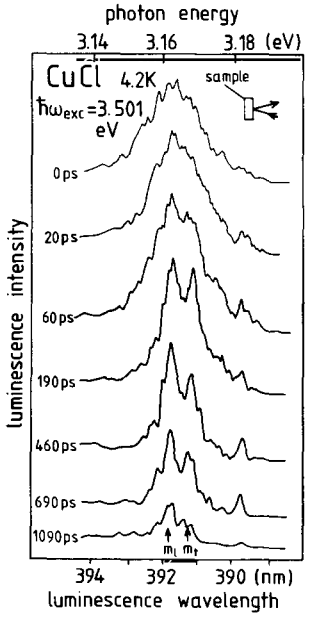

Fig. 27. The temporal evolution of the m_t and m_l-bands of CuCl after picosecond excitation. The decay time after the maximum of the excitation pulse is given on the left, the geometry of the experiment in the right top corner (from Ojima et al. [3.11]).

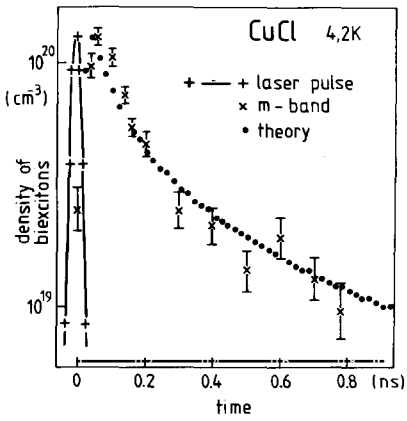

Fig. 28. Temporal behaviour of the integrated m_t and m_l-band intensity in CuCl after picosecond excitation (from Ostertag and Grun [3.9]).

which describe the experiment equally well, see e.g. ref. [3.14]. In this paper a more complicated set of differential equations than above has been used and the comparison between experiment and theory is again quite satisfactory.

4.3.2. Excitation spectroscopy

The analysis of the luminescence spectra of CuCl gave already rather conclusive evidence for the existence of biexcitons. Nevertheless, one tried to find further independent proofs for their existence and to develop methods which allow a precise determination of their symmetries and energies. Several of these methods make in different ways use of the fact, that a two-photon transition from the crystal-ground state to the biexciton level has a very high probability ("giant oscillator strength") [e.g. 4.123, 4.139, 4.179], which results in K_2-values which are several orders of magnitude larger than that for "normal" two-photon absorption, see table 4. If only photons of one frequency (i.e. from one laser beam) are used for the excitation, K_2 is given in second order perturbation by

$$K_2 = \text{const} \cdot \left| \sum_{\mathrm{x}} \frac{\langle \mathrm{m}|H_{\mathrm{D}}|\mathrm{x}\rangle\langle \mathrm{x}|H_{\mathrm{D}}|0\rangle}{E_{\mathrm{x}} - \hbar\omega_{\mathrm{exc}}} \right|^2 \delta(E_{\mathrm{m}} - E_0 + 2\hbar\omega_{\mathrm{exc}}), \tag{4.13}$$

where H_{D} is the dipole operator, and the summation runs over all virtually excited intermediate states $|\mathrm{x}\rangle$.

In (4.13) damping has been neglected. Formulas for K_2 including this effect are given e.g. in [4.180].

Firstly, K_2 is enlarged by the resonance dominator. The value of the denominator ΔE is given by

$$\Delta E = E_{\mathrm{x}}^{\mathrm{S}} - \hbar\omega_{\mathrm{exc}} = E_{\mathrm{x}}^{\mathrm{S}} - \tfrac{1}{2}E_{\mathrm{m}} \simeq \tfrac{1}{2}E_{\mathrm{m}}^{\mathrm{b}} \lesssim 14\,\mathrm{meV}, \tag{4.14}$$

where $E_{\mathrm{x}}^{\mathrm{S}}$ is the energy of the lowest dipole-allowed exciton (generally a singlet). In contrast to this almost resonant excitation of the intermediate state, ΔE is about 1 eV for normal two-photon band-to-band excitation. Thus K_2 is increased by the resonance effect roughly four orders of magnitude. A further increase is expected from the matrix elements themselves due to the large extension of the wave function of the virtually excited intermediate exciton state. There is, however, some discrepancy about the numerical value of the resulting additional factor. Theoretical predictions range from about 10 up to several orders of magnitude [4.123, 4.139, 4.179].

The influence of this large value of K_2 is displayed nicely in the excitation spectra of the biexcitons. Fig. 29 gives the excitation spectra of the $\mathrm{m_t}$- and $\mathrm{m_l}$-bands together with those of some other emission bands, discussed later on in the text. For $\hbar\omega_{\mathrm{exc}} \gtrsim E_{\mathrm{x}}$, the luminescence intensity I_{lum} is almost constant. The small dip around 3.205 eV is caused by the reflection maximum of the Γ_5-exciton. The biexcitons are formed under this condition from free excitons (process 1 in fig. 30). The biexciton binding energy, which has to be dissipated in the creation of the biexciton, is very close to the LO-phonon energies in CuCl and CuBr. Since the coupling of the LO-phonons is very effective in ionic compounds, the binding energy is predominantly emitted as a LO-phonon [4.83]. This energetic coincidence might explain, why the formation of biexcitons is favoured in CuCl and CuBr over the inelastic exciton–exciton collision. Since the dispersion curve of the LO-phonon is rather flat, biexcitons with rather large kinetic energies are formed, which thermalize among themselves by elastic collisions very rapidly [3.14], but which cannot reach completely the thermal equilibrium with the lattice during their lifetimes by the emission of acoustic phonons (AP) (process 2 in fig. 30) [3.14, 4.83].

The decay of the biexcitons gives rise to the $\mathrm{m_t}$- and $\mathrm{m_l}$-bands, shown as process 3. For $\hbar\omega_{\mathrm{exc}} < E_{\mathrm{x}}$,

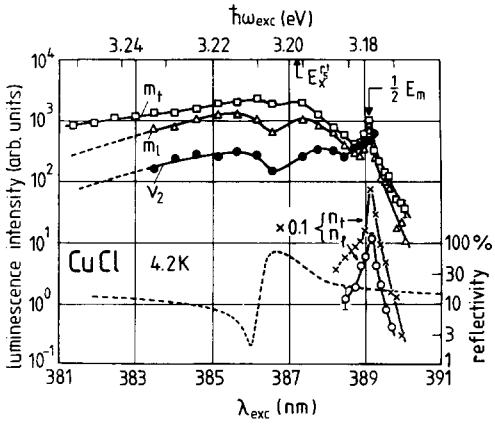

Fig. 29. Excitation spectra of the m_t(□) and m_l(△) bands of CuCl, of the narrow bands n_t(×) and n_l(○) and of the bound exciton line ν_2(●). One observes a dip at the transverse energy of the Γ_5-exciton due to the maximum of reflection (dashed line). The biexciton recombination bands m_t, m_l and n_t, n_l show a significant peak, if the photon energy of the exciting laser equals one half of the biexciton energy. The excitation spectrum of the ν_2-line shows no such resonance.

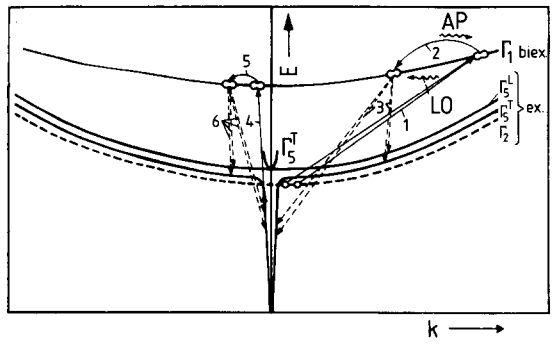

Fig. 30. A schematic representation of various formation-, relaxation and decay processes of biexcitons; 1: formation of a biexciton e.g. from two triplet excitons under emission of a LO-phonon; 2: partial thermalization of a biexciton with the lattice by emission of acoustic phonons (AP); 3: decay of a biexciton in a photon and either a transverse or a longitudinal exciton, giving rise to the m_t and m_l bands, respectively; 4: creation of a biexciton by two photon absorption; 5: partial thermalization of a "cold" biexciton with the lattice by absorption of acoustic phonons; 6: recombination of a biexciton giving rise to the narrow emission bands n_t and n_l, respectively (from Levy et al. [4.83]).

the excitation spectrum starts to decrease. At $\hbar\omega_{exc} = \frac{1}{2}E_m$, a significant peak appears in the excitation spectrum. Furthermore, two narrow emission lines n_t and n_l show up at the high energy edges of m_t and m_l, respectively, as seen in fig. 31 [4.83–4.85, 4.96–4.98, 4.108]. At intermediate excitation intensities, they are the only emission bands which are detected in this region. The appearance of n_t and n_l as well as the resonance in the excitation spectrum is easily explained by assuming that a larger number of

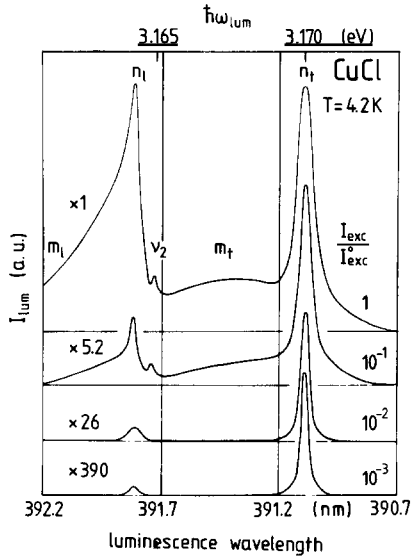

Fig. 31. Emission spectra of CuCl under resonant biexciton-excitation, showing broad (m_t and m_l) and narrow (n_t and n_l) emission bands and the bound exciton recombination line ν_2. $I^0_{exc} \approx 3\,MW/cm^2$, $\hbar\omega_{exc} = \frac{1}{2}E_m = 3.186\,eV$ (from Levy et al. [4.83]).

biexcitons is created by resonant TPE (process 4). Since the kinetic energy corresponding to $k_m = 2k_{exc}$ is small compared to the thermal energy $k_B T_l$ they start to thermalize with the lattice by absorbing acoustic phonons and by thus spreading in k-space (process 5). Because of their finite lifetime, this thermalization is again not perfect, and the recombination of these "cold" biexcitons gives rise to the narrow emission bands n_t and n_l (process 6). The excitons left behind in this process may then form "hot" biexcitons according to process 1, which give rise to the m_t- and m_l-bands at higher I_{exc}, together with those originally cold biexcitons, which have undergone scattering processes with high energy excitons or biexcitons. The interpretation of the narrow lines as cold biexciton recombination lines is also supported by polarization measurements [4.101]. Thus, these narrow lines cannot be assigned to a Bose–Einstein condensation of excitonic molecules. This conclusion has also been reached in [4.97, 4.111, 4.120]. In a recent paper by Chase et al. [4.117], narrow molecule recombination lines are observed above a critical excitation intensity, which show different characteristics than the lines observed in ref. [4.83]. The question, whether these recent observations of Chase et al. can yield evidence for a Bose–Einstein condensation is still subject to a controversal discussion [e.g. 4.120].

The appearance of narrow emission bands has been also reported for CuBr [4.80, 4.181, 4.182]. However, they are not so intensively studied as in CuCl.

Resonances in the excitation spectra of the M-bands in CdS and ZnO, which are reported by some authors [4.66, 4.183], can be regarded as hints for the existence of biexcitons in these materials. Unfortunately, this interpretation is not unequivocal, since at the same spectral positions there are resonances in the excitation spectra of bound excitons, which are interpreted as excited states of these impurity complexes [4.184–4.186].

The excitation spectrum of the M-band in red HgI_2 gave also some indication for the existence of biexcitons in this compound. For a detailed discussion see [4.38] and the literature cited therein.

4.3.3. Some other results of nonlinear spectroscopy

In this subsection we are dealing with the experimental results of some other nonlinear spectroscopic methods and the conclusions which may be drawn from these results concerning biexcitons. The methods discussed here are two-photon absorption and two-step absorption, including virtually or really excited intermediate states, respectively, and the two-photon (or hyper-) Raman scattering via virtually excited biexcitons. Again, we are describing the methods and the results relevant to the Cu-halides first. Then the findings for the II–VI semiconductors are discussed.

In the two-photon absorption, the "giant oscillator strength" for biexciton creation is more directly exploited, than in the case of the excitation spectroscopy. A two beam method is used (see subsection 3.2), in which the crystal is illuminated by an intense, spectrally narrow, tunable dye-laser beam $\hbar\omega_{exc}$ (with $\hbar\omega_{exc} < \frac{1}{2}E_m$) and a second, broad dye-laser. A two photon transition process manifests itself in a dip in the transmission spectrum of the broad dye laser, which depends on $\hbar\omega_{exc}$ in the following way:

$$\hbar\omega_{exc} + \hbar\omega_{dip} = E_m. \tag{4.15}$$

The method has been applied successfully to CuCl [4.84, 4.94, 4.102] and CuBr [4.102, 4.114]. By varying the polarizations of the two beams it is possible, to determine the symmetry of the biexciton level [e.g. 4.94, 4.114]. The symmetries of the biexciton states are given by the reduction of the direct product of the irreducible representations of the two valence band holes, the two conduction band electrons and the envelope function, where care has to be taken that the whole wave function is antisymmetric with respect to the exchange of two equal particles [e.g. 4.149],

$$\left[\left(\sum_i (\alpha_i \Gamma_i^{\mathrm{v}}) \otimes \left(\sum_i \alpha_i \Gamma_i^{\mathrm{v}}\right) \otimes (\Gamma^{\mathrm{c}} \otimes \Gamma^{\mathrm{c}}) \otimes \Gamma^{\mathrm{env}}\right]_- = \sum_j \gamma_j \Gamma_j^{\mathrm{m}}, \right. \tag{4.16}$$

where the summations over i run over the different valence bands. Since a simple guess of the rotation levels of a biexciton, using an effective mass picture, yields values for $\hbar^2\theta^{-1}$ (θ is the moment of inertia) which are much larger than the biexciton binding energy, the discussion may be restricted to a symmetric Γ_1 envelope function and to antisymmetric products of conduction- and valence band functions, respectively. Equation (4.16) then reduces to

$$\left[\left(\sum \alpha_i \Gamma_i^{\mathrm{v}}\right) \otimes \left(\sum \alpha_i \Gamma_i^{\mathrm{v}}\right)\right]_- \otimes [\Gamma^{\mathrm{c}} \otimes \Gamma^{\mathrm{c}}]_- \otimes \Gamma_1^{\mathrm{env}} = \sum_j \gamma_j \Gamma_j^{\mathrm{m}}. \tag{4.17}$$

In the Cu-halides, the splitting of the Γ_7 and Γ_8 valence band is large compared to $E_{\mathrm{m}}^{\mathrm{b}}$. Therefore, only the upper valence band participates in the formation of the bound biexciton states. Eq. (4.17) consequently reads [4.126, 127]:

$$\left.\begin{aligned} &[\Gamma_7 \otimes \Gamma_7]_- \otimes [\Gamma_6 \otimes \Gamma_6]_- \otimes \Gamma_1^{\mathrm{env}} = \Gamma_1 \qquad \text{for CuCl} \\ &[\Gamma_8 \otimes \Gamma_8]_- \otimes [\Gamma_6 \otimes \Gamma_6]_- \otimes \Gamma_1 = \Gamma_1 + \Gamma_3 + \Gamma_5 \quad \text{for CuBr and} \end{aligned}\right\} \tag{4.18}$$

for most of the other semiconductors with T_d symmetry.

The corresponding energy levels have been observed in CuCl [4.84, 4.94, 4.102] and CuBr [4.86, 4.102, 4.114] by TPA. The numerical values are: $\Gamma_1^{\mathrm{CuCl}} = 6.3720\,\mathrm{eV}$; $\Gamma_1^{\mathrm{CuBr}} = 5.9061\,\mathrm{eV}$; $\Gamma_5^{\mathrm{CuBr}} = 5.9103\,\mathrm{eV}$ and $\Gamma_3^{\mathrm{CuBr}} = 5.9128\,\mathrm{eV}$ [4.114], respectively. The TPA coefficient K_2 is about 3×10^{-3} cm/W in CuCl [4.94] and is thus considerably larger than for nonresonant TPA-processes (see table 4) in accordance with theoretical predictions.

The two-step process, which has also a high transition probability [4.126, 4.139, 4.179], involves real excitons in the intermediate state instead of virtually excited ones, which means that $\hbar\omega_{\mathrm{exc}}$ has to fulfill the inequality $\hbar\omega_{\mathrm{exc}} \gtrsim E_{\mathrm{x}}$. Photons from the broad probe beam are now absorbed by transforming a real exciton in a real biexciton, i.e. by the reverse of process 3 in fig. 30. The corresponding dip in the probe beam now does not shift as a function of $\hbar\omega_{\mathrm{exc}}$. The analysis of its shape allows to determine the distribution of the excitons on their dispersion curve. This has been done for "steady state" excitation with ns pulses [4.92, 4.102], and time-resolved under ps excitation [3.14, 4.113]. It turns out, that the temperatures of the biexciton gas (determined from the analysis of the $m_{t/l}$-band luminescence) and of the exciton gas (determined from the analysis of the absorption profile) are equal [4.92, 4.112]. The ps-experiments revealed a thermalization time of the excitons to temperatures around 40 K of the order of 300 ps [3.14].

In the two-photon Raman scattering process (TPRS), the biexciton is created only virtually by two polaritons in contrast to the processes discussed so far. This virtually excited biexciton decays in the case of a backward scattering configuration in either a longitudinal exciton or an exciton-like transverse polariton and a photon-like polariton (fig. 32). Momentum is conserved throughout in this process. The corresponding emission lines are called r_l and r_t, respectively. They are Raman-like, i.e. they shift with the frequency of the excited laser according to

$$\hbar\omega_{t/l} = 2\hbar\omega_{\mathrm{exc}} - E_{\mathrm{x}_{t/l}}. \tag{4.19}$$

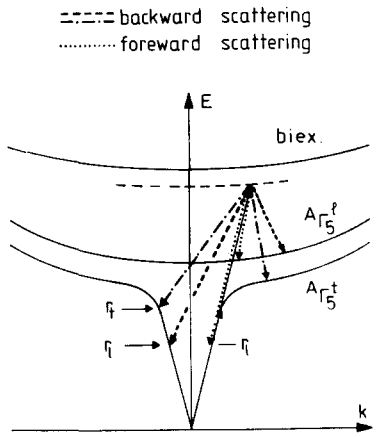

Fig. 32. A schematic representation of two-photon-Raman scattering via virtually excited biexcitons. Forward and backward scattering processes are shown. Solid arrows: virtual excitation of the biexciton; dashed and dashed-dotted arrows: backward scattering yielding the r_t and r_l emission, respectively; dotted arrows: forward scattering yielding the r_l emission.

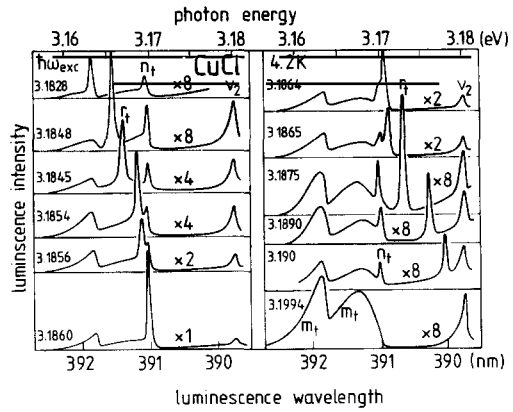

Fig. 33. Emission spectra of CuCl showing the two-photon-Raman scattering line r_t in exact backward scattering. The line r_l is forbidden in this configuration. Furthermore, the biexciton recombination bands m_t, m_l and n_t and the bound exciton recombination line ν_2 are observed (from Vu Duy Phach et al. [4.100]).

This two-photon (or hyper-) Raman scattering can be interpreted as an inelastic polariton–polariton scattering. Due to the almost resonant excitation of the different quasiparticles, this third order process can be observed rather easily [4.84, 4.100, 4.108, 4.116] at intermediate I_{exc} and low temperatures, provided good samples are used together with a narrow band dye-laser, the spectral halfwidth of which should lie below 0.2 meV [4.108].

Fig. 33 gives a series of emission spectra of CuCl which show the radiative recombination of a bound exciton (ν_2) and the luminescence bands m_t, m_l and n_t, which are connected with the radiative decay of biexcitons, see subsection 4.3. In addition a Raman-like emission (r_t) is observed. The relation between $\hbar\omega_{exc}$ and $\hbar\omega_{r_t}$ fulfills eq. (4.19) with high precision. This is demonstrated in fig. 34 where a slope-two

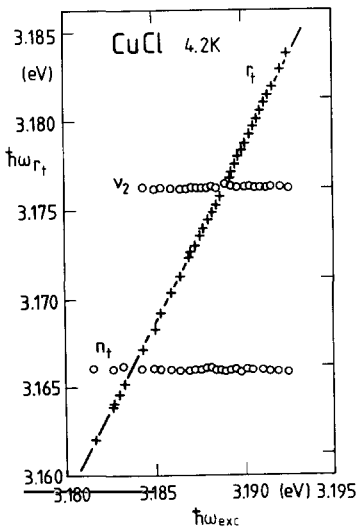

Fig. 34. The dependence on $\hbar\omega_{exc}$ of the energy of the Raman-line r_t, the narrow line n_t and the bound exciton emission line ν_2 in CuCl in backward scattering (from Vu Duy Phach et al. [4.100]).

line is fitted to the experimental points. For comparison the spectral positions of ν_2 and n_t are indicated. They show no dependence on $\hbar\omega_{exc}$.

The influence of the biexciton levels is displayed in an increase of the intensities of the Raman lines $I_{r/t}$, if $2\hbar\omega_{exc}$ approaches E_m. Fig. 35 gives an example for CuCl. The intensity of the Raman line is plotted together with that of the narrow line n_t, which is created by the tail of the exciting laser [4.100]. At resonant excitation, the r_t lines cannot be distinguished from the n_t lines in a backward scattering experiment, if ns excitation pulses are used. Consequently, only the sum of I_{n_t} and I_{r_t} can be given at resonance, see fig. 35. In the case of forward scattering configuration, the Raman lines and the narrow lines are situated at different spectral positions (see 4.4) even at resonance, and may therefore be distinguished. The excitation spectrum of the Raman lines gives then also an increase of I_r with decreasing $2\hbar\omega_{exc} - E_m$, however with a dip at the resonance [4.100]. A dip caused by the damping of the intermediate excitation state in the case of resonant excitation has also been found in the excitation spectra of higher harmonic creation experiments [4.104, 4.118].

With picosecond pulses, it was possible to separate the n and r lines under resonant excitation by their different time behaviour. While the temporal variation of the coherent Raman-lines reproduces the excitation pulse, the n-lines show an appreciably slower decay [4.109, 4.110]. For a further discussion of the relation of TPRS and luminescence in the case of resonant excitation see e.g. [1.19, 1.22, 4.120, 4.121, 4.218].

Furthermore, time-resolved luminescence and transmission measurements allow to study the time evolution of the population of biexcitons and excitons in CuCl [4.112, 4.113]. One of the results is that the exciton and biexiton gases are always at the same temperature T_x. T_x decreases from about 40 ± 10 K immediately after the picosecond excitation pulse to values of about 20 K after 1.4 ns [4.112].

Finally it should be pointed out that the narrow resonances in the excitation spectra of the Raman-lines may disappear at rather high excitation intensities, where the Raman-lines are strongly stimulated. Instead, rather broad excitation spectra are observed, partly exhibiting peaks which are not connected with biexciton levels [4.187, 4.213]. This makes the determination of the biexciton energies from the TPRS resonance less reliable than TPA-measurements.

Concerning the wurtzite II–VI compounds, there are also several indications for the possible existence of biexcitons from nonlinear spectroscopy.

An induced absorption band in CdS around 2.545 eV has been interpreted as being due to the two-step transition from excitons to biexcitons [4.171, 4.188–4.190]. Hvam reports gain and induced absorption in this spectral region, which he explained by the recombination of biexcitons and the transition from excitons to biexcitons, respectively [4.39]. However, some rather improbable assump-

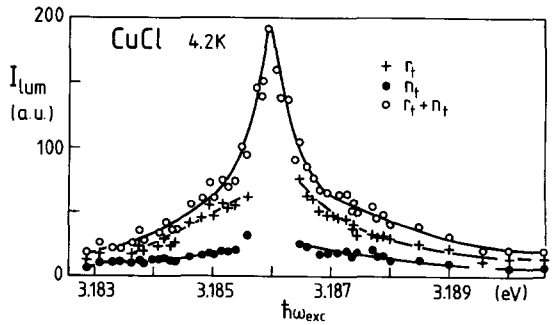

Fig. 35. The intensities of the two-photon-Raman line r_t, of the narrow luminescence line n_t and of their sum as a function of $\hbar\omega_{exc}$ in CuCl for a backward scattering geometry. $I_{exc} \simeq 1.8$ MW/cm^2, the resonance occurs at $\hbar\omega_{exc} = \frac{1}{2}E_m = 3.186$ eV (from Vu Duy Phach et al. [4.100]).

tions had to be made for a quantitative interpretation of the results: In CdS, the temperatures of the exciton and the biexciton gas differed by a factor four [4.39]. This is rather unlikely for two penetrating and strongly interacting gases and is in contradiction to the experimental results in CuCl. In ZnO, a decrease of the density of biexcitons with increasing excitation had to be postulated [4.39]. Some nonlinear absorption signals observed with a narrow, tunable dye-laser [4.191, 4.215], are lacking the final evidence for the simultaneous participation of two-photons: a two step process, where the first photon creates an impurity center (e.g. by ionizing an electron from a donor) and the second photon excites a bound exciton at this new center [4.216] would yield nonlinear absorption signals similar to the findings of refs. [4.191] and [4.215]. Furthermore, transitions to excited states of bound excitons occur within experimental error in the same spectral region [4.184–4.186]. The definite experimental proof for the existence of biexcitons in CdS and ZnO came from the resonance in TPRS via virtually excited biexcitons [4.66, 4.191–4.193] and from TPA spectroscopy [4.66, 4.194, 4.195].

In the latter case, a slightly modified method has been used in so far, as the sample was excited by a narrow tunable dye-laser only, and instead of the broad band probe beam the luminescence of the excited sample itself was used. Consequently, a two-photon absorption process was detected in this luminescence assisted two-photon spectroscopy (LATS) as a reabsorption dip which shifts over the luminescence band and which fulfills again the equation:

$$\hbar\omega_{\mathrm{exc}} + \hbar\omega_{\mathrm{dip}} = E_{\mathrm{const}}. \tag{4.20}$$

Fig. 36 gives an example for the spectra and for equation (4.20), the constant being 5.0983 eV.

This two-photon absorption is attributed to the formation of a biexciton for the following reasons: The level is 5.7 meV below two times the energy of the Γ_6 triplet exciton ($E_x = 2.552$ eV), a value which is reasonable for the biexciton binding energy (see subsections 2.4 and 4.3.4). The polarization properties are compatible with Γ_1 symmetry, which is expected for the biexciton ground state. Finally, the value of 5.0983 eV coincides reasonably with a resonance in TPRS [4.191, 4.192] observed at 2.5507 eV*, which indicates, that only nonlocalized quasiparticles participate in the process.

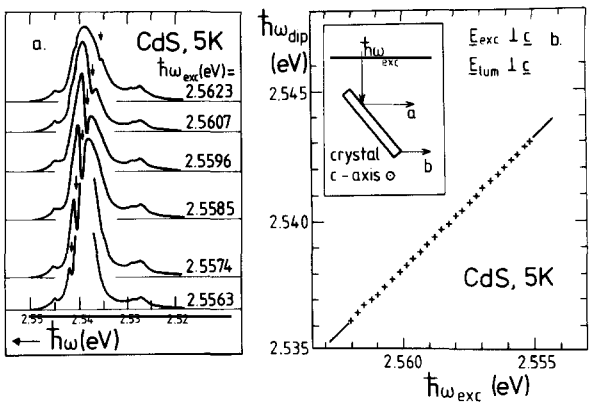

Fig. 36. Emission spectra of the M-band of CdS for different values of $\hbar\omega_{\mathrm{exc}}$, showing a dip (indicated by an arrow) (a) which shifts with $\hbar\omega_{\mathrm{exc}}$. In (b) the relation between $\hbar\omega_{\mathrm{exc}}$ and $\hbar\omega_{\mathrm{dip}}$ is given. The crosses are experimental points, the solid line corresponds to $\hbar\omega_{\mathrm{dip}} + \hbar\omega_{\mathrm{exc}} = 5.0983$ eV (from Schrey et al. [4.194]).

* It should be pointed out, that there is some confusion in the literature concerning the calculation of photon energies from wavelength. Several authors use the vacuum speed of light, though wavelength-tables for standard spectral lines generally give values in air under spectroscopic normal conditions.

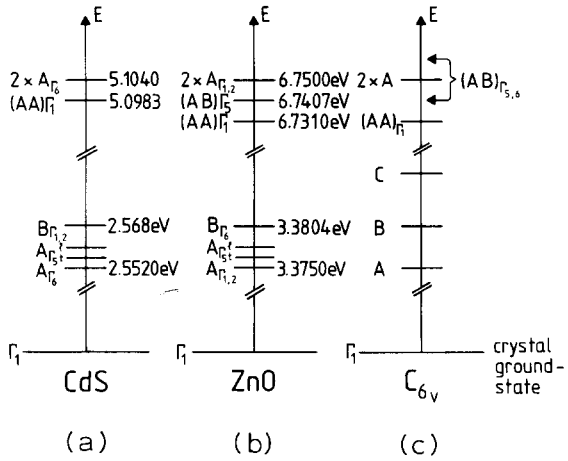

Fig. 37. Energies of excitons and biexcitons in CdS, ZnO and a general wurtzite-type II–VI semiconductor. A_{Γ_i} and B_{Γ_i} ($i = 1, 2, 5, 6$) are the symbols for the different A- and B-excitons (see subsection 2.3). $(AA)_{\Gamma_j}$ and $(AB)_{\Gamma_j}$ ($j = 1, 5, 6$) stands for a biexciton consisting of two electrons and either two holes from the A-valence band or of one hole from the A- and from the B-valence band, respectively.

Apart from the Γ_1 level, no further biexciton level has been detected in CdS so far (see fig. 37a), in contrast to ZnO. In the latter material a distinct resonance in TPRS has been observed at $\hbar\omega_{exc} = 3.3655\,eV \pm 0.5\,meV$ [4.66, 4.193] which occurred at this spectral position in different samples and under different I_{exc}. Since furthermore the polarization properties are compatible with Γ_1 symmetry, the state at $6.731\,eV \pm 1\,meV$ is believed to be the biexciton ground state. The resulting binding energy of $19 \pm 1\,meV$ is rather large as compared to theoretical predictions. This point will be discussed in more detail in subsection 4.3.4.

An excited biexciton state at 6.7407 eV with symmetry Γ_5 has been detected in ZnO by LATS [4.66, 4.194, 4.195]. So we are led to the level scheme shown in fig. 37b. An alternative assignment has been suggested by Hvam [4.195]. He attributes the level observed by LATS to the biexciton ground state, which reduces the value of E_m^b by approximately a factor two. On the other hand, this interpretation brings about some difficulties: There is no satisfactory explanation for the sharp resonance in TPRS. In addition problems arise concerning the Γ_5 symmetry of the level ascribed by [4.195] to the biexciton ground state. Finally it becomes necessary to explain the M-luminescence band of ZnO, which is ascribed to biexciton decay by [4.195], mainly by a decay of the biexciton ground state in a photon and either a longitudinal B_{Γ_5}-exciton or a polariton on the upper branch of this B-exciton. Though this process is dipole-allowed (starting from a Γ_1 biexciton level) it involves a spin flip and has therefore a rather low transition probability as compared to the dipole- and spinflip allowed transition to the A_{Γ_5}-exciton levels. However, it is assumed in [4.195] that this second process contributes only to a small amount to the luminescence at the high energy edge of the M-band. A nonlinear absorption signal at $3.365\,eV \pm 1\,meV$ called IA in [4.195] is attributed to the two-step transition from excitons, which are excited really by the high energy tail of the dye-laser, to the biexciton level. On the other hand, this experimental result is also consistent with a two-photon transition from the crystal ground state to the biexciton level of fig. 37b.

Since this Γ_1 level could unfortunately not be detected by LATS, because of a competitive strong one-photon absorption of the exciting light, the final decision between the two models must come from two-photon spectroscopy which has been shown to work successfully in the Cu-halides. Until these experiments are performed, we use for the further discussion in ZnO the level scheme of fig. 37b.

The next part of this subsection is devoted to answer the question, why an excited biexciton level is observed in ZnO and not in CdS, though the two materials are very similar.

Assuming again, that only biexcitons with Γ_1 envelope are bound, then eq. (4.16) reads, if all three valence bands of the wurzite II–VI compounds are considered [4.149]

$$[(2\Gamma_7+\Gamma_9)\otimes(2\Gamma_7+\Gamma_9)]_-\otimes[\Gamma_7\otimes\Gamma_7]_-\otimes\Gamma_1^{\mathrm{env}}=4\Gamma_1+\Gamma_2+3\Gamma_5+2\Gamma_6. \tag{4.21}$$

It should be noted, that only one Γ_1 level results from the combination of two holes from the upper (A-) valence band in CdS and ZnO which then forms the lowest biexciton level $(AA)\Gamma_1$. The next higher levels involve already holes from the next (B-) valence band namely $(AB)\Gamma_5$ and $(AB)_{\Gamma_6}$ [4.149]. Since the A, B and C-valence bands are nicely reproduced in the A, B and C-exciton series, one could hope to observe these series also for the biexciton levels (see fig. 37c). Since the splitting of the A- and B-excitons amounts 16 meV in CdS [4.196] and is thus large in comparison to E_m^b, the $(AB)\Gamma_{5,6}$ biexciton levels are expected to be unbound. Their observation will be rather difficult. In ZnO the opposite is true, i.e. the splitting of the A- and B-excitons is only 5.4 meV [2.8] while $E_m^b = 19$ meV. Therefore, the excited Γ_5 biexciton level at 6.7407 eV is interpreted as the $(AB)\Gamma_5$-state.

As a concluding remark of this subsection it should be noted, that there is also some experimental evidence for the existence of biexcitons in II–VI compounds with T_d symmetry. In ZnSe a narrow resonance in TPRS has been observed [4.197] indicating a value of E_m^b of 2.2 meV, which is consistent with corresponding values deduced from the M-band luminescence [4.36]. For ZnTe see also [4.36]. Because of the small values of E_m^b it will be difficult, however, to observe in these materials the splitting of the biexciton ground state in a $\Gamma_1+\Gamma_5+\Gamma_3$ level as in CuBr.

In most of the direct III–V compounds, the values of E_m^b are expected to be below 0.5 meV. Therefore, the experimental observation of biexcitons will be extremely difficult. No results are reported so far.

4.3.4. A discussion of biexciton binding energy

In table 5 we have listed several parameters relevant for the description of biexcitons in direct gap semiconductors. Column 4 gives the exciton binding energy E_x^b, which is the energetic difference between the lowest free exciton (column 3) and the polaron gap, i.e. the gap renormalized by the carrier–phonon interaction. Column 7 gives the ratio of the experimentally determined values of E_m^b and E_x^b. This value is generally compared with the theoretical values for E_m^b/E_x^R, i.e. with the ration of E_m^b and the exciton Rydberg E_x^R. However, both expressions are in principle incommensurable quantities. E_x^b corresponds to E_x^R only in the case, that the exciton Bohr radius is large compared to the polaron radii of electrons and holes so that the band renormalization can completely develop for both carriers in the exciton (see e.g. [4.198] and the literature cited therein). In the opposite limit, the electron–hole pair in the exciton sees the unrenormalized gap and the Rydberg energy E_x^R for the 1s-exciton level is the whole energetic distance between E_x and the unrenormalized gap. The more or less ionic bound semiconductors discussed here, occupy an intermediate position, i.e. the exciton and polaron radii are of comparable size. This means, that the values of E_x^R for the 1s-exciton level are partly considerably larger than E_x^b. This effect is especially important for ZnO. Corresponding values for E_x^b and E_x^R taken from the literature are given in columns 4 and 8, respectively. In columns 11 and 12 we give calculated ratios E_m^b/E_x^R from different authors. In fig. 38 we compare these values (solid lines) with the experimental values of column 7 (open symbols) and column 9 (full symbols) from table 5. Whereas most of the values of E_m^b/E_x^R are within ±50% of the curve of [2.18] and above the results of

Table 5
Exciton and biexciton parameters of some direct gap materials

1	2	3	4	5	6	7	8	9	10	11	12
Material	Point-group	E_x [eV] exper.	E_x^b [meV] exper.	E_m [eV] exper.	E_m^b [meV] exper.	$\frac{(E_m^b)^{exp.}}{(E_x^b)_{exp.}}$	E_x^R [meV] theory	$\frac{(E_m^b)^{exp.}}{(E_x^R)_{theor.}}$	$\sigma = \frac{m_e^*}{m_h}$	$\frac{(E_m^b)^{theor.}}{(E_x^R)_{theor.}}$ [2.16, 2.17]	$\frac{(E_m^b)^{theor.}}{(E_x^b)_{theor.}}$ [2.18]
CuCl	T_d	Γ_2 3.200	190	Γ_1 6.3720	28	0.147	≃210	0.133	0.25	0.06	0.16
CuBr	T_d	$\Gamma_{3,4}$ 2.9633	108	Γ_1 5.9061 Γ_5 5.9103 Γ_3 5.9128	20.5	0.190	≃150	0.137	0.2	0.07	0.18
CdS	C_{6v}	Γ_6 2.552	28	Γ_1 5.0983	5.7	0.204	74**	0.077	0.14	0.08	0.2
ZnO	C_{6v}	Γ_1 3.3750	60.8	Γ_1 6.7310 Γ_5 6.7407	19	0.313	158**	0.120	0.47	0.034	0.13
ZnSe	T_d	$\Gamma_{3,4}$ $^{2.8025}_{\pm 0.0005}$	21 ± 1	Γ_1 5.6018	2.2	0.105	33**	0.067	0.23	0.06	0.17
ZnTe	T_d	$\Gamma_{3,4}$ 2.381	11 ± 1	Γ_1 4.7605	1.5 ± 1	0.136	23.5**	0.064	0.16	0.07	0.19

* Polaron masses.
** From G. Beni and T.M. Rice [5.20].

the variational calculations [2.16, 2.17], the value of ZnO deviates considerably from theory. This was partly used in the literature as an argument against the assignment of the biexciton levels according to fig. 36b [4.195]. If we compare the correct values of E_m^b/E_x^R from column 9 of table 5 with the calculation, all points including ZnO are nicely situated between the theoretical curves, thus indicating reasonable agreement between experiment and theory.

As a conclusion of the above discussion, it can be stated, that the precise calculation of E_m^b should start from the unrenormalized gap. Then the lowering of the energy due to the Coulomb-interaction and due to the partly quenched carrier–phonon coupling should be calculated for both excitons and biexcitons. The energetic difference between the biexciton level and two times the exciton level should

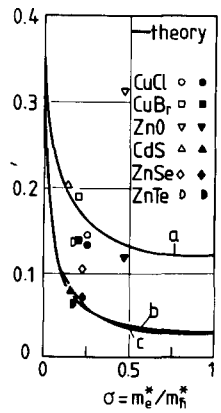

Fig. 38. A comparison of the calculated ratio E_m^b/E_x^R (solid lines) with $(E_m^b)_{experiment}/(E_x^b)_{experiment}$ (open symbols) and $(E_m^b)_{experiment}/(E_x^R)_{theory}$ (full symbols) for various semiconductors. Theories (a) from [2.18], (b) from [2.17] and (c) from [2.16]. (From Klingshirn [Habilitation-thesis].)

finally be compared to the experimental values of E_m^b. This calculation is by far not trivial and to our knowledge has not yet been carried out for biexcitons.

4.4. *Spectroscopy in momentum space via virtually excited biexcitons*

Until now, the two-photon Raman scattering (TPRS) via virtually excited biexcitons has been discussed only with respect to the determination of the properties of biexcitons (such as symmetry and energy levels). Since the exciton energy enters in the formulae for the spectral position of the Raman lines (4.19), TPRS allows to determine these quantities. As can be seen from fig. 32, the final state particles left in the crystal are already on the rather flat part of the polariton dispersion curve in the case of backward scattering, which leads to the typical slope two variation of the spectral positions of the Raman lines r_t and r_l with $\hbar\omega_{exc}$ (fig. 34). The situation is similar concerning the transition to the longitudinal exciton in the case of forward scattering (fig. 32). Taking into account the frequency dependent refractive index, the energy difference of $\hbar\omega_l$ in forward and backward scattering allows to determine the curvature of the dispersion curve of the longitudinal exciton and thus its effective mass. The value deduced e.g. for CuCl is $m_x = (2.5 \pm 0.5)m_0$ [4.99] in agreement with results obtained from inelastic exciton–electron scattering [4.8].

A different situation arises in a forward scattering configuration if both final state particles are on the lower polariton branch. In exact forward scattering, energy and momentum conservation demand $\hbar\omega_{exc} = \hbar\omega_r$, i.e. the Raman lines cannot be separated spectrally from the incident laser. If the angle between the k-vectors of the two final state particles is finite, their frequencies shift away from $\hbar\omega_{exc}$ (see fig. 39). Since they are both situated in the bottle-neck region, they are both observed as Raman-photons in the experiment. They are generally called r_t^+ and r_t^- because they are energetically situated above and below $\hbar\omega_{exc}$ [4.95, 4.98–4.100, 4.105, 4.107]. The variation of $\hbar\omega_{r_{t\pm}}$ with $\hbar\omega_{exc}$ deviates strongly from a slope two law as can be seen in fig. 40, for different external angles γ. (γ is defined in the inset of fig. 43.) Furthermore, transitions with one polariton on the upper polariton branch are possible [4.107], which are not shown in fig. 39. In [4.99], a self-consistent method has been developed to determine the polariton dispersion curve from experimental results as those shown in figs. 34 and 40.

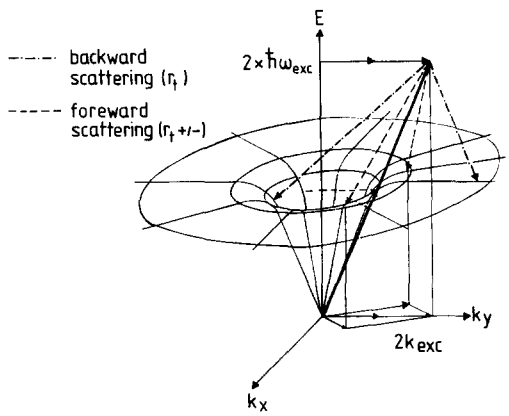

Fig. 39. A schematic representation of two-photon-Raman scattering for backward (dashed-dotted lines) and forward scattering (dashed lines), respectively. Only processes involving polaritons on the lower polariton branch are shown. In backward scattering, one polariton is exciton-like, the other photon-like giving rise to the r_t line. In foward scattering both polaritons are partly photon-like giving rise to the r_t+ and r_t− lines, which are situated above and below $\hbar\omega_{exc}$, respectively (from Hönerlage et al. [4.99]).

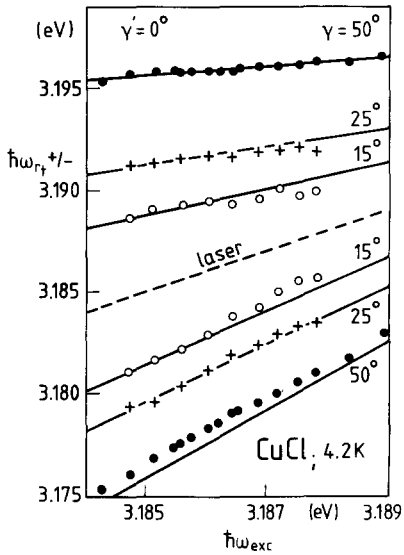

Fig. 40. The dependence of the Raman lines $\hbar\omega_{\Gamma_1+/-}$ on $\hbar\omega_{exc}$ in CuCl for different scattering geometries. For the definition of the scattering angles γ and γ' see fig. 9c. ○, ● and + are experimental points, the solid lines are calculated curves (from Vu Duy Phach et al. [4.94]).

Fig. 41 shows the results for the rather simple case of CuCl, which can be described by the Hopfield model [4.199, 4.200]. The agreement between experiment and theory is excellent. The open circles give the results of a "classical" two-photon absorption measurement of Fröhlich et al. [4.201]. In CuBr the situation is more complicated because of the higher degeneracy of the valence band, the participation of light and heavy holes, and possible k-linear and warping terms (see 2.3). Fig. 42 illustrates this situation. Again excellent agreement is found between experiment and theory. The parameters used are given in the captions of figs. 41 and 42, respectively.

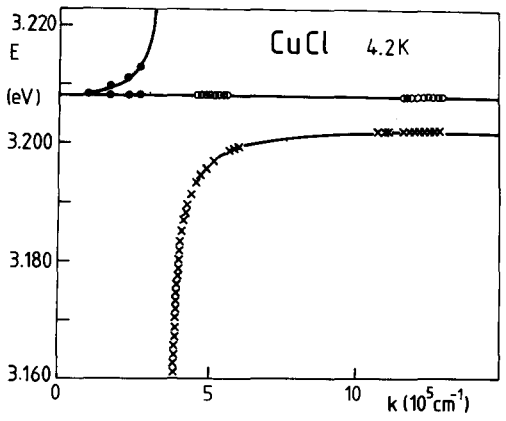

Fig. 41. The dispersion curve of the excitonic polariton in CuCl as deduced from two-photon-Raman scattering (○, ×). The parameters are: $m_x = (2.5 \pm 0.3)m_0$; $E_{x_1}^{\Gamma_5} = 3.2080$ eV; $E_{x_t}^{\Gamma_5} = 3.2025$ eV and $\varepsilon_b = 5.0 \pm 0.2$ (from Hönerlage et al. [4.99]). (●) from two-photon absorption (from Fröhlich et al. [4.201]).

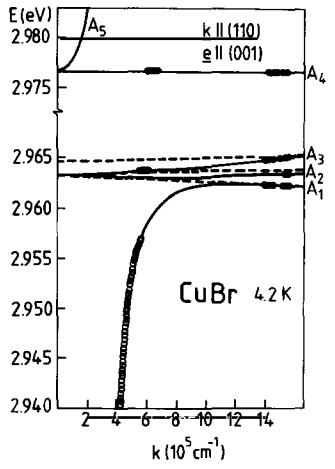

Fig. 42. The dispersion curves of excitons and polaritons in CuBr as deduced from two-photon-Raman scattering. The parameters are $E_x^{\Gamma_3} = E_x^{\Gamma_4} = 2.9633$ eV; $E_{x_t}^{\Gamma_5} = 2.9646$ eV; $E_x^{\Gamma_5} = 2.9766$ eV; $\varepsilon_b = 5.4 \pm 0.2$; $m_x = (11 \pm 3)m_0$; $c_k = (69 \pm 4)\ 10^{-11}$ eV cm (from Bivas et al. [4.115]).

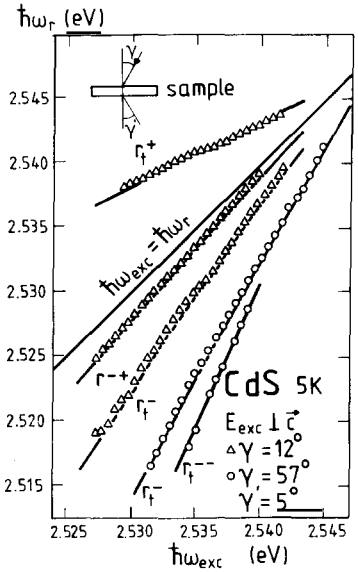

Fig. 43. The dependence of the two-photon-Raman scattering lines $r_t+/-$ and of their satellites r_t-+ and r_t-- on $\hbar\omega_{exc}$ for various scattering geometries. The solid lines are calculated curves (from Schrey et al. [4.202]).

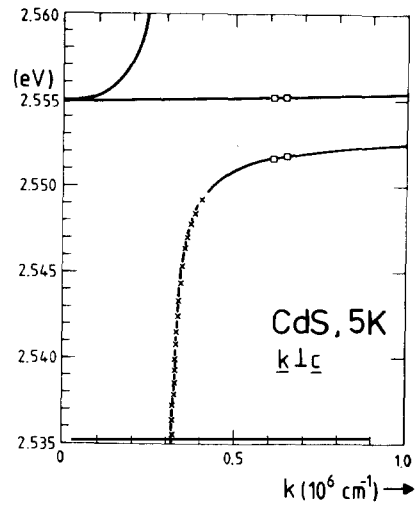

Fig. 44. The dispersion curves of the A-excitonic polariton in CdS for $k \perp c$ as deduced from two-photon-Raman scattering. For the parameters see text. (□) backward scattering, (×) forward scattering, solid lines calculated curves (from Schrey et al. [4.202]).

Concerning the II–VI compounds, such a detailed analysis has been carried out so far only for CdS in the case where the scattering plane is perpendicular to the c-axis [4.202]. A second order two-photon Raman scattering effect has even been identified in CdS [4.202], which manifests itself in satellites r_t^{++}, r_t^{+-}, and r_t^{-+}, r_t^{--} of the lines r_t^+ and r_t^-, respectively. An example is shown in fig. 43. Fig. 44 finally gives the dispersion curve of CdS deduced from TPRS.

The parameters for the A-exciton used in the fit are:

$$E_{x_t}^{\Gamma_5} = 2.5523\,\text{eV} \pm 0.2\,\text{meV}; \qquad E_{x_l}^{\Gamma_5} = 2.5549\,\text{eV} \pm 0.2\,\text{meV}.$$

The value for the triplet exciton taken from [4.203] is $E_x^{\Gamma_6} = 2.5520\,\text{eV}$. The values for $E_{x_l}^{\Gamma_5}$ are in reasonable agreement with the results found by other authors, e.g., from reflection (2.5548 eV [4.204], 2.5546 eV [4.205]) or transmission measurements (2.5547 eV [4.206]). The value of $E_t^{\Gamma_5}$ is slightly lower than the values deduced from the other experiments (2.5527 eV [4.204], 2.5524 eV [4.205] and 2.5528 eV [4.206]). Consequently, the analysis of the TPRS measurements yields a value for $\Delta_{LT} = 2.6\,\text{meV}$, which is a little bit larger than the values in the references cited above (2.1 meV [4.204], 2.2 meV [4.205] and 1.9 meV [4.206]).

A serious discrepancy occurs, however, concerning the background dielectric constant ε_b. The TPRS measurements give $\varepsilon_b = 5.4 \pm 0.4$. From reflection measurements generally values of $\varepsilon_b = 8.5 \pm 1$ are extracted. In [4.207] $\varepsilon_b = 9.3$ has been determined about 2 meV below the exciton resonance from resonant Brillouin scattering (RBS) and the same technique gave $\varepsilon_b = 8.5$ some 5 meV below resonance [4.208].

In fact one expects in the energy region near the excitonic bottle-neck a background dielectric constant in a one oscillator model which is higher than the value of ε_∞ determined from the Reststrahlen absorption region ($\varepsilon_\infty = 5.27$ in CdS [4.209]) because of the oscillators which are lying rather close above the A-exciton. Although the TPRS measurements were carried out some 10 to

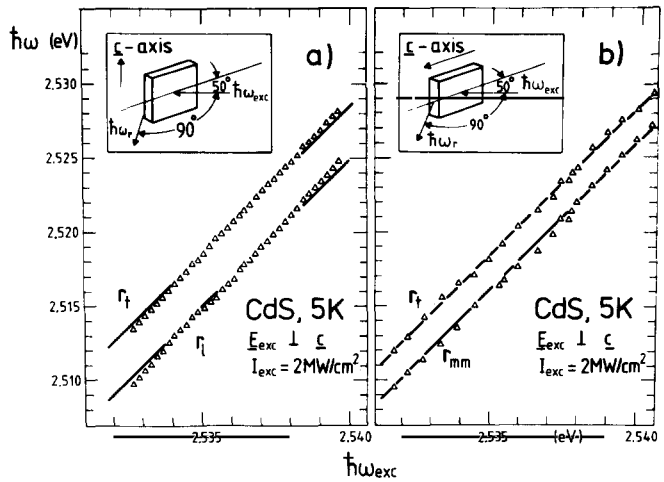

Fig. 45. $\hbar\omega_{r_t}/\hbar\omega_{r_l}$ as a function of $\hbar\omega_{exc}$ for different scattering geometries as indicated in the insets. The solid lines are given by $\hbar\omega_r = 2\hbar\omega_{exc} - E_t$, E_t being 2.5515 eV for $\hbar\omega_{r_t}$ in (a) and (b) and 2.5550 eV and 2.5537 eV in (a) and (b), for r_l and $r_{mm'}$ respectively (from Schrey et al. [4.210]).

30 meV below the resonance, a value of $\varepsilon_b = 5.4 \pm 0.4$ seems to be too low to be consistent with the RBS data. It is unsettled, whether high density effects in the TPRS measurement or the influence of damping may be responsible for this discrepancy [4.202].

If TPRS is carried out with the c-axis in the scattering plane (sp) mixed mode polaritons may be reached in the final state [4.191, 4.210]. This is illustrated in fig. 45. In fig. 45a one has $sp \perp c$ and the final state energies deduced from the slope two lines (4.19) correspond to the values for either pure longitudinal excitons or pure transverse polaritons at their corresponding wavevectors. In the case $sp \parallel c$ (fig. 45b) one has still pure transverse polaritons in the final state. Instead of the longitudinal exciton, now a mixed mode polariton is reached (see 2.3). Its energy deduced from fig. 45b is 2.5538 eV which is in good agreement with the value of 2.5539 eV calculated from the exciton parameters deduced from the TPRS experiments described above. The polarization properties of the TPRS lines of CdS are in agreement with theoretical predictions [4.150, 4.210] for a Γ_1 biexciton ground state. A certain peculiarity occurs in the polariton dispersion curve, if a higher density of excitonic polaritons with a certain energy E_p is present in the crystal. Experimentally, this situation can be realized by illuminating the sample with a sufficiently strong laser of frequency $\hbar\omega_L = E_p$. Due to the strong (giant) oscillator strength of the one-photon transition from E_p to the molecule, a resonance occurs at $E_m - E_p$, which can be seen e.g. with a weak probe beam. Theoretical investigations of this phenomenon are given e.g. in [4.159] and the literature cited therein. Recently, it has been shown how these renormalization effects of the polariton can be calculated easily within a dielectric formalism [4.217]. Fig. 46 shows the deformation of the normal polariton dispersion curve with increasing density of polaritons. A similar effect occurs for the pumplaser itself if it is tuned through $\hbar\omega_L = \frac{1}{2}E_m$ [4.159]. First experimental indications for this effect have been found by [4.105, 4.106] in CuCl, where an anomal behaviour of $\hbar\omega_{r_{t+/-}}$ as a function of $\hbar\omega_{exc}$ has been observed (see fig. 47). Summarizing it can be stated that TPRS allows to perform spectroscopy in momentum space. It is a complementary method to the resonant Brillouin scattering (RBS), see e.g. [4.211] and the literature cited therein. TPRS covers a smaller fraction of the Brillouin-zone only, but does not necessitate the extremely high spectral resolution of the Brillouin scattering, and allows the detection of exciton branches which are inactive in RBS because of different selection rules.

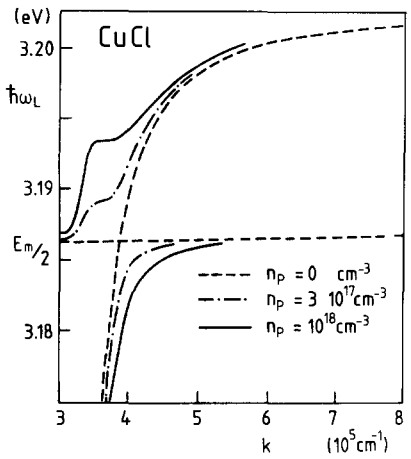

Fig. 46. Calculated dispersion curves for the polaritons excited by a tunable laser beam in a crystal. An anomaly occurs if $\hbar\omega_L$ equals one half of the biexciton energy E_m. The parameter is the density of polaritons created in the sample at the energy $\hbar\omega_L$ (from May et al. [4.159]).

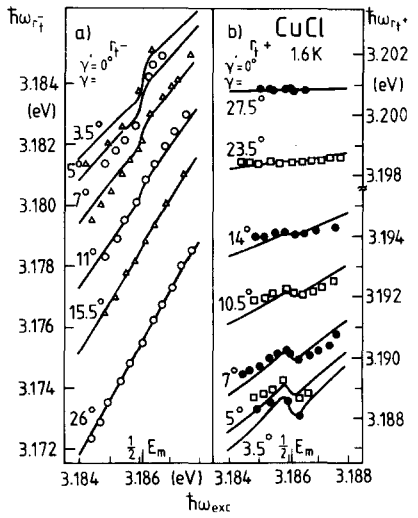

Fig. 47. The dependence of $\hbar\omega_{\Gamma_1^+}$ and $\hbar\omega_{exc}$ for different scattering geometries showing the anomaly at $\hbar\omega_{exc} = \frac{1}{2}E_m$. γ and γ' describe the scattering geometry (fig. 9c). The points give experimental results, the solid lines calculated curves (from Itoh and Suzuki [4.105]).

A comparison between the results of RBS and the dispersion curve deduced from TPRS has been performed for the first time for CdS [4.202] see fig. 48. Good agreement is observed in the exciton-like part of the lower polaron branch. The discrepancies concerning ε_b are evident in the photon-like part of the dispersion curve. The longitudinal excitons have been reached by TPRS only (fig. 44) and not by the RBS experiments in [4.207]. This illustrates the remark about the selection rules given above.

4.5. A comment on the M-band in (wurtzite) II–VI compounds

In the following we list, with a few comments, the main models used in the literature to explain the so-called M-luminescence bands generally observed in (wurtzite) II–VI compounds in the spectral

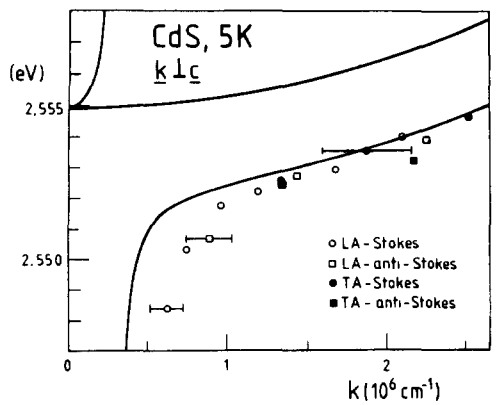

Fig. 48. The A_{Γ_5} polariton dispersion curve of CdS calculated with the parameters deduced from two-photon-Raman scattering compared to results from resonant Brillouin scattering (from Schrey et al. [4.202]).

region of the bound excitons under high excitation:

- The decay of biexcitons into photon-like polaritons and transverse mixed-mode or longitudinal excitons [4.11, 4.19, 4.20, 4.39, 4.41, 4.51, 4.56, 4.66, 4.163–4.176].
  Arguments in vavour of this interpretation are the spectral positions of the M-bands, especially of their high energy edges which correspond approximately to $E_g - E_x^b - E_m^b$. Resonances in excitation spectra of the M-bands in CdS [4.183] and ZnO [4.66] are also compatible with TPE of biexcitons, but are not definitely conclusive because the participation of excited impurity states cannot be excluded [4.184–186]. The behaviour of the M-bands under the application of uniaxial stress perpendicular to the c-axis [4.165] is qualitatively consistent with the biexciton model. A detailed lineshape analysis of the M-band has been performed by different authors [4.19, 4.20], who use in their calculations approximately the same concepts but end up with rather different spectra, which are both confirmed experimentally. For an M-band described by [4.167], which is situated at somewhat higher photon energies, the participation of impurity states also cannot be ruled out [4.178].
- The stimulated emission of the acoustic wing of bound excitons, arising from the radiative recombination of an exciton bound to an impurity under simultaneous emission of an acoustic phonon [1.1, 4.42, 4.65, 4.66].
  Arguments in favour of this process are: the spectral position of the M-band on the low energy side of bound exciton lines, The chemical shift, i.e. the appearance of the M-band with different impurity complexes in different samples, and the coincidence of the excitation spectra for the M-band and for the bound exciton line, as observed in some CdS and ZnO samples [1.1, 4.66].
- Inelastic scattering processes between bound excitons and free carriers or excitons [4.60–4.63]. Arguments supporting this idea are again the chemical shift, and the comparison between observed and calculated lineshapes as a function of I_{exc} and T [4.60–4.63]. The carrier concentrations deduced from the lineshape fit at the highest I_{exc} (up to $10^{18}\,cm^{-3}$) make however excitonic processes in this region unlikely.
- The recombination of electron–hole pairs in a plasma droplet embryo, which forms at an impurity level acting as a nucleation center [4.177]. This interpretation seems reasonable in cases where the M-band is too broad (in ZnO up to 40 meV [4.60]) as to be explained by one of the above mentioned models.
  In view of the different models and of the partly contradictary experimental results, it is reasonable, to assume that the M-band is generally caused by a superposition of different contributions. In some selected samples and under some special experimental conditions, an M-band may be observed which is predominantly caused by only one mechanism. Care has to be taken, however, that such results are not generalized in that way, that the M-bands observed by different authors and under different conditions are all attributed to just this one process.

In a recent experiment [4.212] the temporal evolution of the M-band luminescence has been studied after picosecond excitation. Two components have been observed: One with a rather short time-constant of about 200 ps, which is consistent with biexciton decay. The other component follows closely the decay characteristic of the I_2 bound exciton. This result gives some support to the ideas developed above.

5. Optical properties of the electron-hole plasma

In this section we describe the optical properties of semiconductors in which the density of e–h pairs

is so high, that the bound e–h pair states are no longer stable. The e–h pairs form then a collective state, namely the electron–hole plasma (EHP). In subsection 5.1 we develop the theoretical treatment of EHP and in subsection 5.2 we present experimental results.

5.1. Theoretical aspects

5.1.1. Introduction

In indirect gap semiconductors, e.g. in Ge and Si, it is well established that at low temperatures a first order phase transition between the low density gas phase and a liquid phase (EHL) occurs. The liquid is a degenerate e–h plasma. In recent years experimental evidence was obtained, that also in direct gap semiconductors, e.g. in CdS and GaAs, a similar phase transition occurs (see subsection 5.2). Because the relaxation in a dense plasma takes place in the order of less than picoseconds, one can assume a quasi-equilibrium situation in which the system can be described by a plasma temperature T_P which is however normally different from the lattice temperature T_L. In subsection 5.1.2 we derive the thermodynamic properties of the degenerate e–h plasma by a temperature dependent random-phase-approximation. These calculations are considerably simplified by the use of a plasmon-pole approximation for the screened Coulomb potential.

The most reliable experimental information on the existence and the properties of a degenerate e–h plasma in direct gap semiconductors has been obtained by measurements of the optical gain in highly excited thin crystal platelets [1.23, 1.58, 3.8, 5.1–5.7]. The observed lineshapes of the gain spectra resemble strongly the spectra which one obtains for highly doped materials in p–n junctions, in which the $\boldsymbol{k}$-selection rule is invalidated by the presence of impurities [5.8, 1.24]. In spite of many theoretical attempts [1.23, 5.9–5.11] a successful theory of the lineshape was missing. We show in subsection 5.1.3 that the spectrum can be understood quantitatively if the collision broadening [5.12–5.14] of the individual energy levels, plasmon assisted e–h pair transitions as well as the excitonic enhancement are taken into account [5.11–5.14].

The dynamics of the low-temperature phase transition is in direct gap semiconductors still unknown. Phase transitions in HES are naturally nonequilibrium phase transitions, because the HES is an open system with energy influx and dissipative losses. Therefore, one has to apply the methods, which have been developed in synergetics [see e.g. 5.15] for nonequilibrium phase transitions. In subsection 5.1.4 we apply stochastic rate equations and the corresponding Fokker–Planck equation for the dynamics of the e–h-cluster formation [5.16, 5.17]. This treatment shows that the nucleation of these clusters is a different process in direct and indirect gap semiconductors. Hysteresis effects which are characteristic for the nucleation and decay of e–h drops in indirect gap semiconductors, will not occur in direct gap materials.

Above the critical temperature T_c of the EHP-phase transition the excitons will also ionize when the density of the electronic excitations is increased. This ionization is due to the screening of the attractive e–h Coulomb interactions mainly by the free carriers. The bound e–h pairs are no longer stable and the system is said to undergo a Mott transition. A simple estimate for the Mott density is obtained from the arguments that bound states become impossible if the screening length equals the exciton Bohr radius, i.e. $k_D^2 a_0^2 = 1$, where

$$k_D = \left(\frac{8\pi n e^2}{\varepsilon_0 k_B T_p}\right)^{1/2}$$

is the inverse Debye–Hückel screening length. The condition yields

$$8\pi e^2 n a_0^2/\varepsilon_0 = k_B T_p, \tag{5.1}$$

where n is the density of free carriers and $k_B T_p$ is the thermal plasma energy. The determination of the actual densities of excitons and free carriers for a given excitation intensity is a rather difficult problem, so that conditions like (5.1) are only of limited value. In subsection 5.1.5 we will briefly describe, how the Mott density is calculated if the screening of the Coulomb potential in the exciton is treated dynamically [5.18, 5.19].

5.1.2. Thermodynamic properties of the degenerate e–h plasma

The thermodynamic properties of the plasma which have been calculated e.g. in refs. [5.24, 5.25], can be derived most conveniently by means of temperature-dependent Green's functions [5.25, 5.26]. In systems with long-range Coulomb interactions the use of the Hartree–Fock approximation only gives a qualitative description [5.23, 5.24]. For a quantitative calculation one has to take the dynamic screening of the Coulomb interactions into account. The simplest approach which includes these screening effects is the random-phase-approximation (RPA) or as a further improvement the modified RPA [4.27–5.29]. This approach can be simplified considerably, by describing the screening by the virtual exchange of plasmons. Thus, one simplifies the RPA dielectric function by a plasmon-pole-approximation (see subsection 2.5). Neglecting the collision broadening, the calculation of the thermodynamic properties can be simplified further by a dominant frequency approximation [5.29], which yields a frequency independent self-consistent energy shift.

The self-energy $\Sigma_a(\boldsymbol{k}, \nu)$ is given in RPA by

$$\Sigma_a(\boldsymbol{k}, \nu) = \mathrm{i} \sum_{\boldsymbol{k}', \nu'} V_s(\boldsymbol{k} - \boldsymbol{k}', \nu - \nu')\, G_a(\boldsymbol{k}', \nu'), \tag{5.2}$$

where the index a = e, h describes the electrons or holes. ν is the Matsubara frequency which is given by (with $\hbar = 1$)

$$\nu_a = \frac{\pi(n+1)}{-\mathrm{i}\beta} + \mu_a, \tag{5.3}$$

where μ_a is the quasi-chemical potential of HES and $\beta = 1/k_B T_p$. The screened Coulomb potential has the spectral representation [5.25]

$$V_s(\boldsymbol{k}, \nu - \nu') = V(\boldsymbol{k}) + 2 \int_{-\infty}^{\infty} \frac{\mathrm{d}\omega}{2\pi} \frac{\operatorname{Im} V_s(\boldsymbol{k}, \omega - \mathrm{i}\varepsilon)}{\nu - \nu' - \omega}\ , \tag{5.4}$$

where

$$V_s(\boldsymbol{k}, \omega) = \frac{V(\boldsymbol{k})}{\varepsilon(\boldsymbol{k}, \omega)} = \frac{4\pi e^2}{k^2 \varepsilon(\boldsymbol{k}, \omega)}\ .$$

In the plasmon-pole-approximation $1/\varepsilon$ is given by [2.28]

$$\frac{1}{\varepsilon(\boldsymbol{k},\omega)} = \frac{\omega_{\mathrm{pl}}^2}{2\varepsilon_0\omega_k}\Gamma_k\left(\frac{1}{(\omega-\omega_k)^2+\Gamma_k^2} - \frac{1}{(\omega+\omega_k)^2+\Gamma_k^2}\right), \tag{5.5}$$

where $\omega_{\mathrm{pl}}^2 = 4\pi e^2 n/\varepsilon_0\mu_x$ is the plasma frequency and μ_x the reduced e–h mass, ω_k is the dispersion of the effective plasmon mode

$$\omega_k^2 = \omega_{\mathrm{pl}}^2(1+(k/k_{\mathrm{TF}})^2) + \tfrac{1}{4}(k^2/2\mu_x)^2 - \Gamma_0^2,$$

with

$$k_{\mathrm{TF}}^2 = \frac{4\pi e^2}{\varepsilon_0}\sum_{i=\mathrm{e,h}}(\partial n_i/\partial\mu_i) \quad \text{and} \quad \Gamma_k^2 = \Gamma_0^2 + \frac{k^4}{4}\left(\frac{1}{2\mu_x}\right)^2. \tag{5.6}$$

The lattice polarizability is already taken into account in the static dielectric constant ε_0. Γ_0 is a phenomenological damping constant of the plasma, which is introduced in order to describe the plasma damping due to intervalence band transitions in a real semiconductor.

In strongly ionic semiconductors, however, the lattice polarizability has to be treated dynamically. In this case one has (for simplicity without damping) [5.20, 5.29, 5.30]

$$\varepsilon(\boldsymbol{k},\omega) = \varepsilon_\infty + \frac{(\varepsilon_s-\varepsilon_\infty)\omega_t^2}{\omega_t^2-\omega^2} + \varepsilon_\infty\frac{\omega_{\mathrm{pl}}^2}{\omega_k^2-\omega_{\mathrm{pl}}^2-\omega^2}\quad, \tag{5.7}$$

where ω_t is related to the frequency of the longitudinal optical phonons by $\omega_t = \sqrt{\varepsilon_0/\varepsilon_\infty}\omega_1$. In eq. (5.7) the expression for ω_{pl} and ω_k are of the same form as given in eq. (5.6) if the static dielectric constant ε_0 is replaced by ε_∞.

The frequency dependent self-energy (5.2) determines the Green's function

$$G_a(k,\nu) = \frac{1}{\nu - \varepsilon_a(k) - \Sigma_a(k,\nu)}. \tag{5.8}$$

Following Roesler and Zimmermann [5.31], one can introduce a frequency independent self-energy $\Delta_a(k)$ which will be chosen selfconsistently. By adding and subtracting Δ_a to Σ_a and by expanding the Green's function in terms of the difference $\Sigma_a - \Delta_a$ one gets

$$\begin{aligned} G_a &= \frac{1}{\nu-\varepsilon_a(k)-\Delta_a(k)-(\Sigma_a(k,\nu)-\Delta_a(k))} \\ &\simeq \frac{1}{\nu-\varepsilon_a(k)-\Delta_a(k)} + \frac{\Sigma_a(k,\nu)-\Delta_a(k)}{(\nu-\varepsilon_a(k)-\Delta_a(k))^2} + \dots \end{aligned} \tag{5.9}$$

In order to avoid a double pole in G_a, the numerator of the second term has to vanish at a frequency where the double pole occurs, i.e.

$$\Delta_a(k) = \Sigma_a(k, \varepsilon_a(k)+\Delta_a(k)). \tag{5.10}$$

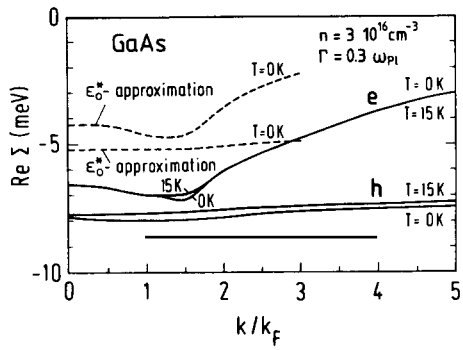

Fig. 49. The real part of the self-energies $\mathrm{Re}\,\Sigma$ of the conduction band and the valence band of GaAs as a function of the normalized wavevector k/k_F calculated with dynamical screening of damped plasmons and phonons. In the ε_0^*-approximation the lattice polarization is treated statically (from Schmitt-Rink et al. [5.76]).

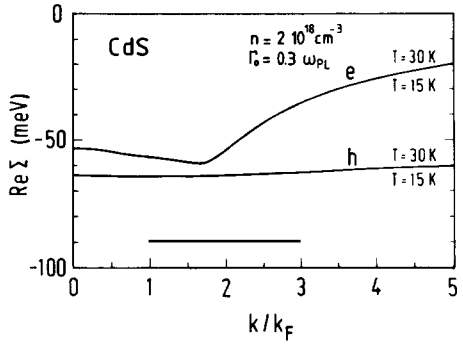

Fig. 50. The real part of the self-energies $\mathrm{Re}\,\Sigma$ of CdS as in fig. 49 (from Schmitt-Rink et al. [5.76]).

With the dominant frequency approximation the Green's function is given only by the first term of (5.9). From this function one obtains immediately the thermal distribution functions

$$f_a(k) = \frac{1}{\exp\{\beta(\varepsilon_a(k) + \Delta_a(k) - \mu_a)\} + 1} \quad . \tag{5.11}$$

Together with $n = \Sigma_k f_a(k)$, one finds the thermodynamic function $\mu_a(n, T)$ with $n = n_e = n_h$.

The energy shifts can now be calculated easily for given n and T. We show results for GaAs and CdS in fig. 49 and fig. 50 according to ref. [5.32]. These figures show the shifts of the energy bands which are obtained by a dynamical treatment of both the lattice and the free-carrier polarization in a phonon–plasmon-pole approximation (as in eq. (5.7) but with damping). The dashed lines in fig. 49 show the results of the so-called ε_0^* approximation, where the lattice polarization is treated statically and where polaron effective masses are used. In order to get the full band renormalization in the ε_0^* approximation one has to add the polaron shifts $\Delta_{LO}^e = -2.6\,\mathrm{meV}$ and $\Delta_{LO}^h = -7.3\,\mathrm{meV}$, so that the resulting plasma energy is lower than in the phonon–plasmon-pole approximation. However, for an accurate calculation one should use the full RPA-expression for the electronic polarization.

In the conduction band the k-dependence of $\Delta_e(k)$ near the center of the Brillouin-zone corresponds to an increase of the effective mass of about 10%. The structure in $\Delta_e(k)$ occurs at the threshold for plasmon emission processes, i.e. at $E_F + \hbar\omega_{pl}$.

The renormalized band edge E_g' is given by $E_g' = E_g + \Delta_e(0) + \Delta_h(0)$ and is plotted together with the resulting chemical potential $\mu = \mu_e + \mu_h$ for CdS according to Roesler and Zimmermann [5.21] in fig. 51. The energy of the plasma $E(n, T)$ can also be obtained from $\mu(n, T)$ by $E(n, T) = (1/n)\int_0^n \mathrm{d}n'\,\mu(n', T)$.

From the minimum energy at $T = 0\,\mathrm{K}$, $E(n_0, T = 0) = E_0$, one gets the binding energy $\varphi = \Delta_{LO} - E_x^b - E_0$, where $\Delta_{LO} = \Delta_{LO}^e + \Delta_{LO}^h$ is the shift of the gap due to polaron effects and E_x^b is the exciton binding energy with respect to the polaron gap. The resulting plasma binding energies φ and plasma densities n_0 are listed in table 6. (A minus sign for φ means that the plasma state is energetically above the free exciton state.)

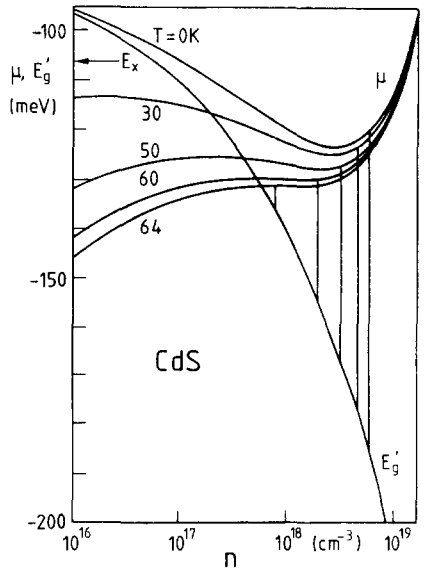

Fig. 51. The reduction of the gap energy E_g' (relative to the unrenormalized gap) and the chemical potential $\mu(n, T)$ for CdS calculated as a function of the e–h pair density n for different plasma temperatures (from Rösler and Zimmermann [5.21]).

As can be seen from table 6, the calculation of the binding energy is a very delicate task, because large numbers are subtracted. This explains, why the theory sometimes fails to predict the bound plasma state, which is observed experimentally.

From $\mu(n, T)$ one finds with a Maxwell construction the quasi-equilibrium phase diagram. Fig. 52 shows the phase diagram which has been constructed according to ref. [5.21] for CdS. On the low-density side, the coexistence curve will be shifted to higher densities due to the existence of excitons, which have not been considered above [see e.g. 5.22–5.24]. The phase diagram of fig. 52 resembles the phase diagrams for indirect gap semiconductors. It has been argued [5.33], that there

Table 6
Calculated and measured plasma parameters for various semiconductors

		Theory		Experiment	
	Δ_{LO} [meV]	n_0 [cm^{-3}]	φ [meV]	n_0 [cm^{-3}]	φ [meV]
CdS	73.1	3.9×10^{18} 5.5×10^{18}	−1 (a) 14 (b)	2×10^{18}–3×10^{18}	≈13 (c) (d) (e)
CdSe	36.7	5.4×10^{17} 8.3×10^{17}	4 (a) 5 (b)	4×10^{17}	2 (c)
ZnO	186.0	2×10^{19}	−21 (b)	~6×10^{18}	22 (e) (f)
GaAs	7.7	2.4×10^{16} 3.4×10^{16}	−0.3 (a) 1.8 (b)	3×10^{16}	4.7 (g) (h)

a Ref. [5.19]
b Ref. [5.20]
c Ref. [5.01]
d Ref. [5.05]
e Ref. [3.08]
f Ref. [5.34]
g Ref. [5.07]
h Ref. (5.02].

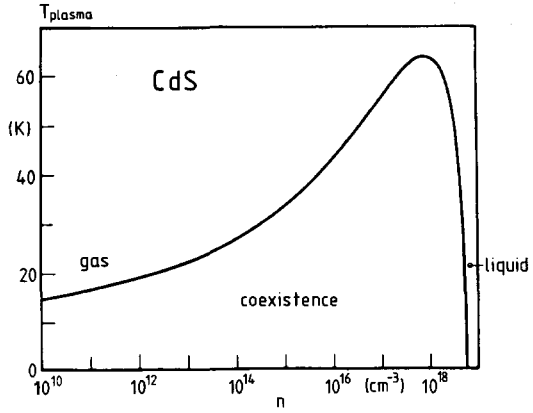

Fig. 52. The phase diagram of electron–hole liquid in CdS as deduced from the calculations shown in fig. 51 (from Rösler and Zimmermann [5.21]).

should exist scaling laws of the form

$$\left.\begin{aligned} &n_c/N = \text{const.} \\ &E_0/k_B T_c = \text{const.} \\ &[\varepsilon_0 T_c n_c^{-1/4}][\varepsilon_0/\mu_x]^{1/4} = \text{const.} \end{aligned}\right\}, \tag{5.12}$$

where μ_x is the reduced e–h-mass and n_c, T_c are the critical density and temperature, respectively. These expressions have been derived from the empirical observation that the sum of the exchange and correlation energy is roughly independent of the band structure.

The use of quasi-equilibrium phase diagrams is however limited especially in direct gap semiconductors. For Ge it is known that a nonequilibrium theory, e.g. the droplet nucleation theory [5.26, 5.35–5.39] has to be used to describe the dynamics of this process appropriately. This treatment also can explain the hysteresis effects [5.40] in the nucleation and the decay of e–h drops in indirect gap semiconductors. In subsection 5.1.4 we develop a nonequilibrium phase transition theory for direct gap semiconductors. In the framework of this theory the phase diagram will be further modified due to the finite lifetimes and due to the influence of the cluster surfaces [5.17, 5.43].

5.1.3. Calculation of the gain spectrum

As already mentioned, gain spectroscopy is one of the most reliable methods to get information on highly excited direct gap semiconductors. However, it turned out, that the lineshape of the observed gain spectra [5.1–5.7, 3.8] of the e–h plasma could not be understood in terms of free particle optical transitions. Reasonable agreement with the observed lineshape could only be obtained if it was assumed that the momentum was not conserved in the optical transition [5.2]. In spite of several theoretical attempts [5.9–5.11, 1.23] a quantitative understanding of the observed lineshape has not been obtained. It will be shown here that one has to take the collision broadening of the single-particle states and the electron–hole correlation in the plasma into account in order to get good agreement with the observed spectra (see subsection 5.2). In the following we will outline the recent work [5.14] by Haug and Tran Thoai.

The imaginary part of the optical (or interband) dielectric function $\varepsilon_2(\infty)$ can be obtained from the imaginary part of the polarization function [5.25]

$$\varepsilon_2(\omega) = C \sum_{k,k'} M_k M_{k'} \operatorname{Im} P_{\mathrm{eh}}(k, -k, k', -k', \omega - \mathrm{i}\varepsilon), \tag{5.13}$$

where M_k is the optical matrix element for a transition between the valence band and the conduction band. This result can be derived from the general definition of the dielectric function [5.26]

$$\varepsilon(1,2) = \int_0^{-\mathrm{i}\beta} \mathrm{d}\bar{4} \frac{\delta U(\bar{4}, 1)}{\delta U_{\mathrm{eff}}(2,2)}, \tag{5.14}$$

where the arguments 1 to 4 represent space and imaginary time coordinates. $U(1,2)$ is the potential of an external perturbation, while $U_{\mathrm{eff}}(1,2)$ is the related effective potential [5.25–26]

$$U_{\mathrm{eff}}(1,2) = U(1,2) - \mathrm{i}\delta(1\text{–}2) \int \mathrm{d}\bar{2}\, V(1,\bar{2})\, G(\bar{2}, \bar{2}^+). \tag{5.15}$$

From (5.14) and (5.15) one obtains

$$\begin{aligned} \varepsilon(1,2) &= \delta(1,2) + \mathrm{i} \int \mathrm{d}\bar{2}\, V(1,\bar{2}) \frac{\delta G(\bar{2}, \bar{2}^+)}{\delta U_{\mathrm{eff}}(2,2)} \\ &= \delta(1,2) - \mathrm{i} \int \mathrm{d}\bar{2}\, V(1,\bar{2})\, P(\bar{2}, \bar{2}^+; 2, 2), \end{aligned} \tag{5.16}$$

where $P = \delta G / \delta U_{\mathrm{eff}}$ is the polarization function. From (5.16) eq. (5.13) can be obtained after expanding the polarization function into Bloch functions [5.26]. The polarization function P_{eh} can be described by the following diagram:

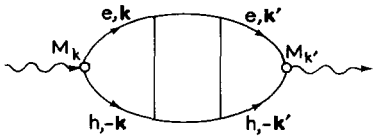

An incoming photon ($\rightsquigarrow$) generates an e–h pair e, k, h, $-k$ with opposite momenta k and $-k$, respectively. The e–h pair interacts, exchanges momentum and recombines eventually by emitting a photon. The polarization function can be calculated from the related temperature-dependent e–h pair function R_{eh} [5.18]:

$$P_{\mathrm{eh}}(p_1, p_2, p_3, p_4, \Omega) = \mathrm{i} \frac{1}{(-\mathrm{i}\beta)} \sum_{\nu} R_{\mathrm{eh}}(p_1, p_2, p_3, p_4, \nu, \Omega). \tag{5.17}$$

R_{eh} depends on two Matsubara frequencies ν and Ω with

$$\nu = \frac{\pi(2n+1)}{-i\beta} + \mu_h$$
$$\Omega = \frac{\pi 2n}{-i\beta} + \mu_e + \mu_h. \tag{5.18}$$

R_{eh} obeys a Bethe–Salpeter equation, which reads in matrix notation

$$R_{eh} = G_e G_h - iG_e G_h V_s R_{eh}. \tag{5.19}$$

Instead of solving directly eq. (5.19), we rewrite it by introducing a T-matrix

$$R_{eh} = G_e G_h - iG_e G_h T G_e G_h, \quad \text{where} \quad T = V_s - iV_s G_e G_h T \tag{5.20}$$

also obeys a Bethe–Salpeter equation. V_s is again the screened e–h Coulomb interaction. With this formulation the optical dielectric function contains two contributions

$$\varepsilon_2(\omega) = C\,\mathrm{Im}\sum iMG_e G_h M + C\,\mathrm{Im}\sum MG_e G_h T G_e G_h M = \alpha_1(\omega) + \alpha_2(\omega). \tag{5.21}$$

Diagrammatically, this means

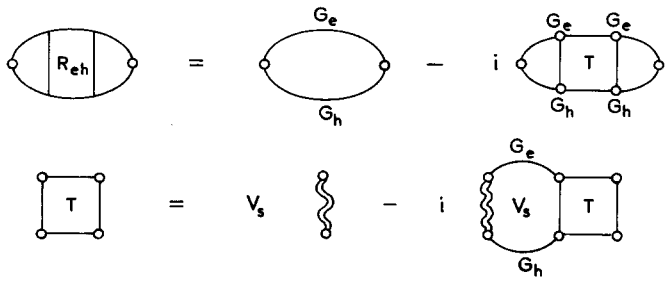

The diagram shows, that the T-matrix describes the multiple e–h scattering, i.e. it takes into account the strong e–h correlation due to their attractive interaction.

For the quantitative understanding of the gain spectrum, it is important to take also the imaginary parts of the electron and hole self-energies into account. As already discussed in subsection 5.1 one should use for this purpose the RPA intraband dielectric function (2.28). If one wants to simplify the calculation by the plasmon-pole approximation one has to take into account the damping of the plasmons due to intervalence band transitions [5.13, 2.27]. Following Rice [2.27], we use a plasmon-pole approximation with damping in the form given in subsection 2.5, i.e. we are treating the lattice polarizability statically (ε_0^*-approximation). The calculation of the real part of the self-energies has already been described in subsection 5.1.2 and will not be repeated here. For the imaginary part of Σ we get from eq. (5.2) after the summation over the Matsubara frequency with $\mathrm{Im}\,\Sigma_a(\boldsymbol{k}, \omega) = \Gamma_a(\boldsymbol{k}, \omega)$:

$$\Gamma_a(\boldsymbol{k}, \omega) = \sum_{\boldsymbol{k}'} \int_{-\infty}^{\infty} d\omega'\, \mathrm{Im}\, V_s(\boldsymbol{k} - \boldsymbol{k}', \omega' - i\varepsilon)\,(g(\omega') + 1 - f_a(\boldsymbol{k}))\delta(\omega - \omega' - e_a(\boldsymbol{k})). \tag{5.22}$$

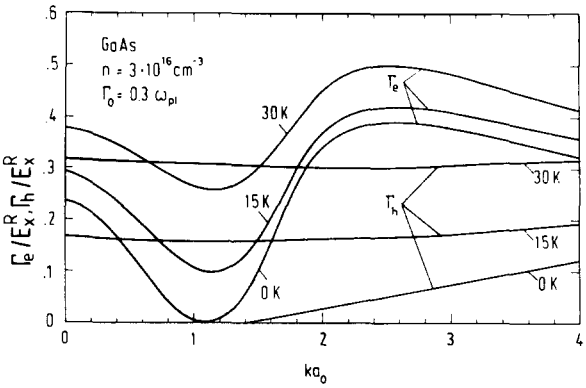

Fig. 53. Calculated collision broadenings Γ_e and Γ_h for GaAs as a function of the wavevector k for different temperatures (from Haug and Tran Thoai [5.14]).

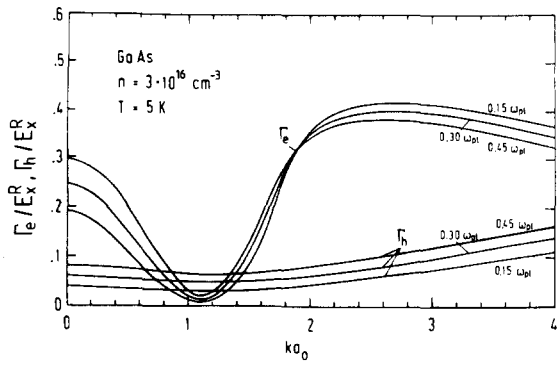

Fig. 54. Calculated collision broadenings Γ_e and Γ_h for GaAs as a function of the wavevector k for various plasma damping constants Γ_0 (from Haug and Tran Thoai [5.14]).

The collision broadening is determined by the scattering rates in and out the state k by emission or absorption of plasmons:

$$(1+g)(1-f_a(k'))+gf_a(k')=1+g-f_a(k') \tag{5.23}$$

where $g(\omega')$ is the plasmon population factor

$$g(\omega')=(\exp(\hbar\omega/k_BT)-1)^{-1}.$$

The resulting collision broadenings (in the ε_0^*-approximation) are shown in fig. 53 for the electrons and holes in GaAs at various temperatures. The fig. 54 shows the weak dependence of Γ_e and Γ_h on the phenomenological plasmon damping constant Γ_0 (see eq. (5.6)). The final results for the optical dielectric constant are still less dependent on the actual value of Γ_0, as long as it is above a certain limiting value. For the rest of the paper we always use $\Gamma_0 = 0.3\,\omega_{pl}$.

The collision broadenings vanish quadratically at the Fermi energy at $T = 0$ K. This fact can immediately be understood, because an electron above the Fermi sea can be scattered into a decreasing number of final states by plasmon emission, if the electron state approaches the Fermi level. An equivalent argument holds for a hole in the Fermi sea (see fig. 55).

The real parts of the self-energies which have been calculated in subsection 5.1.3 will not be treated explicitly here. We will measure the frequency with respect to the renormalized band edge E_g'. With the knowledge of the complex self-energies the first bubble-diagram $\alpha_1(\omega)$ can now be calculated. The frequency summation and an analytic continuation $\Omega = \omega - i\varepsilon$ yield

$$\alpha_1(\omega)=C\sum_k \frac{M_k^2(1-f_e(k)-f_h(k))(\Gamma_e(k,\omega-e_h(k))+\Gamma_h(k,\omega-e_e(k)))}{(\omega-e_e(k)-e_h(k))^2+(\Gamma_e(k,\omega-e_h(k))+\Gamma_h(k,\omega-e_e(k)))^2}\,, \tag{5.24}$$

where the frequency shifts in the arguments of the collision broadening have been taken into account symmetrically. Landsberg [5.12] derived eq. (5.24) without the frequency shifts in the damping

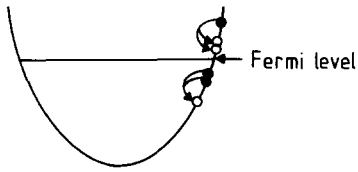

Fig. 55. Sketch of the collision broadening processes, above and below the Fermi level.

constants. Introducing the compound matrix element for a plasmon-assisted transition

$$G_k = \frac{M_k}{(\omega - e_e(\boldsymbol{k}) - e_h(\boldsymbol{k})) - i(\Gamma_e(\omega - e_h(\boldsymbol{k})) + \Gamma_h(\omega - e_e(\boldsymbol{k})))} \tag{5.25}$$

we get by combining eqs. (5.22) and (5.24)

$$\alpha_1(\omega) = 2\pi C \sum_{\boldsymbol{k},\boldsymbol{k}'} \int_{-\infty}^{\infty} \frac{d\omega'}{2\pi} \operatorname{Im} V_s(\boldsymbol{k} - \boldsymbol{k}', \omega' - i\varepsilon)\, \delta(\omega - \omega' - e_e(\boldsymbol{k}') - e_h(\boldsymbol{k}))$$

$$\times \{|G_k|^2 (1 - f_e(\boldsymbol{k}) - f_h(\boldsymbol{k}))(1 + g(\omega') - f_e(\boldsymbol{k}')) + |G_{k'}|^2 (1 - f_e(\boldsymbol{k}') - f_h(\boldsymbol{k}'))(1 + g(\omega') - f_h(\boldsymbol{k}))\}. \tag{5.26}$$

Thus, the contribution of the first bubble diagram has the form of a spectrum due to plasmon-assisted transitions from the electron state $\boldsymbol{k}'$ to the hole state $\boldsymbol{k}$ by emission or absorption of a plasmon with frequency ω', which is integrated over positive and negative frequencies.

In order to calculate the contribution of the second diagram $\alpha_2(\omega)$, we have to calculate the T-matrix with the following arguments

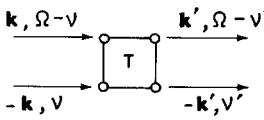

$$= T(\boldsymbol{k}, \boldsymbol{k}', \nu, \nu', \Omega). \tag{5.27}$$

The Bethe–Salpeter equation (5.19) is

$$T(\boldsymbol{k}, \boldsymbol{k}', \nu, \nu', \Omega) = V_s(\boldsymbol{k} - \boldsymbol{k}', \nu - \nu')$$

$$- \frac{i}{(-i\beta)} \sum_{\bar{\boldsymbol{k}}, \bar{\nu}} V_s(\boldsymbol{k}, \boldsymbol{k}', \nu - \bar{\nu})\, G_e(\bar{\boldsymbol{k}}, \Omega - \bar{\nu})\, G_h(\bar{\boldsymbol{k}}, \bar{\nu})\, T(\bar{\boldsymbol{k}}, \boldsymbol{k}', \bar{\nu}, \nu', \Omega). \tag{5.28}$$

We solve this integral equation approximately by factorizing the integral kernel

$$V_s(\boldsymbol{k} - \bar{\boldsymbol{k}}, \nu - \bar{\nu}) = \tfrac{1}{2} V_s^{1/2}(\boldsymbol{k}', \nu - \nu^*)\, V_s^{1/2}(\bar{\boldsymbol{k}}, \bar{\nu} - \nu^*) \tag{5.29}$$

where ν^* is a dominant frequency, which has to be chosen adequately. The factor $\frac{1}{2}$ is necessary in order to recover the low-density result.

Defining

$$\tilde{T}(\boldsymbol{k}', \nu', \Omega) = -\mathrm{i}\frac{1}{(-\mathrm{i}\beta)}\sum_{\bar{\boldsymbol{k}},\bar{\nu}} T(\bar{\boldsymbol{k}}, \boldsymbol{k}', \bar{\nu}, \nu', \Omega)\, V_s^{1/2}(\bar{\boldsymbol{k}}, \bar{\nu} - \nu^*)\, G_e(\bar{\boldsymbol{k}}, \Omega - \bar{\nu})\, G_h(\bar{\boldsymbol{k}}, \bar{\nu}), \tag{5.30}$$

one obtains

$$T(\boldsymbol{k}, \boldsymbol{k}', \nu, \nu', \Omega) = V_s(\boldsymbol{k} - \boldsymbol{k}', \nu - \nu') + \tfrac{1}{2} V_s^{1/2}(\boldsymbol{k}, \nu - \nu^*)\, \tilde{T}(\boldsymbol{k}', \nu', \Omega). \tag{5.31}$$

Multiplying this equation by $V_s^{1/2}(\boldsymbol{k}, \nu - \nu^*)\, G_e(\boldsymbol{k}, \Omega - \nu)\, G_h(\boldsymbol{k}, \nu)$ and summing over ν and $\boldsymbol{k}$ yields

$$\tilde{T}(\boldsymbol{k}', \nu', \Omega) = \frac{A(\Omega)\, V_s(\boldsymbol{k}', \nu' - \nu^*)}{1 - A(\Omega)} \tag{5.32}$$

with

$$A(\Omega) = -\frac{\mathrm{i}}{2}\frac{1}{-\mathrm{i}\beta}\sum_{\nu,\boldsymbol{k}} V_s(\boldsymbol{k}, \nu - \nu)\, G_e(\boldsymbol{k}, \Omega - \nu)\, G_h(\boldsymbol{k}, \nu) \tag{5.33}$$

and finally, we obtain for the T-matrix

$$T(\boldsymbol{k}, \boldsymbol{k}', \nu, \nu', \Omega) = \frac{V_s(\boldsymbol{k} - \boldsymbol{k}', \nu - \nu')}{1 - A(\Omega)}. \tag{5.34}$$

The factor $1/(1 - A(\Omega))$ is the excitonic enhancement factor. At very low temperatures this factor can become divergent, signaling an instability of the normal plasma phase with respect to the excitonic phase.

The contribution of the T-matrix diagram to the gain spectrum therefore is

$$\alpha_2(\omega) = C\,\mathrm{Im}\frac{1}{(-\mathrm{i}\beta)}\sum_{\boldsymbol{k},\boldsymbol{k}',\nu,\nu'} M_k M_{k'} G_e(\boldsymbol{k}, \Omega - \nu)\, G_h(\boldsymbol{k}, \nu)\, G_e(\boldsymbol{k}', \Omega - \nu')\, G_h(\boldsymbol{k}', \nu')$$

$$\times\, V_s(\boldsymbol{k} - \boldsymbol{k}', \nu - \nu')/(1 - A(\omega)), \tag{5.35}$$

with the analytic continuation $\Omega = \omega - \mathrm{i}\varepsilon$.

In order to simplify the numerical calculation, we use only the real part of the enhancement function $A(\omega)$ and calculate it in the static approximation

$$\mathrm{Re}\, A(\omega) = \frac{1}{2}\sum_{\boldsymbol{k}} V_s(\boldsymbol{k}, 0)\frac{(f_e(\boldsymbol{k}) + f_h(\boldsymbol{k}) - 1)(\omega - e_e(\boldsymbol{k}) - e_h(\boldsymbol{k}))}{(\omega - e_e(\boldsymbol{k}) - e_h(\boldsymbol{k}))^2 + [\Gamma_e(\boldsymbol{k}, \omega - e_h(\boldsymbol{k})) + \Gamma_h(\boldsymbol{k}, \omega - e_e(\boldsymbol{k}))]^2} \tag{5.36}$$

The resulting excitonic enhancement factor is shown in fig. 56 for GaAs.

The frequency summations in (5.35) yield

$$\alpha_2(\omega) = \frac{-2C}{1 - \mathrm{Re}\, A(\omega)}\sum_{\boldsymbol{k},\boldsymbol{k}'} V_s(\boldsymbol{k} - \boldsymbol{k}', 0)(|G_k G_{k'}|^2/M_k M_{k'})(f_e(\boldsymbol{k}) + f_h(\boldsymbol{k}) - 1)$$

$$\times\, (f_e(\boldsymbol{k}') + f_h(\boldsymbol{k}') - 1)[\Gamma_e(\boldsymbol{k}, \omega - e_h(\boldsymbol{k})) + \Gamma_h(\boldsymbol{k}, \omega - e_e(\boldsymbol{k}))](\omega - e_e(\boldsymbol{k}') - e_h(\boldsymbol{k}')), \tag{5.37}$$

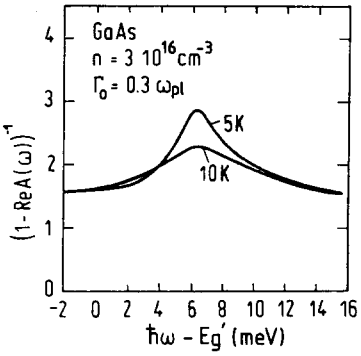

Fig. 56. Enhancement factor $(1 - \mathrm{Re}\, A(\omega))^{-1}$ of GaAs as a function of the energy difference (from Haug and Tran Thoai [5.14]).

where again V_s has been used in the static approximation. The total numerical result for $\alpha_1(\omega)$ and $\varepsilon_2(\omega) = \alpha_1(\omega) + \alpha_2(\omega)$ are shown in fig. 57 for GaAs and fig. 58 for CdS. For GaAs we used the material parameters $m_e = 0.067\, m_0$, $m_h = 0.54\, m_0$ and $\varepsilon_0 = 12.9$, and for CdS $m_e = 0.205\, m_0$, $m_h \perp = 0.7\, m_0$, $m_h \| = 5\, m_0$ and $\varepsilon_0 = 9.5$.

The comparison of the calculated spectra with corresponding gain measurements for GaAs and CdS is presented in subsection 5.2.2, where we show that the calculated spectra are in excellent agreement with the experimental ones. Similar calculations without damping have been carried out by Arya and Hanke [5.41]. Recently, we extended the theory for polar semiconductors and developed an approximation scheme for the calculation of the T-matrix, which does not rely on a factorization approximation [5.76] and obtains very similar spectra as shown in figs. 57 and 58.

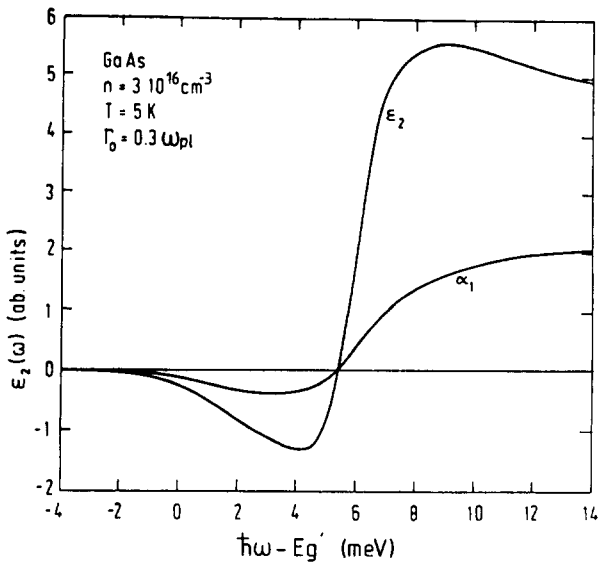

Fig. 57. Imaginary part ε_2 of the dielectric constant versus frequency for GaAs at $T = 5$ K. α_1 is the contribution of the first bubble diagram (from Haug and Tran Thoai [5.14]).

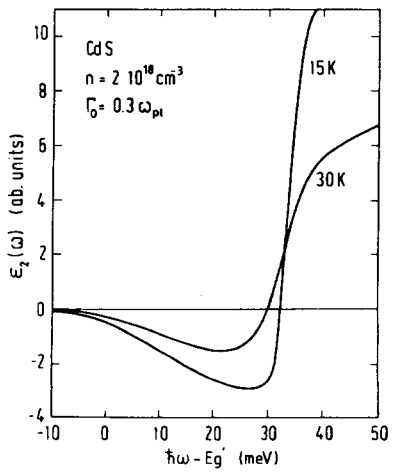

Fig. 58. Calculated gain spectrum $\varepsilon_2(\omega)$ for CdS at $T_p = 15$ K and $T_p = 30$ K for $n = 2 \times 10^{18}$ cm^{-3} and $\Gamma_0 = 0.3\, \omega_{pL}$ (from Haug and Tran Thoai [5.14]).

5.1.4. *The formation of e–h plasma clusters*

We turn now to the dynamical description of the phase transition from the low density gas phase, which consists mainly of excitons, to the high density e–h liquid. In Ge the dynamics have been described successfully by a nucleation theory for the e–h droplets in terms of master and Fokker–Planck equations [5.16, 5.35–5.38].

We will apply these concepts of nonequilibrium phase transitions [5.15] to study the characteristic differences between the plasma cluster formation in direct and indirect gap semiconductors.

Following the recent work by Koch and Haug [5.17], we describe the formation of e–h clusters by means of an indeterministic rate equation (Langevin equation):

$$\mathrm{d}\hat{n}/\mathrm{d}t = g_{\hat{n}} - l_{\hat{n}} + F_{\hat{n}}(t), \tag{5.38}$$

where $\hat{n}$ is the number of e–h pairs in the cluster.

$$g_{\hat{n}} = b\sqrt{T} \cdot n_{\mathrm{x}} \cdot \hat{n}^{2/3} \tag{5.39}$$

is the gain rate due to the collection of excitons at the cluster surface. n_{x} is the exciton density. The square root of the temperature is due to the thermal velocity of the excitons.

$$l_{\hat{n}} = \hat{n}/\tau(\hat{n}) + a(\hat{n})\,\hat{n}^{2/3} \tag{5.40}$$

is the loss term due to recombination and evaporation. $\tau(\hat{n})$ is the lifetime of the particles and $a(\hat{n})$ is the Richardson–Dushman evaporation rate

$$a(\hat{n}) = aT^2 \exp\{-\beta(\phi - c\sigma/\hat{n}^{1/3})\}, \tag{5.41}$$

ϕ is the bulk binding energy which is corrected by a term which is proportional to the surface tension σ of spherical drops. a, b and c are constants and $\beta = 1/k_{\mathrm{B}}T_{\mathrm{p}}$.

The statistical fluctuations are of shot noise character

$$\langle F_{\hat{n}}(t)\, F_{\hat{n}}(s)\rangle = \delta(t-s)Q_{\hat{n}}, \tag{5.42}$$

where

$$Q_{\hat{n}} = l_{\hat{n}} + g_{\hat{n}}.$$

Equivalently to the Langevin equation (5.38) is the Fokker–Planck equation for the cluster distribution function $f_{\hat{n}}$

$$\frac{\partial}{\partial t} f_{\hat{n}} = -\frac{\partial}{\partial \hat{n}} J_{\hat{n}}, \tag{5.43}$$

where the probability current density is given by

$$J_{\hat{n}} = f_{\hat{n}}(g_{\hat{n}} - l_{\hat{n}}) - \frac{1}{2}\frac{\partial}{\partial \hat{n}}(Q_{\hat{n}} f_{\hat{n}}). \tag{5.44}$$

More rigorously, the Fokker–Planck equation (5.43, 5.44) can be derived from the master equation by making a Kramers–Moyal expansion. In addition to eq. (5.37) we have the equation for the conservation of particles

$$\frac{\partial}{\partial t}N+\frac{\partial}{\partial t}n_x=G-\frac{N}{\tau_p}-\frac{n_x}{\tau_x},\ \text{where} \tag{5.45}$$

τ_x is the lifetime of the excitons, τ_p is the lifetime of electron–hole pairs in the cluster, $N=\int \hat{n} f(\hat{n})\,\mathrm{d}\hat{n}$, and G is the laser generation rate.

In the stationary case, the probability current density vanishes, i.e. $J_n=0$. An elementary integration yields the equilibrium distribution

$$f_{\hat{n}}=\text{const}\cdot\exp(-\psi/k_BT), \tag{5.46}$$

where

$$\psi(\hat{n},n_x)=2k_BT\int_1^{\hat{n}}\mathrm{d}\hat{n}'\,(l_{\hat{n}'}-g_{\hat{n}'}+\tfrac{1}{2}\,\partial Q_{\hat{n}'}/\partial\hat{n}')/Q_{\hat{n}'} \tag{5.47}$$

is the Ginzburg–Landau potential. For the clusters close to the stable size, the loss rate $l_{\hat{n}}$ and the gain rate $g_{\hat{n}}$ are nearly equal. Under this condition the potential can be approximated by [5.38]

$$\psi(\hat{n},n_x)=\sigma\hat{n}^2/3s_0-\hat{n}k_BT\ln\left(\frac{n_x}{n_s}\right)+k_BT\sum_{m=2}^{\hat{n}}\ln\left(1+\frac{m^{1/3}}{\tau a(m)}\right), \tag{5.48}$$

where s_0 is the surface energy per surface particle and n_s is the classical saturation density $n_s\propto \mathrm{e}^{-\beta\phi}$. Numerically, eq. (5.48) and eq. (5.47) yield nearly identical results.

Estimating the surface energies by the result of ref. [5.42], we can calculate ψ for a given exciton concentration for various semiconductors with the following material parameters:

Table 7

	σ[erg/cm^2]	n_0[cm^{-3}]	ϕ[meV]	τ[s]
Ge	3.5×10^{-4}	2.28×10^{17}	2	11×10^{-6}
GaAs	7.6×10^{-5}	5×10^{16}	4	10^{-9}
CdS	3.5×10^{-3}	2×10^{18}	14	10^{-9}

Fig. 59 shows the resulting potentials for Ge for various exciton concentrations. The potential is characterized by the existence of a critical droplet size which is roughly determined by the balance between the rates of collection and evaporation. Recombination losses are dominating only for large clusters. Under these conditions we have a first order nonequilibrium phase transition. Such a Ginzburg–Landau potential immediately explains the hysteresis phenomena which have been observed for the nucleation and decay of e–h droplets in indirect gap semiconductors [5.40].

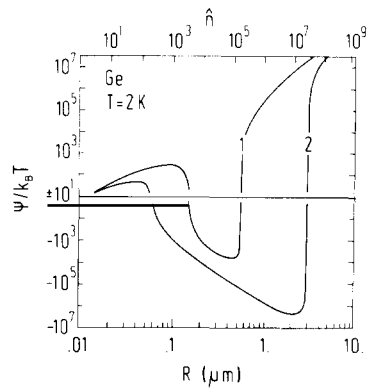

Fig. 59. The calculated Ginzburg–Landau potential ψ as a function of the mean droplet radius R (or the number $\hat{n}$ of electron–hole pairs per droplet) for Ge at exciton densities n_x of $0.41 \times 10^{12}\,cm^{-3}$ (1) and $1.2 \times 10^{12}\,cm^{-3}$ (2). (From Koch and Haug [5.17].)

In figs. 60 and 61 ψ is plotted for two direct gap materials namely for GaAs and CdS, respectively. The recombination losses dominate at all densities over the evaporation losses, so that no critical cluster size exists. At low exciton concentrations small cluster sizes are stable (i.e. excitons and possibly excitonic molecules). With growing exciton concentrations the potential well around the $\hat{n} = 1$ minimum gets broader and eventually the minimum shifts to finite cluster sizes. But at no concentration the stationary cluster size distribution function has two well developed peaks. Thus, for direct gap semiconductors the e–h cluster formation does not show hysteresis phenomena. Instead of the usual coexistence region in which one has liquid drops in the gas phase here the intermediate region consists of a locally inhomogeneous phase of e–h clusters with a relatively broad size distribution. Even in Ge the Ginzburg–Landau potential changes at very low temperatures its character [5.43] from first to second order.

The potential and the stationary cluster distribution depend on the exciton density. In order to determine the actual stationary exciton density one has to solve the time-dependent Fokker–Planck equation. For direct gap semiconductors large clusters cannot be formed because they could only be sustained by a high stationary exciton concentration. But the exciton concentration is determined by the tail of the cluster size distribution and would be too low for large clusters. Consequently, only small

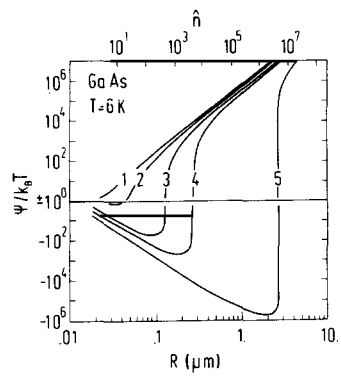

Fig. 60. Ginzburg–Landau potential for GaAs [5.17] for varying exciton densities n_x ($10^{14}\,cm^{-3}$): 0.67 (1), 1.33 (2), 3.3 (3), 6.7 (4) and 67.0 (5).

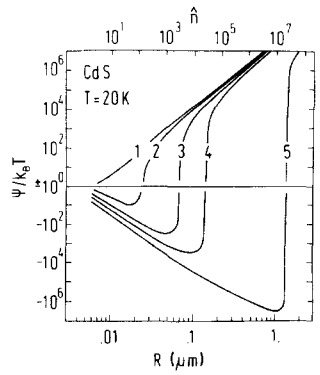

Fig. 61. Ginzburg–Landau potential for CdS [5.17] for varying exciton densities n_x ($10^{16}\,cm^{-3}$): 0.124 (1), 0.249 (2), 0.623 (3), 1.24 (4) and 12.45 (5).

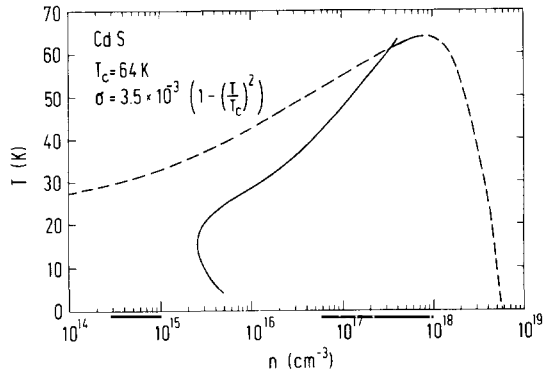

Fig. 62. The calculated phase diagram for the electron–hole liquid in CdS assuming an infinite (------) and finite (———) lifetime of the e–h pairs. σ is the surface tension and T_c the critical temperature. (------ from Rösler and Zimmermann [5.21]; ——— from Koch [5.44].)

clusters will be formed. The available experimental observations on the e–h phase transition in GaAs and CdS seem to be compatible with the above conclusions (see subsection 5.2). Naturally, the interpretation of experiments gets complicated, if the excitation is spatially inhomogeneous, which is generally the case for one-photon excitation. From the generalized Ginzburg–Landau potential one can now calculate the onset of cluster nucleation as a function of n and T. A phase diagram which includes these nonequilibrium effects calculated by Koch [5.44] for CdS is shown in fig. 62.

5.1.5. On the Mott transition in HES

Above the critical temperature T_c of the e–h liquid phase transitions the binding energy of the excitons gradually decreases as the density of the electronic excitations increases. The main change in the exciton binding energy is due to the screening of the free carriers. In the static approximation the screened e–h Coulomb potential is given by $-(e^2/\varepsilon_0 r)\exp(-k_D r)$, where k_D is the inverse Debye–Hückel screening length. For this potential bound states exist only if $k_D a_0 \leq 1.19$, where a_0 is the exciton Bohr radius without screening [5.45]. This condition for the existence of excitons is usually called the Mott criterion, see e.g. [5.46]. The validity of the use of a static screening can be questioned in a situation where the electron and the hole are in a state of rapid relative motion. One would expect that the dynamically screening of the free carriers becomes ineffective if the plasmon energy is much lower than the exciton binding energy. In ref. [5.18] the influence of the dynamically screened Coulomb potential on the exciton was investigated by treating Bethe–Salpeter equations for the e–h pair function

$$R_{eh}(12, 34) = G_e(1, 3)\, G_h(2, 4) - iG_e(1, \bar{1})\, G_h(2, \bar{2})\, V_s(\bar{1}, \bar{2})\, R_{eh}(\overline{12}, 34). \tag{5.49}$$

Due to the dynamical screening one has to use a two-frequency pair function:

$$R_{eh}(\boldsymbol{p}_1, \boldsymbol{p}_2, \boldsymbol{p}_3, \boldsymbol{p}_4, \nu, \Omega) = G_e(\boldsymbol{p}_1, \Omega - \nu)\, G_h(\boldsymbol{p}_1, \nu)\Big[\delta_{\boldsymbol{p}_1,\boldsymbol{p}_3}\delta_{\boldsymbol{p}_2,\boldsymbol{p}_4}$$

$$-\frac{1}{-i\beta}\sum_{\nu'\boldsymbol{k}}\frac{V_s(\boldsymbol{q}, \nu' - \nu)}{i}\, R_{eh}(\boldsymbol{p}_1 + \boldsymbol{k}, \boldsymbol{p}_2 - \boldsymbol{k}, \boldsymbol{p}_3, \boldsymbol{p}_4, \nu', \Omega)\Big]. \tag{5.50}$$

This equation has been treated in ref. [5.18] in the framework of a plasmon-pole-approximation but

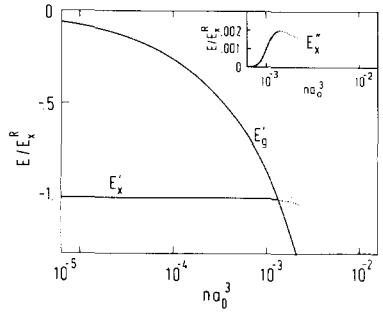

Fig. 63. Real and imaginary part of the exciton energy E_x' and E_x'', respectively, as a function of the plasma density n, for $k_BT/E_x^R = 0.1$ (from Zimmermann et al. [5.19]).

without the self-energy corrections in the single-particle Green's functions. We have seen in subsection 5.1.1 that the real part of the self-energy gives the band edge renormalization. Thus, a complete treatment of an exciton in a gas of free carriers has to take into account both the vertex corrections contained in the screened potential and the self-energy corrections of the single-particle energies. These calculations have been done by Zimmermann et al. [5.19].

The resulting complex energy of the lowest bound exciton level is shown in fig. 63. The exciton level is seen to be rather independent of the concentration of free carriers. Thus, the reduction of the binding energy is mainly due to the reduction of the renormalized band edge E_g'. The broadening of the excitonic level only occurs shortly before the ionization of the exciton takes place. The resulting ionization density is not very different from the prediction of the simple static Mott criterion. Similar results for the exciton binding energies are also contained in earlier treatments [5.47, 5.48].

As already discussed in subsection 5.1.3 the e–h pair function is related to the dielectric function. The contribution of the lowest bound exciton to the dielectric function is given by [5.49]

$$\varepsilon(\omega) = \varepsilon_0 - \mathrm{i}8\pi e^2 \sum |M|^2 \tilde{R}_{\mathrm{eh}}(\boldsymbol{p}_1, \boldsymbol{p}_2, \boldsymbol{p}_3, \boldsymbol{p}_4, \omega)$$

$$\simeq \varepsilon_0 + 16\pi e^2 \frac{\operatorname{Re} E_x}{(\operatorname{Re} E_x)^2 - (\omega + \mathrm{i} \operatorname{Im} E_x)^2} |\varphi_0(0)|^2 M^2, \tag{5.51}$$

where

$$\tilde{R}_{\mathrm{eh}}(\omega) = \frac{1}{-\mathrm{i}\beta} \sum_{\nu} R_{\mathrm{eh}}(\nu, \Omega)|_{\Omega = \omega - \mathrm{i}\varepsilon}.$$

$\operatorname{Re} E_x$ is the real part of the exciton energy, $\operatorname{Im} E_x = \Gamma$ is the broadening of this exciton level, $\varphi_0(\boldsymbol{r})$ is the wave function of the relative exciton motion. This formula can be used together with the results shown in fig. 64 to analyse reflection spectra of HES in the exciton region (see subsection 5.2.1).

A still unsolved theoretical problem is the calculation of the partition function which holds for the whole relevant density range. The knowledge of such an equation of state which covers the low-density regime as well as the high-density plasma regime is necessary for the discussion of the critical region of the e–h liquid phase transition and for the detailed description of the Mott transition. First steps in this direction have been done by [5.50].

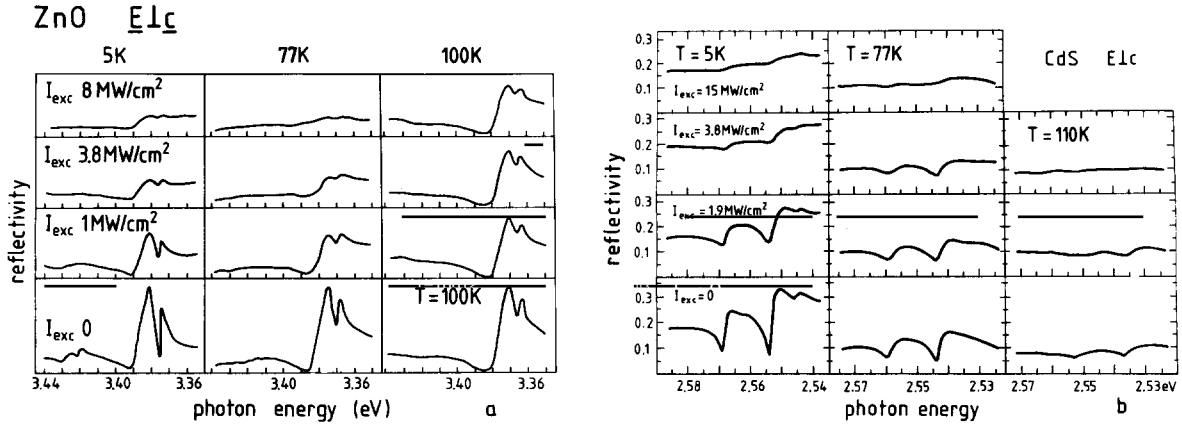

Fig. 64. The excitonic reflection spectra of ZnO (a) and CdS (b) for $E \perp c$ and for different values of I_{exc} and $T_{lattice}$ (from Bohnert et al. [3.8]).

5.2. Experimental aspects

The formation of an EHP is especially favoured in semiconductors with excitons which have a large Bohr radius and which are only weakly bound. This condition is well fulfilled, e.g., for several direct III–V compounds and to a minor degree for the II–VI semiconductors. In the Cu-halides, the exciton is so strongly bound (in CuCl $E_x^b = 190$ meV and $a_0 = 7$ Å, respectively) that an EHP might be formed only at excitations intensities which are above the damage threshold of the sample. In fact, no indications for an EHP have been reported so far for the Cu-halides [3.14, 5.74] up to the highest I_{exc}. Therefore, our discussion will be limited to the direct gap III–V compounds (especially GaAs) and to II–VI materials (mainly CdS and ZnO).

5.2.1. Reflection- and absorption spectroscopy

Since excitons do not longer exist in an EHP, those structures which are characteristic for excitons should disappear from the reflection and absorption spectra of semiconductors with an EHP. Indeed a significant decrease of the excitonic reflection signals with increasing I_{exc} has been observed by several authors. See for CdS [3.8, 5.6, 5.51–5.53] and for ZnO [3.8, 5.54]. Examples for the $n = 1$ A Γ_5 and B Γ_5 excitons in CdS and ZnO are shown in fig. 64a, b. In ZnO, in addition the $n = 2$ excitons are observed at low lattice temperature T_L and I_{exc}. Because of their large radii, they disappear more rapidly than the $n = 1$ states. The results for CdS are in qualitative agreement with theoretical predictions (see subsection 5.1.5 [5.19]).

A detailed analysis of the reflection spectra of ZnO and CdS has been performed e.g. in [3.8].

For $I_{exc} > 0$ several models are tested, which are potentially able to explain the disappearance of the excitonic reflection structures. However, first the reflection spectra for $I_{exc} = 0$ have to be fitted using standard techniques. The authors of [3.8] take into account: an exciton free surface layer of thickness Δ, spatial dispersion, using the additional boundary conditions of Pekar [5.55, 5.56], which seems to be the most adequate [see e.g. 4.204], the interaction of the two close lying A- and B-exciton resonances [5.57] and phenomenological damping constants Γ_A and Γ_B, respectively. The agreement between experiment and theory is quite good (see fig. 65a). We now consider three models for $I_{exc} = 0$:

model 1: The e–h pairs created by I_{exc} influence the parameters $E_{A/B}$, $F_{A/B}$ (oscillator strength), $\Gamma_{A/B}$

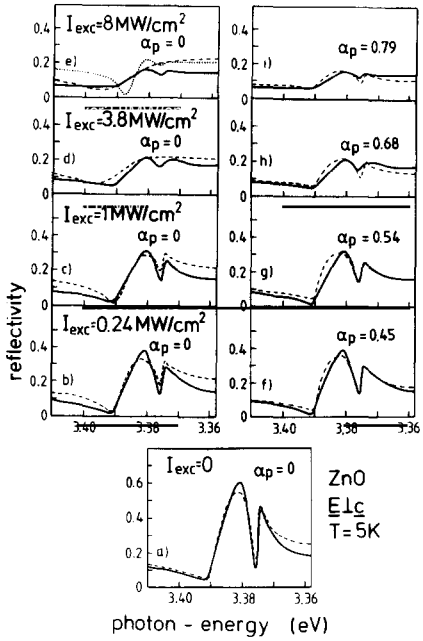

Fig. 65. The measured reflection spectra of the A^{Γ_5} and B^{Γ_5} excitons of ZnO for $T_L = 5$ K (solid lines) as compared to various calculated spectra (dashed and dotted lines). For the different models and the meaning of the parameter α_p see text (from Bohnert et al. [3.8]).

and Δ homogeneously over the excited area. Correspondingly seven parameters may be varied for every spectrum with increasing I_{exc}. Model 1 is thus a refined version of eq. (5.51).

model 2: A top layer on the crystal of adjustable thickness is filled with an EHP, which is described by $\varepsilon = \varepsilon_1 + i\varepsilon_2$ with $\varepsilon_1 = \varepsilon_\infty$ and ε_2 corresponding to an absorption coefficient of $10^5\,\mathrm{cm}^{-1}$, which is a reasonable value for the band-to-band transitions for photon energies $\hbar\omega > \mu(n, T) = \mu_e + \mu_h$. Below this layer, the crystal shows excitonic reflection with the parameters determined for $I_{exc} = 0$.

model 3: The excited area splits in parts, where an EHP exists, described by a frequency independent reflectivity R_p, and in parts with a low-density exciton gas. The reflection of the latter parts is again described with the parameters deduced for $I_{exc} = 0$. The only adjustable parameter is the percentage α_p of the surface which shows "plasmonic" reflection.

The comparison between experiment and the model calculations yields the following results: At low temperatures, model 1 describes the spectra of ZnO only up to $I_{exc} = 1\,\mathrm{M\,W/cm^2}$. For higher I_{exc}, model 1 fails (dashed and dotted lines in fig. 65b–e) as well as model 2. Model 3 is able to reproduce the experimental results up the highest I_{exc} (dashed lines in fig. 65f–i). The values of α_p of model 3 are given in fig. 65f–i. A slight increase of $\Gamma_{A/B}$ to values of about 3 meV leads to a perfect coincidence between experiment and theory.

For CdS, the models 1 and 3 fit the experimental data at 5 K. Model 1, however, only with rather high values of $\Gamma_{A/B}$ up to half the exciton binding energy. Bearing in mind the theoretical predictions of ref. [5.19] such high values of $\Gamma_{A/B}$ seem to be rather unlikely. At higher temperatures, the models 1 and 3 work equally well in ZnO ($T_L = 100$ K) and CdS ($T_L \gtrsim 77$ K)*.

* The spectra of CdS at 100 K do not have enough structures to deduce reliable information.

These results give already some experimental indications for the existence of an EHP. The good agreement with model 3 is not necessarily an indication for a thermodynamic phase-separation, but it could also be a consequence of crystal inhomogenities, which favour in some parts of the crystal the formation of an EHP and suppress it in other regions (e.g. because of fast nonradiative (surface-) recombination channels [5.58]).

As a final remark of the discussion of the reflection spectra it should be noted, that the spectra can also be fitted by decreasing ε_∞ by a factor two, with increasing I_{exc}, combined with a constant F and an increase of Γ. The physical meaning of such a strong decrease of ε_∞ is not yet clear, however (see also subsection 4.4 [4.202]).

Consistently with the results deduced from reflection spectroscopy, one observes that the excitonic absorption structures vanish also with increasing I_{exc}. Thin samples have to be used in these experiments to assure a rather homogeneous excitation. Examples for GaAs and CdS are shown in figs. 66 and 67 taken from refs. [e.g. 5.59 and 5.60], respectively.

It is important to note, that the absorption peaks due to the exciton levels broaden with increasing I_{exc} and finally disappear, but that they do not shift spectrally with I_{exc} within experimental error. This fact is in agreement with what is observed in reflection spectroscopy (fig. 64). Such a behaviour is consistent with theoretical predictions that the variations of E_x^b and of E_g' with the e–h pair density n (i.e.: with I_{exc}) almost compensate each other, leaving the value of E_x nearly unchanged (see subsection 5.1.4, fig. 63).

5.2.2. Gain- and luminescence spectroscopy of the EHP

Reflection and absorption spectroscopy in the exciton region yield some evidence for the existence of an EHP in direct gap semiconductors. A quantitative information about its properties, e.g. the e–h pair density n, the plasma temperature T_p, the position of the reduced gap E_g' etc., cannot be obtained from

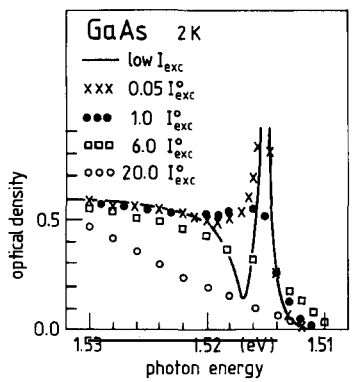

Fig. 66. Optical density of a 0.5 μm thick GaAs sample in the exciton region for various excitation intensities I_{exc} ($I_{exc} \simeq 5 \times 10^2$ W/cm^2). (From Shah et al. [5.59].)

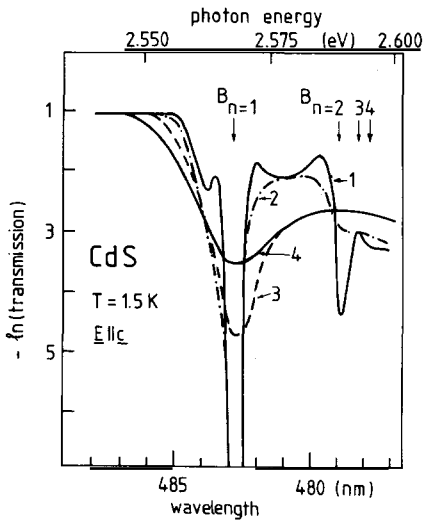

Fig. 67. Transmission spectra of a 0.5 μm thick CdS sample in the B-exciton region for $E \| c$ and $T_{lattice} = 1.5$ K, for various excitation intensities I_{exc}. (1): $I_{exc} = 40$ W/cm^2; (2) $I_{exc} = 8.5$ kW/cm^2; (3) $I_{exc} = 0.7$ MW/cm^2; (4) $I_{exc} = 10$ MW/cm^2 (from Lysenko and Revenko [5.60]).

these experiments. The investigation of the optical gain connected with the e–h pair recombination processes in an EHP gives more detailed informations. The gain values g that have to be expected in the EHP in direct gap materials are of the same order of magnitude as the absorption coefficients due to the band-to-band transitions of the unexcited sample, i.e. $g_{max} \gtrsim 10^3\,cm^{-1}$ or $10^4\,cm^{-1}$ in direct III–V and II–VI compounds, respectively. It is obvious, that a system with such high optical gain cannot be sustained homogeneously in large excited volumes and that the amplification of light runs rapidly into saturation effects, if the amplification path length d is too long. Experimental conditions should be realized, where the product $g_{max} \cdot d$ is smaller than 5 [3.37, 3.38]. This means, that the two beam method using one-photon band-to-band excitation and small excitation spots (see subsection 3.2) is the adequate technique. If the method of varying the excitation strip length is used, an EHP is difficult to be observed, especially if l is varied over several hundreds of micrometers [5.7, 5.61–5.63]. In fact, under these experimental conditions mainly the excitonic processes are detected [e.g. 3.8, 4.10, 4.28, 4.39, 4.58].

Fig. 68 gives a gain spectrum of GaAs obtained with the two beam method by Goebel and Hildebrand [5.2]. The theoretical curve is calculated according to the theory described in subsection 5.1.3 [5.14] and yields the plasma density of $5 \times 10^{16}\,cm^{-3}$ and a plasma temperature $T_p = 10\,K$, which corresponds to $\mu_e - \mu_h - E_g' = 7.36\,meV$. This value has been calculated from $n_j = \Sigma_k f_{k,j}(\mu_j, T)$. Note that the crossover $\varepsilon_2(\omega) = 0$ occurs at $\hbar\omega = \mu_e + \mu_h - E_g' \simeq 7\,meV$. This difference is due to the approximations used in the theory. The resulting parameters are surprisingly close to those obtained from a fit using a simple model for optical transitions without $\boldsymbol{k}$-selection. From this fit Hildebrand and Goebel obtained $n = 4.32 \times 10^{16}\,cm^{-3}$ and $T_p = 10\,K$ [5.2].

Recently, we have shown [5.77] that our theory allows to fit the spectrum given in fig. 68. Also with the same fixed parameters a whole series of spectra which had been obtained by tuning the frequency of the excited laser light has been fitted. Again good agreement is obtained with the results of the no-$\boldsymbol{k}$-selection model if we take the full complex excitonic enhancement $A(\omega)$ into account.

However, in the absorption region, the predictions of the no-$\boldsymbol{k}$-selection rule model deviate strongly from the results of the theory given in subsection 5.1.3 which predicts a peak in the absorption due to the excitonic enhancement (see fig. 57). A comparison between similar lineshape calculations of Arya and Hanke [5.41] which also include the excitonic enhancement but not the collision broadenings, and experimental results of v.d. Linde and Lambrich are shown in fig. 69. While the fit is poor in the region

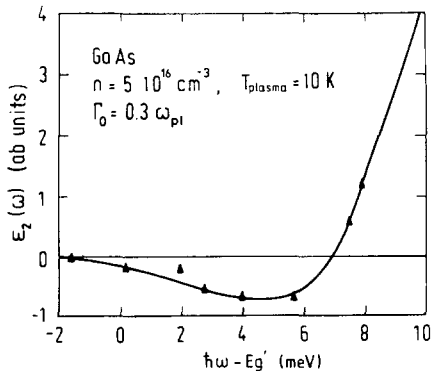

Fig. 68. An experimentally observed gain spectrum (▲) of highly excited GaAs as compared to a calculated gain spectrum (———). The data used in the calculation are $n_p = 5 \times 10^{16}\,cm^{-3}$, $T_p = 10\,K$. (Experimental results from Hildebrand et al. [5.2], theoretical results from Haug and Tran Thoai [5.14].)

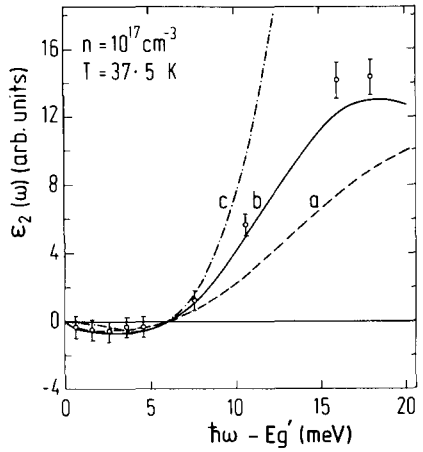

Fig. 69. A transmission spectrum (Φ) of highly excited GaAs showing gain and absorption as compared to different model calculations (experiment from v.d. Linde and Lambrich [5.73]): (a) single-particle transitions with k-selection rule; (b) theory of Arya and Hanke [5.41]; (c) single-particle transitions without k-selection rule.

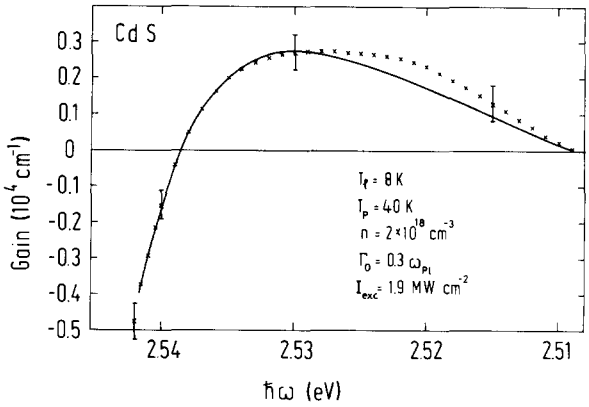

Fig. 70. An experimentally observed gain spectrum (×) of highly excited CdS as compared to a calculated spectrum (———). (Experimental results from Bohnert et al. [3.8], calculation from Schmitt-Rink et al. [5.76].)

of positive gain, the theory is able to explain the change in the absorption due to the presence of the plasma.

InCdS, gain spectra are reported by several authors, from which $n_p = (2\text{–}3) \times 10^{18}\,\text{cm}^{-3}$ and $\mu(n, T) = 2.538\,\text{eV} \pm 3\,\text{meV}$ can be deduced [3.8, 5.1, 5.4, 5.5, 5.63]. Fig. 70 gives an example again together with a theoretical curve according to subsection 5.1.4. Again, the theoretical lineshape fit yields good agreement with the experiment. The small hump on the low energy side is most likely due to some reminiscent excitonic gain (e.g. x–LO or x–x). The parameters deduced from the fit are $n = 2 \times 10^{18}\,\text{cm}^{-3}$ and $T_p = 40\,\text{K}$. They are again in surprisingly good agreement with those deduced from a fit with the no-k-selection rule model, namely $n_p = 2 \times 10^{18}\,\text{cm}^{-3}$, $T_p = 30\,\text{K}$ [3.8]. It is noteworthy, that in CdS also gain spectra have been reported, which are interpreted in terms of an EHP, but which yield a lower plasma density ($n = 4.5 \times 10^{17}\,\text{cm}^{-3}$) and a slightly higher chemical potential $\mu(n, T) = 2.554\,\text{eV}$ [5.6, 3.8].

In all cases reported so far, $\mu(n, T)$ and n are almost constant, if I_{exc} is varied over more than a decade [3.8, 5.1–5.7, 5.61–5.63]. The values for the chemical potentials given above for GaAs and CdS have been confirmed by excitation spectroscopy, since one observes a steep decrease of the excitation spectrum of an EHP, if one passes from $\hbar\omega_{exc} > \mu(n, T)$ to $\hbar\omega_{exc} > \mu(n, T)$ [1.1, 5.7]. Fig. 71 gives an example for GaAs. The values deduced for $\mu(n, T)$ from the excitation spectroscopy are 1.512 eV for GaAs [5.7] and $2.540\,\text{eV} \pm 2\,\text{meV}$ for CdS [1.1].

In other direct III–V compounds (InP, GaSb), there are similar experimental results as in GaAs concerning the EHP [5.7]. In ZnO gain spectroscopy indicates an EHP with $\mu(n, T) = 3.355\,\text{eV} \pm 5\,\text{meV}$ i.e. $E_x - \mu(n, T) \simeq 20\,\text{meV}$ and $n \simeq 5 \times 10^{18}\,\text{cm}^{-3}$ [3.8, 5.62]. The shape of the gain spectra sometimes seems to be a superposition of plasma contributions with different n but almost constant μ [3.8]. Some indications for an EHP in ZnSe [5.64], ZnTe [5.65] and CdTe [5.66] have been deduced from luminescence spectra. It should be noted however, that simple luminescence measurements under band-to-band excitation with a N_2-laser generally cannot give conclusive results concerning the existence of an EHP [e.g. 4.37].

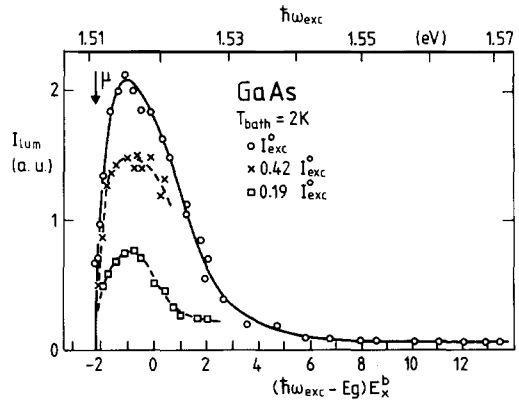

Fig. 71. The excitation spectra of the electron–hole plasma emission of GaAs for different excitation intensities I_{exc}. Points: experiment; solid lines and dashed line: calculated curves (from Hildebrand et al. [5.7]).

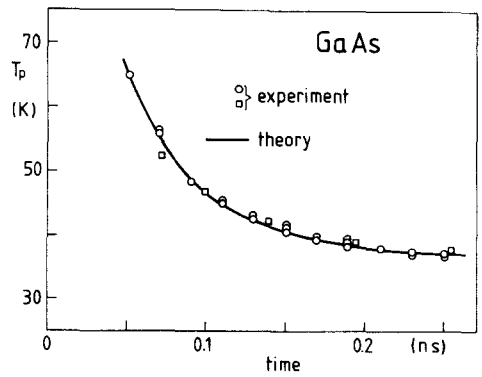

Fig. 72. The temporal evolution of the plasma temperature T_p of an electron–hole plasma in GaAs after picosecond excitation. The sample is excited by two-photon absorption from a mode-locked Nd-laser. The duration of the laser pulse is 25 ps (from v.d. Linde and Lambrich [5.73]).

In [5.67–5.70] an emission band in CdS and CdSe has been observed in luminescence- and gain spectroscopy under ns- and ps- excitation which is sometimes called Q-band. Though it is situated at considerably lower photon energies with respect to E_g than the emission structures described above, it is attributed to an EHP, too. Since it develops from the E_x–LO emission, an alternative interpretation would be to ascribe it to some LO-phonon satellite of a higher energy process. Temperature effects may also play an important role [5.6].

Relaxation processes of carriers in an EHP after ps excitation have been investigated by an excitation and probe beam technique in GaAs and other materials [5.71–72]. The energy-loss-rate of the carriers in the bands has been found to be about 0.4 eV/ps [5.71].

In [5.73], the temporal evolution of the plasma temperature in GaAs has been determined from the variation of the EHP lineshape. Fig. 72 gives an example. The solid line is a theoretical curve taking into account the cooling of the EHP by LO–phonon emission. For temperatures below 40 K this process becomes ineffective and a cooling via acoustic phonon emission has a much longer time constant, at least in materials without strong piezo-coupling. The lifetime of the EHP itself depends strongly on the experimental conditions. Stimulation effects play an important role. Data given in the literature are ranging from about 100 to 500 ps (see e.g. [1.58, 5.71, 5.73]).

5.3. Open questions concerning the EHP in direct gap materials

We limit our discussion mainly to GaAs as a representative of the III–V compounds and to CdS as a typical II–VI semiconductor. First, we compare the values of n_0 and φ deduced from the experiments with the theoretical predictions (see table 6 in subsection 5.1.2). The comparison shows, that the theoretical values tend to underestimate the binding energy of the EHP, even if the polaron corrections which tend to stabilize the plasma are included [e.g. 5.7, 5.20]. The values of the theoretical equilibrium densities are generally of the same order as those deduced from the experiment.

The fact, that the chemical potentials $\mu(n, T)$ and n are rather independent on I_{exc} in GaAs and CdS is regarded by several authors as an indication, that the EHP is in a liquid state (EHL). There are however several experimental findings, which strongly contradict this interpretation: In GaAs and other

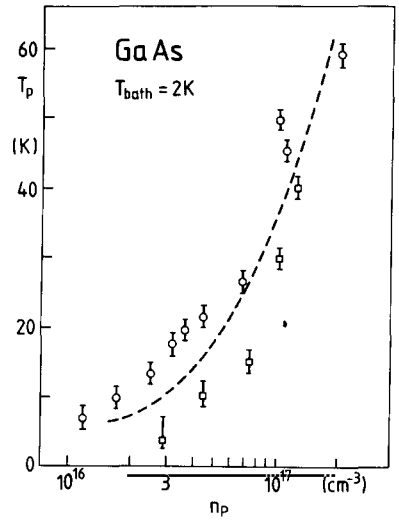

Fig. 73. The density of an electron–hole plasma in GaAs as a function of the plasma temperature T_p ($\frac{\diamond}{\diamond}$ = strip-length method, $\frac{\diamond}{\diamond}$ = two beam method). The dashed lines gives some average between the results of the two different techniques (from Hildebrand et al. [5.7]).

III–V compounds one has found [5.7], that the plasma density increases linearly with increasing temperature T_p and depends on the experimental technique, see fig. 73. Both facts are in contradiction to all calculated phase diagrams for an EHL, known so far (see e.g. subsection 5.1.2 and fig. 52). In CdS, different plasma densities are observed in different samples which are, however, rather independent of I_{exc}. In the low density case, n also increases with T_p from 4.5×10^{17} cm^{-3} at $T_p \simeq 30$ K to 8.2×10^{17} cm^{-3} at $T_p \simeq 60$ K [3.8]. For the high density case unfortunately, no reliable investigations of the temperature variation have been performed so far*.

In GaAs [5.7], where the critical temperature T_c for an EHL formation is rather low ($T_c \simeq 10$ K), the above mentioned experimental results are explained by assuming, that n is determined by the Mott density n_M, which in fact increases linearly with T_p if Debye–Hückel screening is assumed. The values of the Mott density n_M, however, are more than a factor of ten higher than the theoretical expected values. Therefore, an alternative model has been put forward tentatively in ref. [3.8]:

The e–h pairs, created by the excitation in a very thin layer (penetration depth of the exciting light $w = K_1^{-1} \simeq 0.1$ μm in CdS) are driven into the sample by e.g. the enormous gradient in the chemical potential μ (grad $\mu \geq 10^6$ eV/m) or by the phonon wind. In this expanded gas of free and bound e–h pairs, the condensation to the equilibrium density sets in. Since the ground state energy $E_g^0(n)$ and – at low T_p – also the chemical potential are only slightly varying functions of n_p for n_p smaller than the equilibrium density n_0 (in contrast to $n > n_0$) the e–h pairs often do not reach thermal equilibrium during their rather short lifetime. The degree to which thermal equilibrium is reached, depends on the experimental conditions and on the individual sample under investigation.

Therefore, it is understandable that in different samples different values of n are observed. Spectra are reported (e.g. for ZnO [3.8]) which can be fitted only by assuming a spatial or temporal superposition of contributions with different plasma densities. Especially favourable conditions for obtaining thermal equilibrium are given, if very thin samples are used ($\lesssim 1$ μm thick), where the initial

* The spectra reported in [5.75] show significant structures due to excitonic recombination processes. The results seem therefore not to be conclusive for an EHP.

expansion of the e–h pair gas is partly suppressed by the crystal dimensions. Under such conditions, $g(\hbar\omega)$ has been determined for CdS in [5.5] from the variation of the interference fringes in transmission and reflection. The value deduced for the chemical potential of 2.535 eV is therefore assumed to be rather close to the equilibrium value.

In conclusion it can be stated, that many experimental findings give evidence for the formation of an EHP in direct materials under high excitation. In order to get a more detailed understanding of the EHP, one has to use in the theory a dynamical nonequilibrium treatment in order to explain high excitation experiments in direct gap semiconductors. First attempts in this direction have been described in subsection 5.1.4. This theory predicts that the "coexistence" region has quite different properties in direct and indirect materials. In indirect materials one has a coexistence region (in analogy to a classical gas–liquid phase diagram) consisting of e–h droplets in an exciton gas. For direct gap semiconductors we expect between the exciton gas phase and the homogeneous liquid phase a region in which one has e–h clusters with a broad distribution of sizes. The formation and properties of these e–h clusters have not yet been investigated experimentally.

Therefore, further research work is necessary to understand the intermediate density region, where the transition from a dense exciton system to a plasma occurs. Theoretically, one has to develop a description which contains both the bound states and the continuum of e–h pairs in order to understand the Mott transition and to derive an equation of state for the total density range. It would be highly desirable if one could develop methods which allow a reliable experimental determination of the density of free carriers and excitons at a given excitation intensity. Further experimental work on the phase diagram is necessary especially on the low-density side and in the critical region. Up to now, there is for instance no experimental investigation of the enhanced scattering in the critical region which would correspond to the critical opalescence, a phenomenon which is studied extensively for classical gas–liquid phase transitions. We believe that a thorough understanding of all these effects can, especially for direct gap semiconductors, only be reached if the low-temperature phase transition to a degenerate EHP is described and analysed as a nonequilibrium phase transition.

Acknowledgements

This work has been funded by the Deutsche Forschungsgemeinschaft, the theoretical part of it is a project of the Sonderforschungsbereich Frankfurt/Darmstadt. Our coworkers D.B. Tran Thoai, S.W. Koch, S. Schmitt-Rink, K. Bohnert, G. Schmieder, H. Schrey, W. Maier, K. Wünstel and V.G. Lyssenko have contributed significantly to the reported work. Stimulating discussions with B. Hönerlage, J.B. Grun and many other colleagues are gratefully acknowledged.

References

[1.1] H. Schrey and C. Klingshirn, Phys. Stat. Sol. b 90 (1978) 67.
[1.2] For a recent review of the properties of bound excitons, see e.g. P.J. Dean and D.C. Herbert, in: Topics in Current Physics, Vol. 14, ed. K. Cho (Springer, 1979) p. 55.
[1.3] Ya. Pokrovskii, Phys. Stat. Sol. a 11 (1972) 385.
[1.4] C.D. Jeffries, Science 189 (1975) 955.
[1.5] T.M. Rice, Solid State Physics, Vol. 32 (Academic Press, 1977) p. 1.
[1.6] J.C. Hensel, T.G. Philips and G.A. Thomas, ibid p. 88.
[1.7] Ya. Pokrovskii and V.B. Timofeev, Sov. Scient. Rev. A, Phys. Rev. 1 (1979) 191.
[1.8] D. Hulin, M. Combescot, N. Bontemps and A. Mysyrowicz, Phys. Lett. 61A (1977) 349.

[1.9] R. Schwabe, F. Thuselt, H. Weinert, R. Bindemann and K. Unger, Phys. Stat. Sol. b 89 (1978) 561.
[1.10] H. Maaref, J. Barrau, M. Brousseau, J. Collet, J. Mazzaschi and M. Pugnet, Phys. Stat. Sol. b 88 (1978) 261.
[1.11] D. Bimberg, M.S. Skolnick and L.M. Sander, Phys. Rev. B 19 (1979) 2231.
[1.12] A. Haug, Sol. State Comm. 25 (1978) 477 and J. Luminescence 20 (1979) 173.
[1.13] J. Bille, Advances in Solid State Physics, Vol. XIII (1973) p. 111.
[1.14] H. Büttner, ibid p. 145.
[1.15] M.H. Pilkuhn, J. Luminescence 7 (1973) 269.
[1.16] E. Göbel and M.H. Pilkuhn, Jour. de Phys. 35 (1974) C 3–191.
[1.17] R. Levy and J.B. Grun, Phys. Stat. Sol. a 22 (1974) 11.
[1.18] Excitons at High Densities, eds. H. Haken and S. Nikitine, Springer Tracts in Modern Physics 73 (1975).
[1.19] Proc. Oji Seminar on the Physics of Highly Excited States in Solids, Japan 1976, eds. Y. Nishina and M. Ueta, Lecture Notes in Physics Vol. 57 (Springer, Berlin, 1976).
[1.20] E. Hanamura, in: Optical Properties of Solids, New Developments, ed. B.O. Seraphin (North-Holland, Amsterdam, 1976) p. 81.
[1.21] M. Voos and C. Benoît à la Guillaume, ibid p. 143.
[1.22] E. Hanamura and H. Haug, Physics Reports 33C (1977) 209.
[1.23] R. Luzzi and L.C.M. Miranda, Physics Reports 43C (1977) 423.
[1.24] E. Göbel and G. Mahler, Advances in Solid State Physics XIX (1979) 105.
[1.25] J.B. Grun, B. Hönerlage and R. Lévy, Modern Problems in Solid State Physics, eds. A.A. Maradudin and V.M. Agranovich (North-Holland, Amsterdam, 1980).
[1.26] Proc. Intern. Conf. on the Physics of Semiconductors:
9th Conf., Moscow (1968);
10th Conf., Cambridge (1970);
11th Conf., Warsaw (1972);
12th Conf., Stuttgart (1974);
13th Conf., Rome (1976);
14th Conf., Edinburgh (1978);
15th Conf., Kyoto (1980).
[1.27] Proc. Intern. Conf. on Luminescence:
Tokyo (1975), J. Luminescence 12/13;
Paris (1978), J. Luminescence 18/19.
[1.28] Taormina Research Conf. on Recent Developments in Optical Spectroscopy of Solids (1976), published in Il Nuovo Cimento B39 (1977).
[1.29] R.S. Knox, Solid State Physics, Supplement 5 (Academic Press, 1963).
[1.30] J.O. Dimmock, Semiconductors and Semimetals, Vol. III (Academic Press, 1967) p. 259.
[1.31] M.A. Lampert, Phys. Rev. Lett. 1 (1958) 450.
[1.32] S.A. Moskalenko, Optics and Spectroscopy 5 (1958) 147.
[1.33] D.G. Thomas and J.J. Hopfield, J. Appl. Physics 33 (1962) 3243.
[1.34] C.E. Hurwitz, Appl. Phys. Lett. 9 (1966) 420.
[1.35] V.K. Konjukhov, L.A. Kulevskii and A.M. Prokhorov, Sov. Phys.-Doklady 10 (1966) 943.
[1.36] F.H. Nicoll, Appl. Phys. Lett. 10 (1967) 69 and J. Appl. Phys. 42 (1971) 2743.
[1.37] J.R. Packard, W.C. Tait and D.A. Campbell, IEEE J. Quant. Electr. QE5 (1969) 44.
[1.38] D. Magde and H. Mahr, Phys. Rev. Lett. 24 (1970) 890.
[1.39] D.L. Keune, N. Holonyak Jr., P.D. Dapkus and R.D. Burnham, Appl. Phys. Lett. 17 (1970) 42.
[1.40] J.M. Hvam, Phys. Rev. B 4 (1971) 4459.
[1.41] B.K. Garside, J. Shewchun and B.S. Kawasaki, IEEE J. Quant. Electr. QE 7 (1971) 88.
[1.42] K. Era and D.W. Langer, J. Appl. Phys. 42 (1971) 1021.
[1.43] R.N. Hall, Solid State Electronics 6 (1963) 405.
[1.44] G. Lasher and F. Stern, Phys. Rev. 133 (1964) A 553.
[1.45] L.V. Keldysh, Proc. 9th Intern. Conf. Phys. on Semiconductors (Moscow, 1968) p. 1303.
[1.46] J.R. Haynes, Phys. Rev. Lett. 17 (1966) 860.
[1.47] C. Benoît à la Guillaume and O. Parodi, J. Electr. Control 6 (1959) 356.
[1.48] A. Mysyrowicz, J.B. Grun, R. Levy, A. Bivas and S. Nikitine, Phys. Lett. 26 A (1968) 615.
[1.49] V.M. Asnin and A.A. Rogachev, JETP Lett. 7 (1968) 360; 9 (1969) 248.
[1.50] V.S. Vavilov, V.A. Zayats and V.N. Murzin, JETP Lett. 10 (1969) 192.
[1.51] V.S. Bagaev, T.I. Galkina, O.V. Gogolin and L.V. Keldysh, JETP Lett. 10 (1969) 195.
[1.52] A.S. Kaminskii, Y.E. Pokrovskii and N.V. Alkeev, Sov. Phys.-JETP 32 (1971) 1048.
[1.53] Y.E. Pokrovskii and K.I. Svistunova, JETP Lett. 13 (1971) 212.
[1.54] C. Benoît à la Guillaume, M. Voos, F. Salvan, J.-M. Laurant and A. Bonnot, C.R. Acad. Sci. 272 (1971) 236.
[1.55] D. Magde and H. Mahr. Phys. Rev. B 2 (1970) 4098.
[1.56] R.S. Knox, S. Nikitine and A. Mysyrowicz, Opt. Comm. 1 (1969) 19.

[1.57] R. Lévy and J.B. Grun, J. Luminescence 5 (1972) 406.
[1.58] D.v.d. Linde, Advances in Solid State Physics XIX (1979) 387.
[2.1] O. Madelung, Physics of III–V Compounds (Wiley and Sons, 1964).
[2.2] A. Goldmann, Phys. Stat. Sol. b 81 (1977) 9 and the literature cited therein.
[2.3] J.O. Dimmock, in: II–VI Semiconducting Compounds, Intern. Conf. 1967, ed. D.G. Thomas (W.A. Benjamin, 1967) p. 277.
[2.4] U. Roessler, Phys. Rev. 184 (1969) 733.
[2.5] A. Baldereschi and K. Maschke, Proc. 14th Intern. Conf. on Phys. Semiconductors, Edinburgh (1978), ed. B.L.H. Wilson, p. 1167.
[2.6] M. Cardona, Phys. Rev. B 129 (1963) 69.
[2.7] G. Dresselhaus, Phys. Rev. 100 (1955) 580;
J.M. Luttinger, Phys. Rev. 102 (1956) 1030;
E.O. Kane, Phys. Rev. B 11 (1975) 3850;
S. Suga, K. Cho and M. Bettini, Phys. Rev. B 13 (1976) 943.
[2.8] K. Hümmer, Phys. Stat. Sol. b 56 (1973) 249.
[2.9] F. Bassani, G. Pastori Parravicini and R.A. Ballinger, Electronic States and Optical Transitions in Solids, (Pergamon Press, Oxford, 1975).
[2.10] A.L. Vetter and D. Walecka, Quantum Theory of Many Particle Systems (McGraw-Hill, New York, 1971).
[2.11] J.J. Hopfield, Phys. Rev. 112 (1958) 1555.
[2.12] E. Ostertag, Thesis, Univ. Strasbourg (1977).
[2.13] U. Roessler, Advances in Solid State Physics XIX (1979) 77.
[2.14] K. Cho, Topics in Current Physics Vol. 14 (Springer, 1979) p. 1 and p. 15.
[2.15] For a recent review see K. Hümmer, Habilitation Thesis, Univ. Erlangen (1978).
[2.16] O. Akimoto and E. Hanamura, J. Phys. Soc. Japan 33 (1972) 1537 and Sol. State Comm. 10 (1972) 253.
[2.17] W.F. Brinkman, T.M. Rice and B. Bell, Phys. Rev. B 8 (1972) 1570.
[2.18] W.T. Huang, Phys. Stat. Sol. b 60 (1973) 309.
[2.19] J. Adamowski, S. Bednarek and M. Suffczynski, Sol. State Comm. 9 (1971) 2037 and Phil. Mag. 26 (1972) 143.
[2.20] A.I. Bobrysheva and V.I. Vybornov, Phys. Stat. Sol. b 88 (1978) 315.
[2.21] J. Adamowski, S. Bednarek and M. Suffczynski, Sol. State Comm. 20 (1976) 785 and 25 (1978) 89.
[2.22] D.B. Tran Thoai, Z. Physik B 26 (1976) 115.
[2.23] D. Pines, Elementary Excitations in Solids (W.A. Benjamin, New York, 1963).
[2.24] R.N. Silver and C.H. Alderich, Phys. Rev. Lett. 41 (1979) 1249.
[2.25] B.I. Lundquist, Phys. Kond. Materie 6 (1967) 193 and 206.
[2.26] R. Zimmermann, Phys. Stat. Sol. b 76 (1976) 191.
[2.27] T.M. Rice, Il Nuovo Cimento 23 B (1974) 226.
[2.28] O. Madelung, Introduction to Solid State Theory (Springer, 1978).
[2.29] Y. Toyozawa, Suppl. Prog. Theor. Phys. 12 (1959) 111.
[3.1] P. Wiesner and U. Heim, Phys. Rev. B 11 (1975) 3071.
[3.2] G. Kobbe and C. Klingshirn, Z. Physik B 37 (1980) 9.
[3.3] V.G. Lyssenko and V.I. Revenko, Sov. Phys. Sol. Stat. 20 (1978) 1238.
[3.4] W.D. Johnston Jr., J. Appl. Phys. 42 (1971) 2731.
[3.5] J. Bille, B.M. Kramer and W. Ruppel, Phys. Stat. Sol. a 4 (1971) 731.
[3.6] K.L. Shaklee, R.F. Nahory and R.F. Leheny, J. Luminescence 7 (1973) 284.
[3.7] J.M. Hvam, J. Appl. Phys. 49 (1978) 3124.
[3.8] K. Bohnert, G. Schmieder and C. Klingshirn, Phys. Stat. Sol. b 98 (1980) 175.
[3.9] E. Ostertag and J.B. Grun, Phys. Stat. Sol. b 82 (1977) 335.
[3.10] E. Ostertag, Rev. Sci. Instrum. 48 (1977) 18.
[3.11] M. Ojima, T. Kushida, Y. Tanaka and S. Shionoya, Sol. State Comm. 20 (1976) 847 and 24 (1977) 837 and 841.
[3.12] M. Hayashi, H. Saito and S. Shionoya, Sol. State Comm. 24 (1977) 833.
[3.13] T. Daly and H. Mahr, Sol. State Comm. 25 (1978) 323 and the literature cited therein.
[3.14] R. Lévy, B. Hönerlage and J.B. Grun, Phys. Rev. B 19 (1979) 2326.
[3.15] Topics in Applied Physics, Vol. 18 (Springer Verlag, Berlin, 1977).
[4.1] C. Benoît à la Guillaume, J.M. Debever and F. Salvan, Proc. 9th Intern. Conf. on Phys. Semiconductors, Moscow (1968) p. 581 and Phys. Rev. 177 (1969) 567.
[4.2] H. Haug, J. Appl. Phys. 39 (1968) 4687.
[4.3] C.I. Yu, T. Goto and M. Ueta, J. Phys. Soc. Japan 34 (1973) 693.
[4.4] T. Fischer and J. Bille, J. Appl. Phys. 45 (1974) 3937.
[4.5] G.Y. Buryakovskii, V.S. Mashkevich and Z.I. Uritskii, Sov. Phys. Sol. Stat. 16 (1974) 584.
[4.6] G.Y. Buryakovskii and V.S. Mashkevich, Sov. Phys. Semicond. 8 (1974) 1313.
[4.7] T. Moriya and T. Kushida, J. Phys. Soc. Japan 40 (1976) 1668 and 1676.
[4.8] B. Hönerlage, C. Klingshirn and J.B. Grun, Phys. Stat. Sol. b 78 (1976) 599.
[4.9] H. Haug and S.W. Koch, Phys. Stat. Sol. b 82 (1977) 531.

[4.10] S.W. Koch, H. Haug, G. Schmieder, W. Bohnert and C. Klingshirn, Phys. Stat. Sol. b 89 (1978) 431.
[4.11] S. Shionoya, H. Saito, E. Hanamura and O. Akimoto, Sol. State Comm. 12 (1973) 223.
[4.12] K. Cho, Optics Comm. 8 (1973) 412.
[4.13] A.A. Gogolin and E.I. Rashba, JETP-Lett. 17 (1973) 478.
[4.14] A.A. Gogolin, Sov. Phys. Sol. Stat. 15 (1974) 1824.
[4.15] E. Ostertag, R. Lévy and J.B. Grun, Phys. Stat. Sol. b 69 (1975) 629.
[4.16] K.G. Petrashku and P.I. Khadzhi, Sov. Phys. Semicond. 9 (1975) 734.
[4.17] F. Henneberger and J. Voigt, Phys. Stat. Sol. b 76 (1976) 313.
[4.18] H.-J. Wünsche and F. Henneberger, Phys. Stat. Sol. b 76 (1976) 639.
[4.19] R. Planel and C. Benoît à la Guillaume, Phys. Rev. B 15 (1977) 1192.
[4.20] F. Henneberger, K. Henneberger and J. Voigt, Phys. Stat. Sol. b 79 (1977) K 81.
[4.21] S.W. Koch, private communication.
[4.22] B. Freienstein, Diploma-thesis, Univ. Frankfurt (1978).
[4.23] N. Nagasawa, N. Nakata, Y. Doi and M. Ueta, J. Phys. Soc. Japan 38 (1975) 593 and 39 (1975) 987.
[4.24] C. Klingshirn, Sol. State Comm. 13 (1973) 297.
[4.25] C. Klingshirn, Phys. Stat. Sol. b 71 (1975) 547.
[4.26] K. Wünstel and C. Klingshirn, Optics Comm. 32 (1980) 269.
[4.27] W.D. Johnston Jr., J. Appl. Phys. 42 (1971) 2731.
[4.28] R. Baumert, E. Beckmann and I. Broser, Proc. 14th Intern. Conf. on Phys. Semiconductors, Edinburgh (1978) p. 161.
[4.29] S. Iwai and S. Namba, Appl. Phys. Lett. 16 (1970) 354.
[4.30] J.M. Hvam, Proc. 10th Intern. Conf. on Phys. Semicond., Boston (1970) p. 71 and Phys. Rev. B 4 (1971) 4459.
[4.31] J. Bille, B.M. Kramer, P. Reimers, W. Ruppel and R. Stille, Phys. Stat. Sol. 36 (1969) K 71.
[4.32] J. Bille, H. Liebing, P. Mengel and G. Scheiber, Phys. Stat. Sol. a 12 (1972) K 91.
[4.33] G. Huber, J. Bille, W. Braun and T. Fischer, Phys. Stat. Sol. a 18 (1973) 489.
[4.34] M.S. Brodin, V.P. Krashenko and S.G. Shevel, Sov. Phys. Semicond. 8 (1974) 439.
[4.35] R.L. Herbst and R.L. Byer, Appl. Phys. Lett. 19 (1971) 527.
[4.36] W. Maier and C. Klingshirn, Sol. State Comm. 28 (1978) 13.
[4.37] C. Klingshirn, W. Maier, B. Hönerlage, H. Haug and S.W. Koch, Solid State Electronics 21 (1978) 1357.
[4.38] G. Kurtze, C. Klingshirn, B. Hönerlage, E. Tomzig and H. Scholz, J. Luminescence 20 (1979) 151.
[4.39] J.M. Hvam, J. Luminescence 18/19 (1979) 312 and Sol. State Comm. 26 (1978) 373 and 987.
[4.40] D. Magde and H. Mahr, Phys. Rev. Lett. 24 (1970) 890.
[4.41] J.M. Hvam, Sol. State Comm. 12 (1973) 95 and Phys. Stat. Sol. b 63 (1974) 511.
[4.42] H. Liebing, P. Mengel and W. Ruppel, Phys. Stat. Sol. b 72 (1975) 431.
[4.43] A. Opanowicz, K. Marinova, H. Liebing and W. Ruppel, Phys. Stat. Sol. b 75 (1976) 471.
[4.44] A. Opanowicz and K. Marinova, Phys. Stat. Sol. b 77 (1976) K 35.
[4.45] M. Itoh, Y. Nozue, T. Itoh, M. Ueta, S. Satoh and K. Igaki, J. Luminescence 18/19 (1979) 568.
[4.46] E. Göbel, H. Herzog, M.H. Pilkuhn and K.-H. Zschauer, Sol. State Comm. 13 (1973) 719.
[4.47] E. Göbel, K.L. Shaklee and R. Epworth, Sol. State Comm. 17 (1975) 1185.
[4.48] T. Moriya and T. Kushida, J. Phys. Soc. Japan 41 (1976) 849 and the literature cited therein.
[4.49] C.I. Yu, T. Goto and M. Ueta, J. Phys. Soc. Japan 32 (1972) 1671.
[4.50] J.F. Figueira and H. Mahr, Sol. State Comm. 9 (1971) 679.
[4.51] M. Kuroda and S. Shionoya, Sol. State Comm. 13 (1973) 1195 and J. Phys. Soc. Japan 36 (1974) 476.
[4.52] V.L. Broude, Proc. 12th Europ. Congr. on Molec. Spectr., Strasbourg (1975) p. 159 and
V.L. Broude, V.V. Korshunov, I.I. Tartakovskii and V.B. Timofeev, Sov. Phys. Sol. Stat. 17 (1975) 1139.
[4.53] M. Hayashi, H. Saito and S. Shionoya, Sol. State Comm. 24 (1977) 833.
[4.54] M. Hayashi, H. Saito and S. Shionoya, J. Phys. Soc. Japan 44 (1978) 582.
[4.55] G.A. Boiko, V.S. Dneprovskii, M.V. Kraevskii, K. Marinova, S.M. Oak, E.K. Silina and V.S. Fokin, Phys. Stat. Sol. b 85 (1978) 111.
[4.56] T. Kabayashi, Y. Segawa and S. Namba, Sol. State Comm. 31 (1979) 253.
[4.57] H. Büttner, Phys. Stat. Sol. 42 (1970) 775.
[4.58] R. Baumert, E. Beckmann, I. Broser, R. Broser and R. Renz, J. Luminescence 18/19 (1979) 558.
[4.59] K. Bohnert, G. Schmieder and C. Klingshirn, Phys. Stat. Sol. b 98 (1980) 175.
[4.60] C. Klingshirn, E. Ostertag and R. Lévy, Sol. State Comm. 15 (1974) 883.
[4.61] C. Klingshirn, J.B. Grun, E. Ostertag and R. Lévy, Proc. 12 Europ. Congr. on Molec. Spectr., Strasbourg (1975) p. 101.
[4.62] B. Hönerlage and U. Roessler, ibid p. 105 and J. Luminescence 12/13 (1976) 593.
[4.63] C. Klingshirn, R. Lévy, J.B. Grun and B. Hönerlage, Sol. State Comm. 20 (1976) 413.
[4.64] T. Goto and D.W. Langer, J. Appl. Phys. 42 (1971) 5066.
[4.65] A.F. Dite, V.I. Revenko, V.B. Timofeev and P.D. Altukhov, Sov. Phys.-JETP Lett. 18 (1973) 341.
[4.66] H. Schrey and C. Klingshirn, Phys. Stat. Sol. b 93 (1979) 679.
[4.67] S. Nikitine, A. Mysyrowicz and J.B. Grun, Helvetica Physica Acta 41 (1968) 1058.

[4.68] J.B. Grun, S. Nikitine, A. Bivas and R. Lévy, J. Luminescence 1/2 (1970) 241.
[4.69] R.S. Knox, S. Nikitine and A. Mysyrowicz, Optics Comm. 1 (1969) 19.
[4.70] A. Bivas, R. Lévy, S. Nikitine and J.B. Grun, J. de Physique 31 (1970) 227.
[4.71] H. Souma, T. Goto, T. Ohta and M. Ueta, J. Phys. Soc. Japan 29 (1970) 697.
[4.72] R. Lévy, A. Bivas and J.B. Grun, Phys. Lett. 36A (1971) 159.
[4.73] H. Souma, H. Koike, K. Suzuki and M. Ueta, J. Phys. Soc. Japan 31 (1971) 1285.
[4.74] H. Souma, K. Suzuki and M. Ueta, J. Phys. Soc. Japan 30 (1971) 589.
[4.75] K.L. Shaklee, R.F. Leheny and R.E. Nahory, Phys. Rev. Lett. 26 (1971) 888.
[4.76] G.M. Gale and A. Mysyrowicz, Phys. Rev. Lett. 32 (1974) 727.
[4.77] J.B. Grun, C. Comte, R. Lévy and E. Ostertag, J. Luminescence 12/13 (1976) 581.
[4.78] R. Lévy, A. Bivas, C. Comte and E. Ostertag, Proc. 12th Europ. Congr. Molec. Spectrosc., Strasbourg (1975) p. 97.
[4.79] E. Ostertag, R. Lévy and J.B. Grun, Phys. Stat. Sol. b 69 (1975) 629.
[4.80] N. Nakata, N. Nagasawa, Y. Doi and M. Ueta, J. Phys. Soc. Japan 38 (1975) 593 and 903.
[4.81] N. Nagasawa, N. Nakata, Y. Doi and M. Ueta, J. Phys. Soc. Japan 39 (1975) 987.
[4.82] G.M. Gale and A. Mysyrowicz, Phys. Lett. 54A (1975) 321.
[4.83] R. Lévy, C. Klingshirn, E. Ostertag, Vu Duy Phach and J.B. Grun, Phys. State. Sol. b 77 (1976) 381 and
E. Ostertag, C. Klingshirn, Vu Duy Phach and J.B. Grun, Proc. 13th Int. Conf. Phys. Semiconductors, Rome (1976) p. 922.
[4.84] N. Nagasawa, T. Mita and M. Ueta, J. Phys. Soc. Japan 41 (1976) 929.
[4.85] N. Nagasawa, S. Koizumi, T. Mita and M. Ueta, J. Luminescence 12/13 (1976) 587.
[4.86] Y. Nasu, S. Koizumi, N. Nagasawa and M. Ueta, J. Phys. Soc. Japan 41 (1976) 715.
[4.87] M. Ojima, T. Kushida, Y. Tanaka and S. Shionoya, Sol. State Comm. 20 (1976) 847.
[4.88] R.W. Svorec and L.L. Chase, Sol. State Comm. 20 (1976) 353.
[4.89] E. Ostertag and J.B. Grun, Phys. Stat. Sol. b 82 (1977) 335.
[4.90] J.B. Grun, Il Nuovo Cimento 39 B (1977) 579.
[4.91] E. Ostertag, A. Bivas and J.B. Grun, Phys. Stat. Sol. b 84 (1977) 673.
[4.92] A. Bivas, Vu Duy Phach, B. Hönerlage and J.B. Grun, Phys. Stat. Sol. b 84 (1977) 235.
[4.93] E. Ostertag and J.B. Grun, Appl. Phys. Lett. 31 (1977) 509.
[4.94] Vu Duy Phach, A. Bivas, B. Hönerlage and J.B. Grun, Phys. Stat. Sol. b 84 (1977) 731.
[4.95] B. Hönerlage, Vu Duy Phach, A. Bivas and E. Ostertag, Phys. Stat. Sol. b 83 (1977) K 101.
[4.96] M. Ojima, Y. Oka, T. Kushida and S. Shionoya, Sol. State Comm. 24 (1977) 845.
[4.97] M. Ojima, T. Kushida, Y. Tanaka and S. Shionoya, Sol. State Comm. 24 (1977) 841.
[4.98] N. Nagasawa, T. Mita, T. Itoh and M. Ueta, J. Phys. Soc. Japan 43 (1977) 1295.
[4.99] B. Hönerlage, A. Bivas and Vu Duy Phach, Phys. Rev. Lett. 41 (1978) 49.
[4.100] Vu Duy Phach, A. Bivas, B. Hönerlage and J.B. Grun, Phys. Stat. Sol. b 86 (1978) 159.
[4.101] B. Hönerlage, Vu Duy Phach and J.B. Grun, Phys. Stat. Sol. b 88 (1978) 545.
[4.102] A. Bivas, R. Lévy, Vu Duy Phach and J.B. Grun, Proc. 14th Intern. Conf. on the Phys. of Semiconductors, Edinburgh, 1978, p. 497.
[4.103] M. Ojima, T. Kushida, Y. Tanaka and S. Shionoya, J. Phys. Soc. Japan 44 (1978) 1294.
[4.104] A. Maruani, J.L. Oudar, E. Batifol and D.S. Chemla, Phys. Rev. Lett. 41 (1978) 1372.
[4.105] T. Itoh and T. Suzuki, J. Phys. Soc. Japan 45 (1978) 1939.
[4.106] T. Itoh, T. Suzuki and M. ueta, J. Phys. Soc. Japan 44 (1978) 345.
[4.107] T. Suzuki, T. Itoh and M. Ueta, J. Phys. Soc. Japan 44 (1978) 347.
[4.108] T. Mita and M. Ueta, Sol. State Comm. 27 (1978) 1463.
[4.109] Y. Segawa, Y. Aoyagi, O. Nakagawa, K. Azuma and S. Namba, Sol. State Comm. 27 (1978) 785.
[4.110] Y. Masumoto, S. Shionoya and Y. Tanaka, Sol. State Comm. 27 (1978) 1117.
[4.111] M. Ojima, T. Kushida, S. Shionoya, Y. Tanaka and Y. Oka, J. Phys. Soc. Japan 45 (1978) 884.
[4.112] R. Lévy, B. Hönerlage and J.B. Grun, Phys. Rev. B 19 (1979) 2326.
[4.113] R. Lévy, B. Hönerlage and J.B. Grun, Solid State Comm. 29 (1979) 103.
[4.114] Vu Duy Phach and R. Lévy, Sol. State Comm. 29 (1979) 247.
[4.115] A. Bivas, Vu Duy Phach, B. Hönerlage, U. Roessler and J.B. Grun, Phys. Rev. B 20 (1979) 3442.
[4.116] B. Hönerlage, A. Bivas, Vu Duy Phach and J.B. Grun, J. Luminescence 18/19 (1979) 683.
[4.117] L.L. Chase, N. Peyghambarian, G. Grynberg and A. Mysyrowicz, Phys. Rev. Lett. 42 (1979) 1231.
[4.118] D.S. Chemla, A. Maruani and E. Batifol, Phys. Rev. Lett. 42 (1979) 1075.
[4.119] B. Hönerlage, U. Roessler, Vu Duy Phach, A. Bivas and J.B. Grun, Phys. Rev. B 22 (1980) 797.
[4.120] T. Kushida, Sol. State Comm. 32 (1979) 33 and 209.
[4.121] E. Hanamura and T. Takagahara, Sol. State Comm. 32 (1979) 19 and J. Phys. Soc. Japan 47 (1979) 410.
[4.122] J. Pollmann and H. Büttner, Sol. State Comm. 12 (1973) 1105.
[4.123] E. Hanamura, Sol. State Comm. 12 (1973) 951.
[4.124] I.A. Karp and S.A. Moskalenko, Sov. Phys. Semicond. 8 (1974) 183.
[4.125] F. Bassani, J.J. Forney and A. Quattropani, Phys. Stat. Sol. b 65 (1974) 591.

[4.126] E. Hanamura, J. Phys. Soc. Japan 29 (1970) 50; 37 (1974) 1545; 39 (1975) 1506 and 1516 and O. Akimoto, ibid 35 (1973) 973.
[4.127] C. Comte, Optics Comm. 14 (1975) 79.
[4.128] A.I. Bobrysheva and V.I. Vybornov, Phys. Stat. Sol. b 69 (1975) 267.
[4.129] F. Henneberger, Phys. Stat. Sol. b 70 (1975) K 169.
[4.130] T. Kushida and T. Moriya, Phys. Stat. Sol. b 72 (1975) 385.
[4.131] A.I. Bobrysheva, I.A. Karp and S.A. Moskalenko, Sov. Phys. Semicond. 9 (1975) 407.
[4.132] P.I. Khadzhi and K.G. Petrashku, Sov. Phys. Semicond. 9 (1975) 1510.
[4.133] E. Doni, R. Girlanda and G.P. Parravicini, Sol. State Comm. 17 (1975) 189.
[4.134] S.A. Moskalenko, Proc. 12th Europ. Congr. Molec. Spectrosc., Strasbourg (1975) p. 45.
[4.135] E. Hanamura, J. Luminescence 12/13 (1976) 119.
[4.136] R. Girlanda, E. Doni and G.P. Paravicini, Sol. State Comm. 19 (1976) 583.
[4.137] M.I. Sheboul and W. Ekardt, Phys. Stat. Sol. b 73 (1976) 165.
[4.138] W. Ekardt and M.I. Sheboul, Phys. Stat. Sol. b 73 (1976) 475.
[4.139] W. Ekardt and M.I. Sheboul, Phys. Stat. Sol. b 74 (1976) 523.
[4.140] P.I. Khadzhi, K.G. Petrashku and S.A. Moskalenko, Phys. Stat. Sol. b 76 (1976) 497.
[4.141] M. Inoue and E. Hanamura, J. Phys. Soc. Japan 41 (1976) 771.
[4.142] P.I. Khadzhi, K.G. Petrashku and S.A. Moskalenko, Sov. Phys. Sol. Stat. 17 (1976) 1550 and 2059.
[4.143] K.G. Petrashku and P.I. Khadzhi, Sov. Phys. Sol. Stat. 17 (1976) 2383.
[4.144] K.G. Petrashku and P.I. Khadzhi, Sov. Phys. Sol. Stat. 18 (1976) 1842.
[4.145] P.I. Khadzhi, Sov. Phys. Semicond. 10 (1976) 92.
[4.146] D.B. Tran Thoai, Z. Physik B 26 (1977) 115.
[4.147] W. Ekardt and M.I. Sheboul, Phys. Stat. Sol. b 80 (1977) 51.
[4.148] F. Bechstedt and F. Henneberger, Phys. Stat. Sol. b 81 (1977) 211.
[4.149] O. Goede, Phys. Stat. Sol. b 81 (1977) 235.
[4.150] F. Henneberger, K. Henneberger and J. Voigt, Phys. Stat. Sol. b 83 (1977) 439.
[4.151] K. Arya and A.R. Hassan, Sol. State Comm. 21 (1977) 301.
[4.152] W. Ekardt and M.I. Sheboul, Phys. Stat. Sol. b 86 (1978) 535.
[4.153] A.R. Hassan, Phys. Stat. Sol. b 87 (1978) 31.
[4.154] A.I. Bobrysheva, A.V. Lelyakov and V.I. Vybornov, Sov. Phys. Sol. Stat. 20 (1978) 938.
[4.155] V.I. Vybornov, Sov. Phys. Sol. Stat. 20 (1978) 423.
[4.156] W. Ekardt and H.J. Broksch, Phys. Stat. Sol. b 93 (1979) 203.
[4.157] E. Hanamura and T. Takagahara, J. Phys. Soc. Japan 47 (1979) 410.
[4.158] J. Rössler and K. Henneberger, Phys. Stat. Sol. b 93 (1979) 213.
[4.159] V. May, K. Henneberger and F. Henneberger, Phys. Stat. Sol. b 94 (1979) 611.
[4.160] W. Ekardt and M.I. Sheboul, J. Luminescence 20 (1979) 179.
[4.161] F. Henneberger, J. Voigt and E. Gutsche, J. Luminescence 20 (1979) 221.
[4.162] I. Balslev, Phys. Rev. B 20 (1979) 648.
[4.163] H. Kuroda, S. Shionoya, H. Saito and E. Hanamura, Sol. State Comm. 12 (1973) 533.
[4.164] H. Kuroda and S. Shionoya, Sol. State Comm. 13 (1973) 1195 and J. Phys. Soc. Japan 36 (1974) 476.
[4.165] Y. Segawa and S. Namba, Sol. State Comm. 14 (1974) 779.
[4.166] Y. Segawa and S. Namba, Sol. State Comm. 17 (1975) 489.
[4.167] M.A. Jacobson, G.V. Michailov, B.S. Razbirin, G.O. Müller and H.H. Weber, Sol. State Comm. 16 (1975) 1255.
[4.168] J. Voigt, F. Mir and G. Kehrberg, Phys. Stat. Sol. b 70 (1975) 625.
[4.169] O. Goede, M. Blaschke and E. Hasse, Phys. Stat. Sol. b 70 (1975) K 41.
[4.170] R. Baumert, E. Beckmann and I. Broser, Proc. 13th Intern. Conf. Phys. Semicond., Rome (1976) p. 833.
[4.171] H. Saito, A. Kuroiwa, S. Kuribayashi, Y. Aogaki and S. Shionoya, J. Luminescence 12/13 (1976) 575.
[4.172] S. Miyamoto and S. Shionoya, ibid, p. 563.
[4.173] Y. Segawa and S. Namba, ibid, p. 569.
[4.174] B.S. Razbirin, I.N. Ural'tsev and G.V. Michailov, JETP-Lett. 25 (1977) 174 and Sol. State Comm. 25 (1978) 799.
[4.175] J.M. Hvam, Sol. State Comm. 27 (1978) 1347.
[4.176] A. Kuroiwa, H. Saito and S. Shionoya, J. Phys. Soc. Japan 45 (1978) 1664.
[4.177] V.G. Lyssenko, V.I. Revenko and V.B. Timofeev, JETP-Lett. 24 (1976) 137.
[4.178] V.G. Lyssenko and V.B. Timofeev, Sov. Phys. Sol. Stat. 18 (1976) 588.
[4.179] A.A. Gogolin and E.I. Rashba, JETP-Lett. 17 (1973) 69 and E.I. Rashba, Springer Tracts in Mod. Phys. Vol. 73 (1975) p. 150 and Sov. Phys. Sol. Stat. 15 (1974) 182.
[4.180] A. Bivas, Thesis, Strasbourg (1978).
[4.181] J.B. Grun, R. Lévy, E. Ostertag, Vu Duy Phach and H. Port, Proc. Oji Seminar on the Physics of Highly Excited States in Solids, Lecture Notes in Physics 57 (Springer, Berlin, 1976) p. 49.

[4.182] M. Ueta and N. Nagasawa, ibid, p. 1.
[4.183] T. Itoh, Y. Nozue and M. Ueta, J. Phys. Soc. Japan 40 (1976) 1791.
[4.184] J. Puls and J. Voigt, Phys. Stat. Sol. b 94 (1979) 199.
[4.185] V.G. Lyssenko and H. Schrey, private communication.
[4.186] H. Schrey and C. Klingshirn, Sol. State Comm. 33 (1980) 485.
[4.187] B. Hönerlage and J.B. Grun, private communication.
[4.188] A. Kuroiwa, H. Saito and S. Shionoya, Sol. State Comm. 18 (1976) 1107.
[4.189] J. Voigt and I. Rückmann, Phys. Stat. Sol. b 61 (1974) K 85.
[4.190] I. Rückmann, J. Puls and J. Voigt, Phys. Stat. Sol. b 87 (1978) K 111.
[4.191] T. Itoh, Y. Nozue and M. Ueta, J. Phys. Soc. Japan 40 (1976) 1791.
[4.192] Y. Nozue, T. Itoh and M. Ueta, J. Phys. Soc. Japan 44 (1978) 1305.
[4.193] H. Schrey and C. Klingshirn, Sol. State Comm. 28 (1978) 9.
[4.194] H. Schrey, V.G. Lyssenko and C. Klingshirn, Sol. State Comm. 32 (1979) 897.
[4.195] J.M. Hvam, Phys. Stat. Sol. b 93 (1979) 581.
[4.196] J. Voigt, F. Spiegelberg and M. Senoner, Phys. Stat. Sol. b 91 (1979) 189.
[4.197] M. Itoh, Y. Nozue, T. Itoh, M. Ueta, S. Satoh and K. Igaki, J. Luminescence 18/19 (1979) 568.
[4.198] G. Behnke and H. Büttner, Phys. Stat. Sol. b 90 (1978) 53.
[4.199] J.J. Hopfield, Phys. Rev. 112 (1958) 1955.
[4.200] S.J. Pekar, Sov. Phys. JETP 6 (1958) 785.
[4.201] D. Fröhlich, E. Mohler and P. Wiesner, Phys. Rev. Lett. 10 (1971) 554.
[4.202] H. Schrey, V.G. Lyssenko, C. Klingshirn and B. Hönerlage, Phys. Rev. B 20 (1979) 5267.
[4.203] J.J. Hopfield and D.G. Thomas, Phys. Rev. 122 (1961) 35 and Phys. Rev. Lett. 15 (1965) 22.
[4.204] W. Stößel and H.J. Wagner, Phys. Stat. Sol. b 89 (1978) 403.
[4.205] I. Broser, M. Rosenzweig, R. Broser, M. Richard and E. Birkicht, Phys. Stat. Sol. b 90 (1978) 77.
[4.206] J. Voigt, M. Senoner and I. Rückmann, Phys. Stat. Sol. b 75 (1976) 213 and
J. Voigt, F. Spiegelberg and M. Senoner, Phys. Stat. Sol. b 91 (1979) 189.
[4.207] G. Winterling and E. Koteles, Sol. State Comm. 23 (1977) 95 and Proc. Intern. Conf. Lattice Dynamics, Paris (1977) p. 170.
[4.208] R.H. Bruce and H.Z. Cummins, Phys. Rev. B 16 (1977) 4462.
[4.209] H.W. Verleur and A.S. Barker Jr., Phys. Rev. 155 (1967) 750.
[4.210] H. Schrey, V.G. Lyssenko and C. Klingshirn, Sol. State Comm. 31 (1979) 299.
[4.211] R. Ulbrich and C. Weisbuch, Advances in Solid State Phys. Vol. XVIII (1978) p. 217.
[4.212] T. Kobayashi, Y. Segawa and S. Namba, Sol. State Comm. 31 (1979) 253.
[4.213] C. Klingshirn, V.G. Lyssenko and H. Schrey, JETP Lett. 30 (1979) 568.
[4.214] S.G. Elkomoss and G. Munschy, J. Phys. Chem. Sol. 38 (1977) 557.
[4.215] J. Puls, I. Rückmann and J. Voigt, Phys. Stat. Sol. b 96 (1979) 642.
[4.216] T. Anzai, T. Goto and M. Ueta, J. Phys. Soc. Japan 38 (1975) 774.
[4.217] H. Haug, R. März and S. Schmitt-Rink, Phys. Lett. 77A (1980) 287.
[4.218] Y. Toyozawa, J. Phys. Soc. Japan 41 (1976) 400.
[5.1] R.F. Leheny and J. Shah, Phys. Rev. Lett. 37 (1976) 871.
[5.2] O. Hildebrand, F. Faltermeier and M.H. Pilkuhn, Sol. State Comm. 19 (1976) 841.
[5.3] O. Hildebrand and E. Göbel, Proc. 13th Intern. Conf. Phys. Semiconductors, ed. F.G. Fumi (Rome, 1976) p. 942.
[5.4] G.O. Müller and R. Zimmermann, Proc. 14th Intern. Conf. Phys. Semiconductors, ed. B.L.H. Wilson (Edinburgh. 1978) p. 165.
[5.5] G.O. Müller, H.H. Weber and I. Höricke, Phys. Stat. Sol. b 91 (1979) 531.
[5.6] K. Bohnert, G. Schmieder, S. El-Dessouki and C. Klingshirn, Sol. State Comm. 27 (1978) 295.
[5.7] O. Hildebrand, E. Göbel, K.M. Romanek, H. Weber and G. Mahler, Phys. Rev. B 17 (1978) 4775.
[5.8] G. Lasher and F. Stern, Phys. Rev. 133 (1964) A 553.
[5.9] W.F. Brinkman and P.A. Lee, Phys. Rev. Lett. 31 (1973) 257.
[5.10] M. Rösler and R. Zimmermann, Phys. Stat. Sol. b 67 (1975) 525.
[5.11] R. Zimmermann, Phys. Stat. Sol. b 86 (1978) K 63 and Phys. Stat. Sol. 15 (1966) 623.
[5.12] P.T. Landsberg, Proc. Phys. Soc. A 62 (1949) 806.
[5.13] R.N. Silver and C.H. Aldrich, Phys. Rev. Lett. 41 (1978) 1248 and Phys. Rev. B 21 (1980) 600.
[5.14] H. Haug and D.B. Tran Thoai, Phys. Stat. Sol. b 98 (1980) 581.
[5.15] H. Haken, Synergetics (Springer Verlag, Berlin, 1977).
[5.16] S.W. Koch and H. Haug, Phys. Stat. Sol. b 95 (1979) 155.
[5.17] S.W. Koch and H. Haug, Phys. Lett. 74A (1979) 250.
[5.18] H. Haug and D.B. Tran Thoai, Phys. Stat. Sol. b 85 (1978) 561.
[5.19] R. Zimmermann, K. Kilimann, W.D. Kraeft, D. Kremp and R. Röpke, Phys. Stat. Sol. b 90 (1978) 175.
[5.20] G. Beni and T.M. Rice, Phys. Rev. B 18 (1978) 768 and Phys. Rev. Lett. 37 (1976) 874.
[5.21] M. Rösler and R. Zimmermann, Phys. Stat. Sol. b 83 (1977) 85.
[5.22] G. Mahler, Phys. Rev. B 11 (1975) 4050.

[5.23] R.N. Silver, Phys. Rev. B 8 (1973) 2403.
[5.24] H. Haug, Z. Physik B 24 (1976) 351.
[5.25] P. Kadanoff and G. Baym, Quantum Statistical Mechanics (W.A. Benjamin, New York, 1962).
[5.26] H. Stolz, Einführung in die Vielelektronentheorie der Kristalle (Akademie Verlag, Berlin, 1976).
[5.27] M. Combescot and P. Nozière, J. Phys. C 5 (1972) 2369.
[5.28] W.F. Brinkman and T.M. Rice, Phys. Rev. B 7 (1970) 1508.
[5.29] R. Zimmermann and M. Rösler, Phys. Stat. Sol. b 75 (1976) 633.
[5.30] K. Keldysh and A.A. Silin, Sov. Phys. JETP 42 (1976) 535.
[5.31] M. Rösler and R. Zimmermann, Phys. Stat. Sol. b 67 (1975) 525.
[5.32] Unpublished calculations by S. Schmitt-Rink.
[5.33] T.L. Reinecke and S.C. Ying, Phys. Rev. Lett. 43 (1979) 1054.
[5.34] T. Skettrup, Sol. State Comm. 23 (1977) 741.
[5.35] V.S. Bagaev, N.V. Zamkovets, L.V. Keldysh, N.N. Si'beldin and V.A. Tsvetkov, Sov. Phys.-JETP 43 (1976) 783.
[5.36] J.L. Staehli, Phys. Stat. Sol. b 75 (1976) 451.
[5.37] R.N. Silver, Phys. Rev. B 11 (1975) 1569; B 12 (1975) 5689; B 16 (1977) 797.
[5.38] R.M. Westervelt, Phys. Stat. Sol. b 74 (1976) 727.
[5.39] M. Combescot, Phys. Rev. B 21 (1980) 771.
[5.40] R.M. Westervelt, T.K. Lo, J.L. Staehli and C.D. Jeffries, Phys. Rev. Lett. 32 (1974) 1051.
[5.41] K. Arya and W. Hanke, Sol. State Comm. 33 (1980) 739.
[5.42] T.M. Rice, Phys. Rev. B 9 (1974) 1540.
[5.43] M. Combescot and R. Combescot, Phys. Lett. 56A (1976) 228.
[5.44] S.W. Koch, Sol. State Comm. 35 (1980) 419.
[5.45] F.S. Rogers, H.C. Graboske and D.J. Harwood, Phys. Rev. A 1 (1970) 1577.
[5.46] W. Ebeling, W.D. Kraeft and D. Kremp in: Ergebnisse der Plasmaphysik und der Gaselektronik, Vol. 5 (Akademie Verlag, Berlin, 1976) p. 1.
[5.47] J.G. Gay, Phys. Rev. B 4 (1971) 2567.
[5.48] G. Mahler and J.L. Birman, Phys. Rev. B 16 (1977) 1552.
[5.49] D.B. Tran Thoai and H. Haug, J. Luminescence 18/19 (1979) 309.
[5.50] H. Stolz and R. Zimmermann, Phys. Stat. Sol. b 94 (1979) 135.
[5.51] K.L. Shaklee, Springer Tracts in Mod. Physics 73 (1975) p. 225.
[5.52] I. Kh. Akopyan and B.S. Razbirin, Sov. Phys. Sol. Stat. 16 (1976) 113.
[5.53] R.F. Leheny, J. Shah and G. Chiang, Sol. State Comm. 25 (1978) 621.
[5.54] J. Heidmann and T. Skettrup, Sol. State Comm. 23 (1977) 27.
[5.55] S.I. Pekar, Sov. Phys. JETP 33 (1958) 785 and 34 (1958) 813 and 36 (1959) 314.
[5.56] J.J. Hopfield and D.G. Thomas, Phys. Rev. 132 (1963) 563.
[5.57] J. Lagois, Phys. Rev. B 16 (1977) 1699.
[5.58] Z.A. Hoffman, K. Jarašiūnas, H.J. Gerritsen and A.V. Nurmikko, Appl. Phys. Lett. B 33 (1978) 563.
[5.59] J. Shah, R.F. Leheny and W. Wiegmann, Phys. Rev. B 16 (1977) 1577.
[5.60] V.G. Lyssenko and V.I. Revenko, Sov. Phys. Sol. Stat. 20 (1978) 1238.
[5.61] V.G. Lyssenko, V.I. Revenko, F.G. Tartas and V.G. Timofeev, Sov. Phys. JETP 41 (1975) 163.
[5.62] T. Skettrup, Sol. State Comm. 23 (1977) 741.
[5.63] P. Motisuke, C.A. Arguello and R. Luzzi, Sol. State Comm. 23 (1977) 617.
[5.64] R. Baltrameyunas and E. Kuokshtis, JETP-Lett. 28 (1978) 66.
[5.65] R. Baltrameyunas and E. Kuokshtis, JETP-Lett. 28 (1978) 543.
[5.66] M.G. Matsko and O.V. Franiv, Sov. Phys. Sol. Stat. 21 (1979) 553.
[5.67] M.S. Brodin, N.V. Volovik and M.I. Strashinkova, JETP-Lett. 23 (1976) 227;
N.V. Volovik and M.I. Strashinkova, Sov. Phys. Sol. Stat. 20 (1978) 94.
[5.68] G.O. Müller, M. Rösler, H.H. Weber, R. Zimmermann, M.A. Jacobson, G.V. Michailov, B.S. Razbirin and I.N. Ural'tsev, J. Luminescence 12/13 (1976) 557.
[5.69] H. Saito, M. Hayashi and S. Shionoya, Sol. State Comm. 24 (1977) 837.
[5.70] H. Saito and S. Shionoya, Sol. State Comm. 27 (1978) 1331.
[5.71] D.H. Auston, Proc. 14th Intern. Conf. Phys. Semiconductors, Edinburgh (1978) p. 73 and the literature cited therein.
[5.72] C.V. Shank, R.L. Fork, R.F. Leheny and J. Shah, Proc. 14th Intern. Conf. Phys. Semiconductors, Edinburgh (1978) p. 493;
C.V. Shank, D.H. Auston, E.P. Ippen and O. Teschke, Sol. State Comm. 26 (1978) 567;
C.V. Shank, R.L. Fork, R.F. Leheny and J. Shah, Phys. Rev. Lett. 42 (1979) 121.
[5.73] D.v.d. Linde and R. Lambrich, Phys. Rev. Lett. 42 (1979) 1090.
[5.74] R. Lévy, A. Bivas, J.B. Grun and S. Nikitine, Springer Tracts in Mod. Phys. 73 (1975) p. 171.
[5.75] R.F. Leheny and J. Shah, Phys. Rev. Lett. 38 (1977) 511.
[5.76] S. Schmitt-Rink, D.B. Tran Thoai and H. Haug, Z. Physik B 39 (1980) 25.
[5.77] S. Schmitt-Rink, D.B. Tran Thoai and H. Haug, Sol. State Comm. (in print).

Note added in proof

The manuscript of this paper has been finished in the beginning of 1980. Since then interesting new results have been published in the field of HES. Some of them will be shortly mentioned here:

In CuBr, it was possible to investigate the dispersion and splitting of the biexciton levels in k-space by angle dependent two-photon absorption (TPA) [6.1]. Two-photon Raman scattering (TRPS) has been performed for the first time in a layer compound (PbJ_2) and the biexciton has been detected in this material by luminescence assisted two-photon spectroscopy (LATS) [6.2]. This technique has also been adopted in [6.3] to deduce – together with TPA – the dispersion curves of excitons and biexcitons in a rather large region of the Brillouin zone.

The anomaly in the dispersion curve due to the two-polariton transition from the crystal ground state to the biexciton has observed in CdS [6.4] together with some further renormalization effects which allow now to fit the TPRS data of CdS with the conventional background dielectric constant of 8 [6.5]. A quantitative theory of the intensity dependent renormalization effect has been developed [6.6], and it has been pointed out that this effect can be used to obtain optical bistability [6.7]. Furthermore, the Γ_1 biexciton level of CdS has been confirmed by low intensity nonlinear coherent mixing [6.8]. In wurtzite and zincblende type II–VI compounds TPRS measurements have been performed for the first time in strong magnetic fields [6.4, 6.5, 6.9].

Concerning the EHP in direct gap materials, both experimental and theoretical results indicate, that the plasma does not completely reach its thermodynamic equilibrium state, due to the short lifetime of the e–h pairs: New experimental results for GaAs are given in [6.10] where also Raman scattering involving plasmons in the EHP has been reported. Time resolved measurements are published for GaAs in [6.11]. A detailed theoretical investigation of the nucleation indicates, that only very tiny e–h pair clusters are formed in a EHP in direct gap materials [6.12, 6.13], the number of the pairs per cluster being generally for below 100. Time resolved measurements of the EHP in CdS revealed, that the plasma reaches different states for different excitation intensities after a relaxation time of about 80 ps [6.14]. A detailed investigation of the EHP gain spectra in CdS shows furthermore, that the density in the EHP increases both with I_{exc} and T_p in contrast to the publications of an equilibrium phase transition [6.13, 6.15].

First investigations of the EHP in highly excited and highly doped CdS have been reported in [6.16].

[6.1] R. Lévy, B. Hönerlage and J.B. Grun, Phys. Rev. Lett. 44 (1980) 1355.
[6.2] R. Lévy, A. Bivas, B. Hönerlage and Q.H. Yu, to be published in Physica B (1980) (Proc. of the PLCM-Conf. Sendai 1980).
[6.3] T. Mita, K. Sôtome and M. Ueta, J. Phys. Soc. Japan 48 (1980) 496.
[6.4] G. Kurtze, W. Maier, G. Blattner and C. Klingshirn, Z. Physik B 39 (1980) 95.
[6.5] G. Kurtze, W. Maier, K. Kempf, G. Schmieder, H. Schrey, C. Klingshirn, B. Hönerlage and U. Rössler, Proc. 15th Intern. Conf. Physics Semicond. Kyoto (1980).
[6.6] R. März, S. Schmitt-Rink and H. Haug, Z. Physik B 40 (in print).
[6.7] S.W. Koch and H. Haug, preprint.
[6.8] A. Marnani, D.S. Chemla and E. Batifol, Sol. State Comm. 33 (1980) 805.
[6.9] W. Maier, G. Blattner, G. Kurtze and C. Klingshirn, Z. Physik B 40 (1980).
[6.10] K.M. Romanek, E.O. Göbel, H. Conzelmann and H. Nather, Proc. 15th Intern. Conf. Phys. Semicond. Kyoto (1980).
[6.11] S. Tanaka, H. Kobayashi, H. Saito and S. Shionoya, Sol. State Comm. 33 (1980) 167.
[6.12] H. Haug and F.F. Abraham, to be published in Phys. Rev. B.
[6.13] H. Haug, D.B. Tran Thoai, S. Schmitt-Rink, K. Bohnert, C. Klingshirn and G. Blattner, Proc. 15th Intern. Conf. Phys. Semicond. Kyoto (1980).
[6.14] H. Yoshida, H. Saito, S. Shionoya and V.B. Timofeev, Sol. State Comm. 33 (1980) 161.
[6.15] K. Bohnert, M. Anselment, G. Kobbe, C. Klingshirn, F.F. Abraham, H. Haug, S.W. Koch and S. Schmitt-Rink, to be published in Z. Physik B.
[6.16] G.O. Müller, M. Rösler and R. Zimmermann, Proc. 15th Int. Conf. Phys. Semicond. Kyoto (1980).